Università di Pisa

Dipartimento di Fisica
Corso di Laurea Magistrale in Fisica

Development of an algorithm to increase the K_S tracking efficiency at Belle II

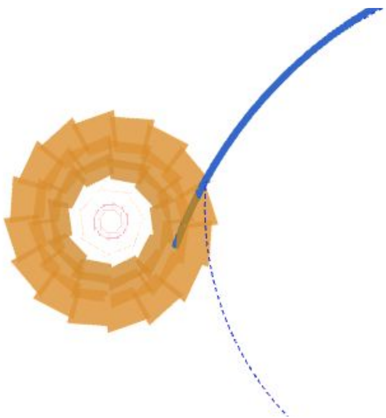

Relatrice:
Prof. Giulia Casarosa

Candidata:
Matilde Carminati

Anno accademico 2023/2024

Contents

Introduction

Today High Energy Physics experiments focus on testing the Standard Model (SM), a very successful theory that describes the interactions among elementary particles, for most of the known processes. For instance, it does not comprise gravity or dark matter and it leaves many other open questions; moreover anomalies were found between experimental measurements and theoretical predictions. Among all these puzzles, there is the size of the observed asymmetry between matter and antimatter in the Universe. Measurements of the CP asymmetry in meson decays are one of the main ways in trying to understand this mystery. At the Belle II experiment such measurements are brought forward in the charm and beauty flavor sectors. Being an experiment on the intensity frontier, Belle II aims to acquired high statistics to analyze the decays of the D and B mesons, where the K_S is often present in the final state. Due to its displaced decay vertex, the tracking reconstruction of the K_S is not as good as primary particles. Then the measurements at Belle II with the K_S in the final state are dominated by the statistical uncertainty.

This thesis' project is to improve the tracking efficiency of the K_S by implementing a new algorithm to be inserted in the current reconstruction software of the experiment. Since I have found out that, in the $K_S \to \pi^+\pi^-$ decay, the primary source of the K_S tracking inefficiency is the failure to reconstruct one of its two charged daughters, the developed algorithm aims to recover the track of the K_S missing daughter, utilising information only from the Silicon Vertex Detector (SVD) and the fitted track of the reconstructed daughter. The position of the K_S decay vertex is assumed to lay on the helix arc of the reconstructed daughter between its innermost SVD hit and the position of the backward extrapolation on the previous SVD layer. This estimate is used, together with the assumption that the K_S is coming from the interaction region, to solve a second-degree equation from the quadri-momentum conservation, and to compute two estimates of the K_S momentum, and thus of the missing pion. Each estimate is used as seed, together with the estimated K_S decay vertex position, to build a temporary helix of the missing pion. Such helix is used to search for SVD hits near its intersections with the SVD layers, in order to reconstruct the track. The algorithm is implemented from scratch in the official Belle II analysis software framework to explore its potential.

The thesis is structured as follows. Chapter 1 presents an overview of the SM: its structure is briefly described, the Cabibbo-Kobayashi-Maskawa matrix is presented for its relation with CPV. CPV effects observed in the weak decays of flavored mesons are discussed with a focus on the mixing process of the neutral meson systems. At the end of the chapter some CPV measurements, performed at the Belle II experiment, are reported.

In Chapter 2 the Belle II experiment and the accelerator SuperKEKB are presented. The section of the accelerator focuses on the strategy allowing the high luminosity and the relative generated beam backgrounds. The status of the data taking is mentioned. Then the sub-detectors of the experiment are briefly described, only the Silicon Vertex Detector is discussed on a deeper level. At the end, the Belle II analysis software framework (basf2) is introduced and the SVD signals' reconstruction is described.

In Chapter 3, after a brief description on the trajectory of the charged particles at collider experiments, the tracking algorithms implemented in basf2 are reported. The discussion focuses on the track finding of the two main tracking detector, the VerteX Detector (VXD) and the Central Drift Chamber (CDC). The performance of the tracking software is shown and a study on the reconstruction efficiency and inefficiency of the K_S is presented.

Chapter 4 describes the new algorithm to recover the K_S lost by the current tracking algorithm. First an overview of the K_S decay is given and then the steps of the new algorithm are discussed in details. The results on the efficiency of the algorithm is computed in a toy data sample with and without beam background. In Chapter 5 the results of the algorithm applied to a $B\overline{B}$ data sample are reported and some improvements have been made. The impact on CPV measurements with one or two K_S in the final state is computed.

Chapter 1

CP Violation in the Standard Model

In this chapter an overview on CP violation (CPV) in meson systems is given. This is needed to understand the nature of the K_S particle as well as the physics importance of measurements in which the gain in reconstruction efficiency of the K_S is relevant.

At first the Standard Model (SM) structure is briefly explained with a description of its main components, and the Cabibbo-Kobayashi-Maskawa (CKM) matrix is presented to explain how CPV fits in the SM framework. Then, the CPV effects in meson systems are listed with a focus on the description of the mixing process in neutral mesons. In the end some examples of CPV measurements conducted at Belle II in the B and the D sectors, with a K_S in the final state, are reported.

1.1 Introduction to the Standard Model

As of today, the SM [1, 2] is the most complete theory in particle physics, whose goal is the understanding of the fundamental constituents and forces of the Universe. The SM theory manages to describe three of the known fundamental forces, the electromagnetic, the strong and the weak forces; while it does not include the description of the gravitational one. In the SM framework there are seventeen fundamental particles, outlined in Fig. 1.1: twelve fermions (spin-half particles), four vector bosons (1-spin particles) and one scalar boson (0-spin particle).

The fundamental elements of matter are the twelve fermions, divided in six quarks (blue colored in Fig. 1.1) and six leptons (green colored). Quarks and leptons are organized in three generations. Each quark generation is composed of an *up*-type quark (u, c and t), with charge $q = +\frac{2}{3}e$, and a *down*-type quark (d, s, and b), with charge $q = -\frac{1}{3}e$; while each lepton generation is composed by a charged lepton (ℓ, charge $q = -e$) and the corresponding neutrino (ν_ℓ, zero charge):

$$\begin{pmatrix} \ell^- \\ \nu_\ell \end{pmatrix} \quad \begin{pmatrix} u \\ d \end{pmatrix}. \tag{1.1}$$

Both the charged leptons and the quarks possess the empirical feature to increase their masses with the generation, for instance an electron is lighter than a muon that is lighter than a tau. Each lepton generation is characterized by the relative lepton number, that is individually conserved in strong and electromagnetic processes, while the weak interaction conserves only the total lepton number (resulting as the sum of the electron, muon and tau lepton numbers). The heavier quarks also have a quantum number F, called *flavour*, conserved in strong and electromagnetic interaction; each quark has a

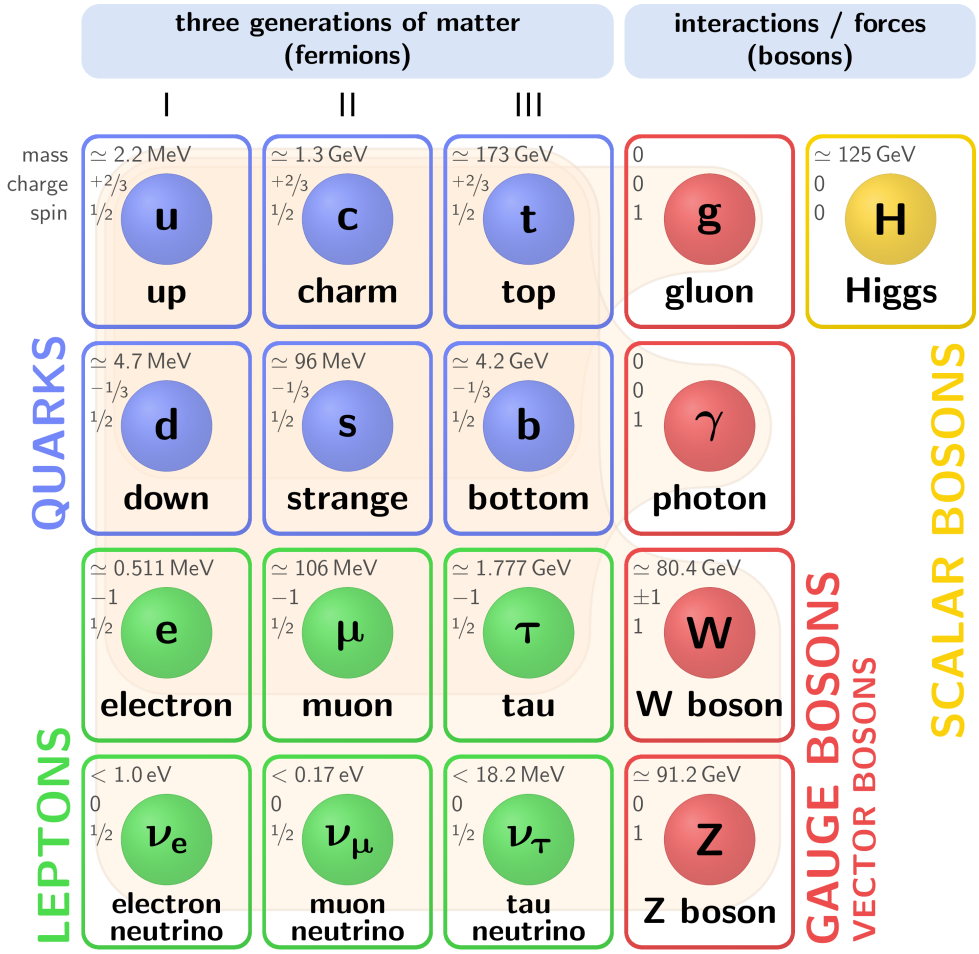

Figure 1.1: A representation of the fundamental SM particles.

different one: charm for *charm* quarks (c), strangeness for *strange* quarks (s), beauty or bottomness for *bottom* quarks (b) and topness for *top* quarks (t).

Each fermion f has a twin antiparticle $\overline{f}$, with the same mass and decay width, but opposite helicity and quantum numbers, such as the electric charge, flavour and lepton number. The helicity $\widehat{h}$ is a quantity defined as the projection of the spin $\overrightarrow{S}$ along the direction of the momentum $\overrightarrow{p}$ of the particle:

$$\widehat{h} \equiv \frac{\overrightarrow{S} \cdot \overrightarrow{p}}{p} \tag{1.2}$$

Antiparticles are always right handed (projection of the spin with the same direction of the motion), while particles are always left handed (opposite direction). Antiparticles are the fundamental components of the antimatter and, mathematically, they come from the negative solutions for the energy of the Dirac equation.

Unlike leptons, quarks can not be observed as free particles, but they are confined by the strong force in bound states, called *hadrons*. The hadronic states are classified in:

- *mesons*, formed by a quark and an antiquark ($\mathrm{q\overline{q}}$)
- *baryons*, composed of three quarks (qqq)
- *antibaryons*, consisting of three antiquarks ($\mathrm{\overline{q}\,\overline{q}\,\overline{q}}$).

For example the K^0 is a meson composed of a $\overline{s}$ anti-quark and a d quark, its antiparticle is the $\overline{K}^0 = s\overline{d}$.

In the SM, the interactions are described by the exchange of some mediating particles, the vector or gauge bosons (red colored in Fig. 1.1):

- the photon (γ) mediates the electromagnetic force that is described by the QED, it can interact with all the charged particles, therefore among the fermions only the neutrinos do not feel the electromagnetic force
- the gluon (g) mediates the strong force, described by QCD, and it interacts only with quarks
- the $W^{\pm}$ and the Z^0 mediate the weak interaction, described by the electroweak theory, and they interact with all the fermions.

The SM picture is completed by the Higgs boson (yellow colored in Fig. 1.1), the only scalar boson of the SM. It was the last SM particle to be observed in 2012 at the LHC experiments [3, 4]. It is responsible for giving mass to the SM particles via a spontaneous symmetry breaking.

1.1.1 Physics beyond the SM

In the past years many tests were performed to verify the predictions of the SM: while there are few measurements in tension with the theoretical predictions, most of them result consistent till now. Despite its success there are many questions that still do not find an answer in the SM.

For example, what is the source of the observed asymmetry between matter and antimatter in the Universe? According to the Big Bang theory, the early Universe had a symmetric composition of matter and antimatter. On the other hand, it is possible to say with confidence that the composition of our Universe is dominated by matter, from the observations made in astronomical searches that exclude the idea of regions of space dominated by antimatter. The violation of the CP symmetry is a required ingredient to explain the generation of this asymmetry, however the one contained in the SM is not big enough.

The CP transformation combines the charge conjugation (C) and the parity (P) transformations. In the C transformation all the particle's quantum numbers change sign. While the parity transforms the vectors and the pseudo-scalar, leaving unchanged the scalar quantities and the axial-vectors: the vectors, like the momentum, reverse their direction and the pseudo-scalars, like the helicity, change their sign. Hence CP transforms matter in antimatter and vice-versa. If this transformation was an exact symmetry, then matter and antimatter would follow the same laws. Though it was observed that CP is conserved in electromagnetic and strong interaction, that's not the case in weak interaction, where C and P are also violated, separately and in the strongest possible way.

Another example of unanswered question is the nature of Dark Matter (DM), a form of matter that does not interact with the electromagnetic field. Dark matter is implied by gravitational effects which cannot be explained by general relativity unless more matter than the observed one is present. The problem arises from the fact that the observed matter is just the 5% of the Universe, while the remaining 95% is divided between dark energy and dark matter, whose exact composition remains unknown.

There are other open questions like: why are there only three generations of elementary fermions and what is the origin of the mass hierarchy? Is it possible to include Gravitational interactions in a unified theory? And many more.

Therefore, the SM can not be the ultimate theory of particle physics. To search for the answers of such questions two complementary approaches are taken at collider experiments: the energy frontier, carried forward for example at CMS and ATLAS, and the intensity frontier, explored for instance by the Belle II and LHCb experiments. At the energy frontier, experiments increase their energy in the center of mass frame to be able to create heavier and unknown particles and final states, while at the intensity frontier the experiments increase the luminosity, to collect more data and be able to perform high precise measurements.

In the Belle II experiment, the physics program [5] spans a broad range of physics domains, including flavour physics, tau physics and the dark sector. The aim of this thesis project, the improvement of K_S tracking efficiency, can have broad applications in Belle II since the K_S is often present in the final state of many interesting decays of B, D mesons and τ leptons. For what concerns this thesis, I decided to focus on the impact on CPV measurements in meson decays, however more applications could be considered. In the following section I will discuss CPV in the SM.

1.1.2 The CKM quark mixing matrix

In the SM, the CP violation appears only in the weak interactions of leptons and quarks, although for now it is observed only in the quark sector. In the latter, CPV is described by the weak phase of the Cabibbo-Kobayashi-Maskawa (CKM) matrix, $\mathrm{V_{CKM}}$.

The $\mathrm{V_{CKM}}$ is an unitarity matrix that describes the relation between the weak (marked by the " $'$ " in Eq. 1.3) and the mass eigenstates of the d-type quarks, as the natural extension of the Cabibbo mechanism to three generations of quarks:

$$\begin{pmatrix} \mathrm{d}' \\ \mathrm{s}' \\ \mathrm{b}' \end{pmatrix} = \begin{pmatrix} \mathrm{V_{ud}} & \mathrm{V_{us}} & \mathrm{V_{ub}} \\ \mathrm{V_{cd}} & \mathrm{V_{cs}} & \mathrm{V_{cb}} \\ \mathrm{V_{td}} & \mathrm{V_{ts}} & \mathrm{V_{tb}} \end{pmatrix} \begin{pmatrix} \mathrm{d} \\ \mathrm{s} \\ \mathrm{b} \end{pmatrix}. \tag{1.3}$$

It can be parameterized with three real parameters and a complex phase. The following parametrization highlights its origin from the Cabibbo mechanism:

$$\mathrm{V_{CKM}} = \begin{pmatrix} 1 & 0 & 0 \\ 0 & c_{23} & s_{23} \\ 0 & -s_{23} & c_{23} \end{pmatrix} \begin{pmatrix} c_{13} & 0 & s_{13}e^{-i\delta} \\ 0 & 1 & 0 \\ -s_{13}e^{-i\delta} & 0 & c_{13} \end{pmatrix} \begin{pmatrix} c_{12} & s_{12} & 0 \\ -s_{12} & c_{12} & 0 \\ 0 & 0 & 1 \end{pmatrix} \tag{1.4}$$

where $s_{ij} = \sin\phi_{ij}$ and $c_{ij} = \cos\phi_{ij}$; the parameters are the three rotation angles ϕ_{ij} between the weak and the mass eigenstates along with the complex phase δ, that is responsible for the CP violation effect in flavour changing process.

The magnitudes of the nine elements of the matrix have been measured both separately and together as results of a global fit of the unitarity triangle, explained later in this section. The absolute values of the matrix's elements measured with the global fit [6] are:

$$|V_{CKM}| = \begin{pmatrix} 0.97435 \pm 0.00016 & 0.22500 \pm 0.00067 & (3.69 \pm 0.11)10^{-3} \\ 0.22486 \pm 0.00067 & 0.97349 \pm 0.00016 & (41.82^{+0.85}_{-0.74})10^{-3} \\ (8.57^{+0.20}_{-0.18})10^{-3} & (41.10^{+0.83}_{-0.72})10^{-3} & 0.999118^{+0.000031}_{-0.000030} \end{pmatrix} \tag{1.5}$$

The elements on the diagonal represent flavour transitions within the same generation of quarks and they are near the unity, while the off-diagonal terms, representing flavour transitions between different quark generations, are smaller. The magnitudes of the off-diagonal terms decrease as the generations of the quarks involved in the transition are further apart, for example a transition from the third to the first generation is more suppressed than from the third to the second ones. To highlight this hierarchical structure of the matrix, it is convenient to express it using the Wolfenstein parametrization, where the CKM matrix is written as an expansion of the parameter $\lambda = \sin\phi_{12} = 0.225$ (ϕ_{12} is also known as Cabibbo angle):

$$\begin{pmatrix} 1-\lambda^2/2 & \lambda & A\lambda^3(\rho - i\eta) \\ -\lambda & 1-\lambda^2/2 & A\lambda^2 \\ A\lambda^3(1-\rho-i\eta) & -A\lambda^2 & 1 \end{pmatrix} + \mathcal{O}(\lambda^4), \tag{1.6}$$

where $A = s_{23}/s_{12}^2$, $\rho = s_{13}\cos\delta/(s_{23}s_{12})$ and $\eta = s_{13}\sin\delta/(s_{23}s_{12})$. In this representation, all the parameters are real, and the complex phase responsible of the CP violation is ensured with $\eta \neq 0$.

The unitarity of the CKM matrix imposes $\sum_i V_{ij}V_{ik}^* = \delta_{jk}$ and $\sum_j V_{ij}V_{kj}^* = \delta_{ik}$. The six combinations equal to zero ($j \neq k$ for the first and $i \neq k$ for the second relations) can be represented as triangles in the complex plane $(\overline{\rho}, \overline{\eta})$, defined as:

$$\overline{\rho} \simeq \rho(1-\lambda^2/2), \quad \overline{\eta} \simeq \eta(1-\lambda^2/2). \tag{1.7}$$

The area of these six triangles is the same and it is proportional to the CP violation component: if the triangles were degenerate (area equal to zero) there won't be any CP violation in the SM quark mixing.

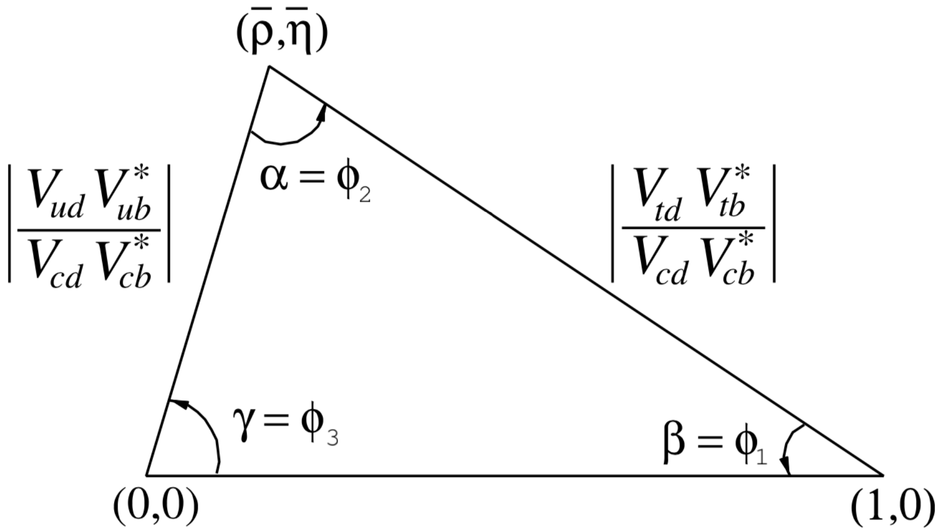

Figure 1.2: The unitarity triangle corresponding to Eq. 1.8. The double notation of the angles come from the two first-generation B-factories: Belle used ϕ_1, ϕ_2 and ϕ_3, while BaBar used α, β and γ. In this thesis the second notation is used.

The most commonly used unitarity triangle, shown in Fig. 1.2, is defined by

$$V_{ud}V_{ub}^* + V_{cd}V_{cb}^* + V_{td}V_{tb}^* = 0 \tag{1.8}$$

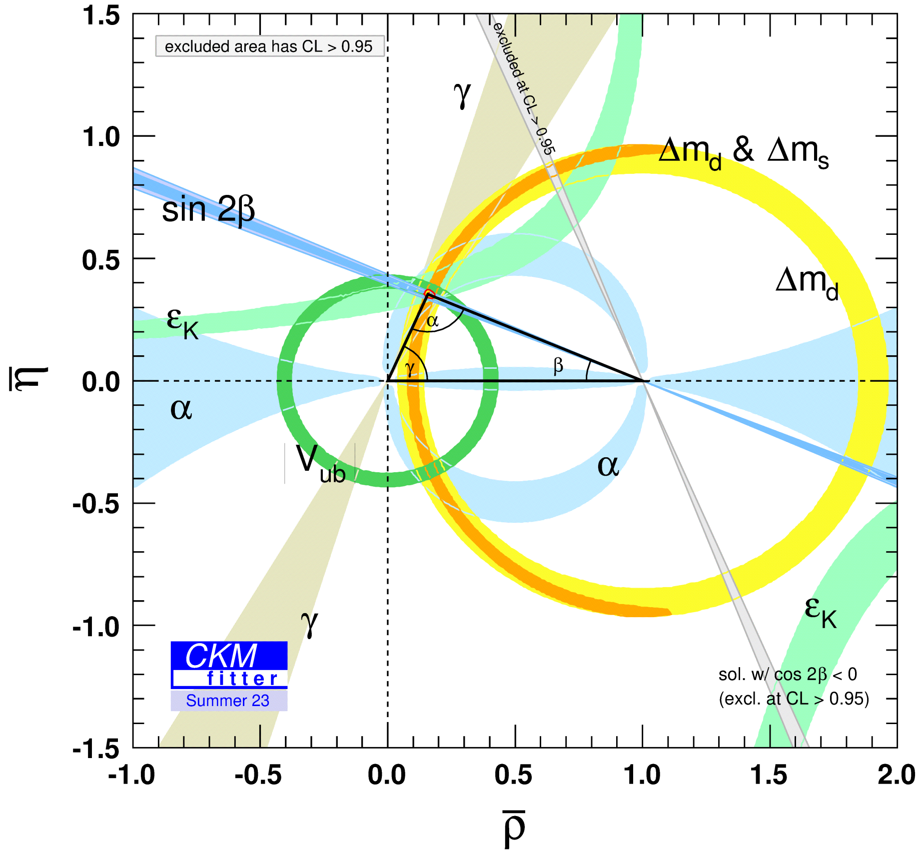

Figure 1.3: The global fit of all the measurements related to the unitarity triangle of Fig. 1.2. The plot is taken from [7].

divided by $V_{cd}V_{cb}^*$. Its vertices are in $(0,0)$, $(1,0)$ and $(\overline{\rho},\overline{\eta})$. To constrain $\overline{\eta}$ and $\overline{\rho}$, different measurements of the triangle's angles and sides are made; all the results are considered in the global fit reported in Fig. 1.3.

CPV is well established inside the SM, but its size is not enough to explain the observed asymmetry between matter and antimatter in the Universe. To understand its origin it is needed to test the SM with more precise measurements: new sources of CPV might reveal themselves as small deviations from the predictions of the CKM mechanism.

1.2 CPV in meson systems

CPV is searched for in different processes [6]: meson decays (where evidence of CPV was found first in 1964 in neutral meson decay [8]), neutrinos oscillation and electric dipole moments. Precise measurements of CPV in mesons decay give constraints on SM parameters and probe new physics.

CP violation was first observed in the decay of neutral kaons and the studies have continued on all flavoured mesons that decay through weak interaction, where the CPV could be observed. These mesons are the lighter ones for each flavour content (K, D, B and B_s both charged and neutral) since those heavier than the latter decay via strong or electromagnetic interaction.

Three types of CPV effects are identified in meson systems:

- CPV in the decay
- CPV in the mixing process (discussed in the next section)
- CPV in the interference between decays with and without mixing.

The last two refers only to neutral mesons, the charged ones can only have CPV in the decay. While the formalism is the same for any pseudo-scalar meson, the phenomenology is different because of the unalike quark composition. Thus the appropriate approaches to the physical analysis need to be different, in particular for neutral mesons [9].

The main difference of the K meson is its lower mass that narrows the number of possible final states with respect to charmed and beauty systems. While the D meson differs from the others since it is the only one that involves an up-type quark, that makes their behavior in some measure different.

At the moment, CPV is well established in K and B meson decay: for the K meson all three types have been observed in the decay $K \to \pi\pi$, while for the B meson direct CPV was observed in $B^0 \to K^+\pi^-$ and CPV in interference in the decay $B^0 \to J/\psi K_S$. An evidence of CPV was recently discovered at the LHCb experiment in neutral D mesons. The measurement of the difference ΔA_{CP} of the CP asymmetry between the decays $D^0 \to K^+K^-$ [10] and $D^0 \to \pi^+\pi^-$ was found to be at 3σ from the SM prediction [11] . Many channels are still under investigation with direct CPV measurements.

1.2.1 Neutral meson mixing

Neutral meson mixing is a possible process for the K^0, D^0, B^0 and B_s^0 mesons (and their antiparticles). It consists in the oscillation of the flavour eigenstates trough weak interaction, thus changing the sign of their flavour quantum number, since they differ from the mass eigenstates. Since the formalism is the same for the four of them, it will be discussed using the general notation M^0 to indicate the neutral meson. In the time evolution of the neutral meson M^0, a final state in $\overline{M}^0$ must be considered; these process can be divided in two types of diagrams: long distance diagram, the D^0 example is shown in Fig. 1.5 and short distance diagram or box diagram, two examples for the K^0 are shown in the diagram in Fig. 1.4. This process is called mixing and, assuming CPT, it

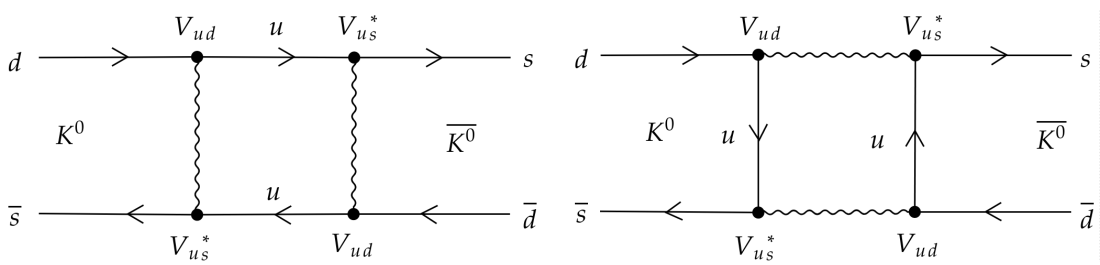

Figure 1.4: Examples of Feynman diagram for the $K^0 - \overline{K}^0$ mixing process through the exchange of virtual Ws, similar diagrams contribute to the mixing process where in the box instead of an u quark there is a c or t quark.

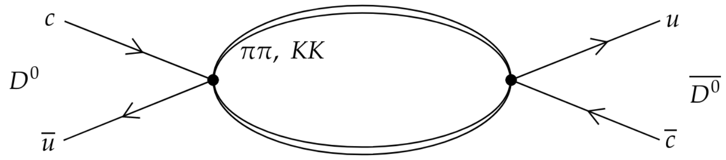

Figure 1.5: Feynman diagram of the D^0 mixing process with the exchange of real particles. This kind of process is less important (and usually neglected) in the K neutral system due to its lower energy.

is described by the effective Hamiltonian:

$$\mathcal{H} = \mathbf{M} - \frac{i}{2}\mathbf{\Gamma} = \begin{pmatrix} M & M_{12} \\ M_{12}^* & M \end{pmatrix} - \frac{i}{2}\begin{pmatrix} \Gamma & \Gamma_{12} \\ \Gamma_{12}^* & \Gamma \end{pmatrix} \tag{1.9}$$

where the diagonal elements of the mass ($\mathbf{M}$) and the decay ($\mathbf{\Gamma}$) hermitian matrices are real number and are associated with the flavour conserving transition ($\Delta F = 0$), while the off-diagonal terms refer to flavour changing transition $M^0 \leftrightarrow \overline{M}^0$ ($\Delta F = 2$). The eigenstates of $\mathcal{H}$ are the mass eigenstates M_L and M_H, and they evolve as free particles:

$$|M_{L,H}(t)\rangle = e^{-i\lambda_{L,H}t} |M_{L,H}(0)\rangle . \tag{1.10}$$

M_L refers to the lighter one and M_H to the heavier and their composition in terms of M^0 and $\overline{M}^0$, they can be expressed as:

$$\begin{aligned} |M_L\rangle &\propto p\,|M^0\rangle + q\left|\overline{M}^0\right\rangle \\ |M_H\rangle &\propto p\,|M^0\rangle - q\left|\overline{M}^0\right\rangle . \end{aligned} \tag{1.11}$$

The masses and decay widths of these states are defined respectively by the real and imaginary part of the associated eigenvalue:

$$\mathcal{H}\,|M_{H,L}\rangle = \lambda_{H,L}\,|M_{H,L}\rangle \quad \lambda_{H,L} \equiv m_{H,L} - i\Gamma_{H,L}/2 \tag{1.12}$$

from where the mixing parameters x and y can be defined:

$$\begin{aligned} x &\equiv \tfrac{\Delta m}{\overline{\Gamma}}, & \Delta m &\equiv m_H - m_L = \mathcal{R}e(\lambda_H - \lambda_L), \\ y &\equiv \tfrac{\Delta\Gamma}{2\overline{\Gamma}}, & \Delta\Gamma &\equiv \Gamma_H - \Gamma_L = -2\mathcal{I}m(\lambda_H - \lambda_L). \end{aligned} \tag{1.13}$$

where $\overline{\Gamma}$ is the average between Γ_H and Γ_L.

By solving the eigenvalue problem for $\mathcal{H}$ the following expression for the relation between p and q is found:

$$\left(\frac{q}{p}\right)^2 = \frac{\mathbf{M}_{12}^* - (i/2)\mathbf{\Gamma}_{12}^*}{\mathbf{M}_{12} - (i/2)\mathbf{\Gamma}_{12}} \tag{1.14}$$

If CP is a symmetry of $\mathcal{H}$ the ratio Γ_{12}/M_{12} is real and $\left|\frac{q}{p}\right| = 1$.

Using the evolution of free particle of M_H and M_L (Eq. 1.10) and their composition in terms of M^0 and $\overline{M}^0$ (Eq. 1.11), the time evolution of the neutral mesons in mixing is obtained:

$$\begin{cases} |M^0(t)\rangle = g_+\,|M^0\rangle + \frac{q}{p}g_-\left|\overline{M}^0\right\rangle \\ \left|\overline{M}^0(t)\right\rangle = \frac{p}{q}g_-\,|M^0\rangle + g_+\left|\overline{M}^0\right\rangle , \end{cases} \tag{1.15}$$

where

$$g_{\pm} = \frac{e^{-im_H t - \Gamma_H t/2} \pm e^{-im_L t - \Gamma_L t/2}}{2}. \tag{1.16}$$

Thus the probability to mix or to not are:

$$\begin{aligned} \mathcal{P}(M^0 \to \overline{M}^0) &= \left|\tfrac{q}{p}\right|^2 |g_-|^2 \\ \mathcal{P}(\overline{M}^0 \to M^0) &= \left|\tfrac{p}{q}\right|^2 |g_-|^2 \\ \mathcal{P}(M^0 \to M^0) = \mathcal{P}(\overline{M}^0 &\to \overline{M}^0) = |g_+|^2 , \end{aligned} \tag{1.17}$$

where $|g_{\pm}| = \frac{1}{2} e^{-\overline{\Gamma}t} \left[\cosh y\overline{\Gamma}t \pm \cos x\overline{\Gamma}t\right]$.

1.2.2 CP violation K, D, B and B_s systems

Given the flavour eigenstate M of a general meson (either charged or neutral), its amplitude into a final state f through weak interaction is defined as

$$A_f = \langle f | \mathcal{H}_W | M \rangle , \tag{1.18}$$

with $\mathcal{H}_W$ the Hamiltonian of weak interaction. Similarly:

$$\overline{A}_f = \langle f | \mathcal{H}_W |\overline{M} \rangle , \quad A_{\overline{f}} = \langle \overline{f} | \mathcal{H}_W | M \rangle , \quad \overline{A}_{\overline{f}} = \langle \overline{f} | \mathcal{H}_W | \overline{M} \rangle , \tag{1.19}$$

where the over-line indicates the antiparticle or the set of antiparticles. On these states, the application of the CP operator introduces a phase ψ depending on the flavour content of the state:

$$\begin{aligned} CP\,|M\rangle = e^{i\psi_M} |\overline{M}\rangle , \quad CP\,|\overline{M}\rangle = e^{-i\psi_M} |M\rangle , \\ CP\,|f\rangle = e^{i\psi_f} |\overline{f}\rangle , \quad CP\,|\overline{f}\rangle = e^{-i\psi_f} |f\rangle \end{aligned} \tag{1.20}$$

If CP is conserved in the decay $\overline{A}_{\overline{f}}$ and A_f have the same magnitude:

$$\overline{A}_{\overline{f}} = e^{i(\psi_f - \psi_M)} A_f \quad \Rightarrow \quad \left| \frac{\overline{A}_{\overline{f}}}{A_f} \right| = 1 \tag{1.21}$$

CP violation in the decay The CP asymmetry in decay is define by $|\overline{A}_{\overline{f}}/A_f| \neq 1$. In charge meson decay, where there is are no mixing effect, this is the only source of CP violation, and it's usually measured using

$$\mathcal{A}_{CP} \equiv \frac{\Gamma(M^- \to f^-) - \Gamma(M^+ \to f^+)}{\Gamma(M^- \to f^-) + \Gamma(M^+ \to f^+)}. \tag{1.22}$$

To observe CPV in decays, at least two amplitudes with different phases are required to contribute to the decay, otherwise the absolute value nullify their effect.

CPV in mixing CPV in mixing is defined by

$$\left| \frac{q}{p} \right| \neq 1, \tag{1.23}$$

and therefore $\mathcal{P}(M^0 \to \overline{M}^0)\mathcal{P}(\overline{M}^0 \to M^0)$ (from Eq. 1.17). When CPV is present in mixing three different eigenstates need to be considered for the meson systems: the flavour eigenstates (K^0 and $\overline{K}^0$ for the kaon system), the CP eigenstates (K_1 and K_2) and the mass eigenstates (K_S is the lighter and K_L is the heavier).

CPV in interference between decays with and without mixing The third kind of CP asymmetry is found in the interference between a decay without mixing, $M^0 \to f$, and one with it, $M^0 \to \overline{M}^0 \to f$ (Fig.1.6), where f need to be a common final state for M^0 and $\overline{M}^0$. In this case the CP violation is defined by

$$\mathcal{I}m\left(\frac{q}{p}\frac{\overline{A}_f}{A_f}\right) \neq 0. \tag{1.24}$$

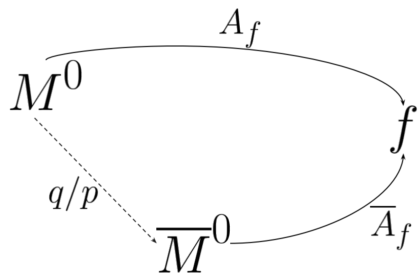

Figure 1.6: Diagram on how mixing can interfere with the decay.

1.2.3 Comparison among systems

As mentioned before, there are some differences between K, D, B and B_s systems arising from their different quark components. Fig. 1.7 gives a graphical representation of the masses and width of the mass eigenstates in the four neutral meson systems, while in Tab. 1.1 their mixing parameters are reported.

Table 1.1: The measured value of the mixing parameters x and y for the K [6], D, B and B_s [13] neutral meson systems.

Meson	x	y
K^0	0.95	0.997
D^0	0.0041	0.0062
B^0	0.80	0.001
B_s^0	27	0.064

Neutral kaons have both x and y near 1, resulting in an accessible oscillation frequency and two mass eigenstates with vastly different lifetimes The D meson system is the only one where the mixing parameters are both significantly less than 1 and the two curves in Fig. 1.7 are overlapped. The B systems have high values of the x parameter, in particular B_s have such big oscillation frequency that it's difficult to measure experimentally. In Fig. 1.8 the probability functions for the four neutral meson systems coming from Eq. 1.17 show the different oscillation frequencies in the four systems.

Given their much shorter lifetime, D and B mesons are more suitable for time dependent CPV measurements than the K meson. In B and D meson the CP violation in mixing is small and usually neglected.

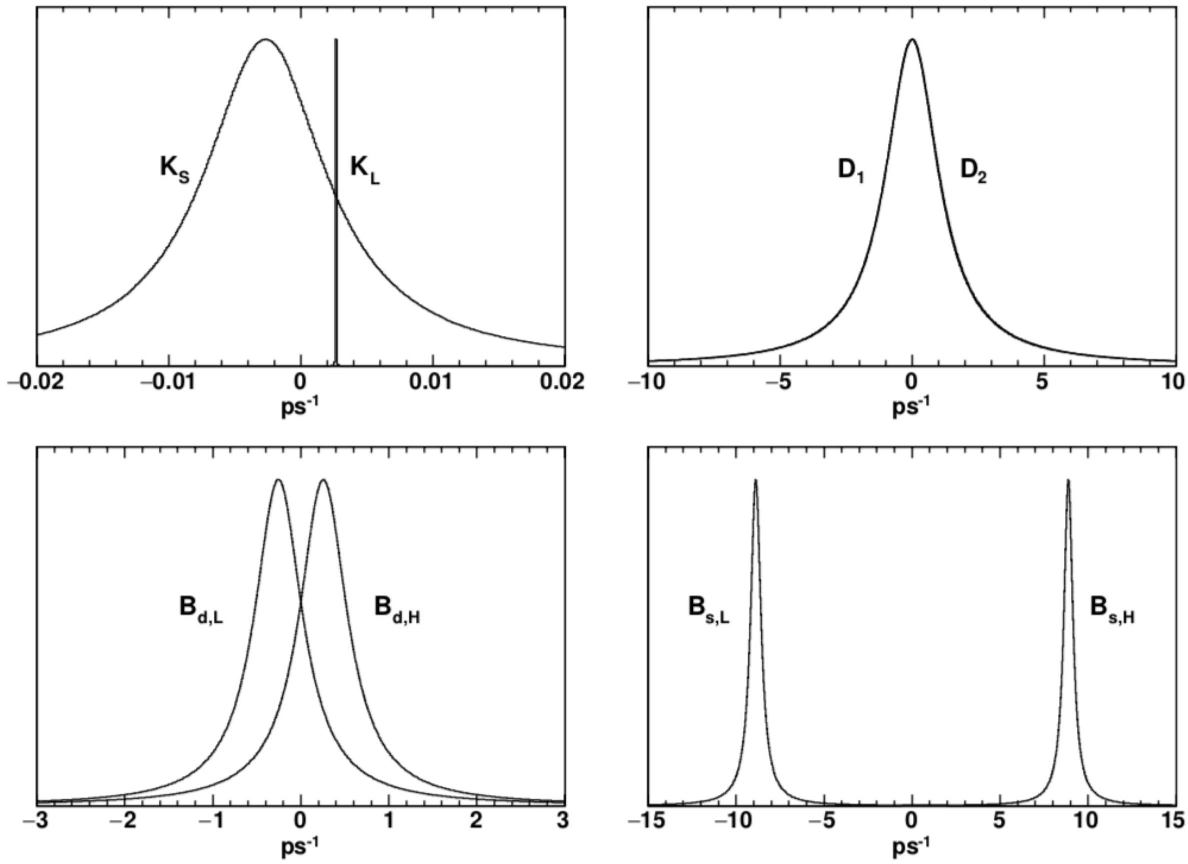

Figure 1.7: A visual representation of the masses and width differences of the mass eigenstate of the neutral mesons. The plots come from [12].

1.3 CPV measurements at Belle II in meson decays with a K_S

At Belle II the study of CP violation [5] is mainly carried forward in charmed and beauty meson decays where precise measurements of the unitarity triangle and CPV in charm are made. As said before, the level of CP violation within the Standard Model's quark sector is insufficient to account for the observed baryon-antibaryon asymmetry in the Universe; interesting measurements come from time dependent CPV analyses in penguin transitions involving $b \to s$ and $b \to d$ quarks. Additionally, exploring CP violation in charm mixing, which is very small in the SM, gives access to possible contribution beyond the SM in the realm of the up-type sector.

Researchers are seeking a new mechanism responsible for generating the matter-antimatter imbalance, beyond the one contained in the Standard Model and described by the CKM matrix. In the bottom and charm sectors at Belle II, for instance, there are measurements in the channels $B^0 \to J/\psi K_S^0$, $B^0 \to K_S^0\pi^0$, $D^0 \to K_S^0\pi\pi$, for CPV and time-dependent mixing measurements and, concerning integrated CPV measurements over time, $D^0 \to K_S^0 K_S^0$. Given the topic of my thesis project I reported only some measurements with a K_S in the final state.

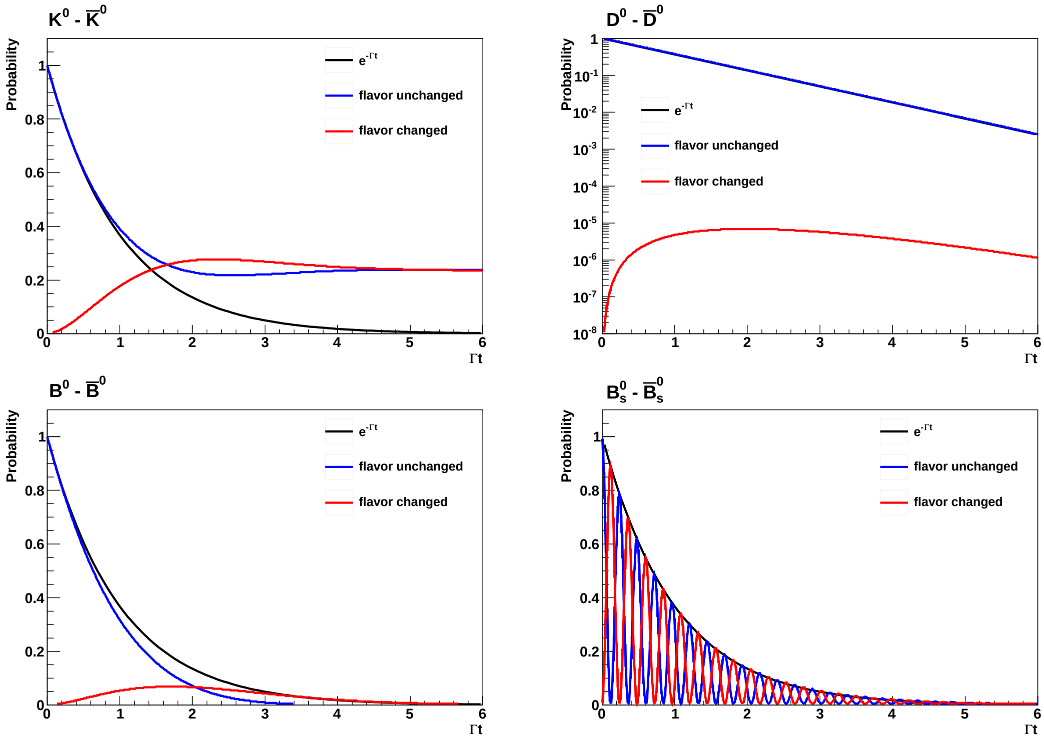

Figure 1.8: Flavour-changing (red) and flavour-unchanging (blue) probability functions for the four neutral meson systems. The plot are taken from [14].

1.3.1 Time dependent $\sin 2\beta$ measurements

In the decay chain $\Upsilon(4S) \to B^0\overline{B}^0 \to B_{CP}B_{tag}$ one of the B mesons decays at time t_{CP} to a CP eigenstate B_{CP} , and the other B meson decays at time t_{tag} to a final state that allows to distinguish if the B_{tag} was a B^0 and a $\overline{B}^0$. Both the times t_{tag} and t_{CP} are the proper times of the two mesons. The decay rate of B_{CP} has a time dependence given by:

$$\mathcal{P}(\Delta t, q) = \frac{e^{|\Delta t|/\tau_{B^0}}}{4\tau_{B^0}} \{1 + q\,[S \sin \Delta m_d \Delta t + C \cos \Delta m_d \Delta t]\} \tag{1.25}$$

where S and C are the CP violation parameters, τ_{B_0} is the B^0 lifetime, Δm_d is the mass difference between the two neutral B mass eigenstates, which corresponds to the oscillation frequency, $\Delta t \equiv t_{CP} - t_{tag}$, and $q = +1(-1)$ corresponds to $B_{tag} = B^0(\overline{B}^0)$.

The key observables are C and mostly S: the SM predicts $C = 0$ and $S = \sin 2\beta$, where β is an angle of the CKM unitary triangle (see Fig. 1.2);

This kind of measurement is done in different channels at Belle II some examples are $B^0 \to J/\psi K^0_S$, $B^0 \to \Phi K^0_S$ and $B^0 \to K^0_S\pi^0$. The recent results are reported in the Tab. 1.2.

1.3.2 Time integrated γ measurement

The angle γ, the angle of the unitarity triangle defined as $\arg(V_{ud}V^*_{ub}/V_{cd}V^*_{cb})$, is measurable via the interference of the tree-level quark transitions $\overline{b} \to \overline{c}u\overline{s}$ and $\overline{b} \to \overline{u}c\overline{s}$, which involve the emission of a W^+ boson from the $\overline{b}$ quark, the Feynman diagram is reported in Fig. 1.9.

Table 1.2: Results of the CPV analysis for the $B \to J/\psi K^0_S$, $B \to \Phi K^0_S$ and $B^0 \to K^0_S\pi^0$ decays performed at Belle II.

channel	S	C	ref.
$B \to J/\psi K^0_S$	$0.724 \pm 0.035 \pm 0.014$	$-0.035 \pm 0.026 \pm 0.013$	[15]
$B \to \Phi K^0_S$	$0.54 \pm 0.26^{+0.06}_{-0.08}$	$-0.31 \pm 0.20 \pm 0.05$	[16]
$B^0 \to K^0_S\pi^0$	$0.75^{+0.20}_{-0.23} \pm 0.04$	$-0.04^{+0.14}_{-0.15} \pm 0.05$	[17]

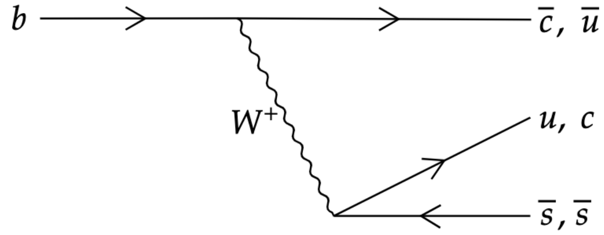

Figure 1.9: An example of a Feynman diagram of the tree-level quark transitions $\bar{b} \to \bar{c}u\bar{s}$ and $\bar{b} \to \bar{u}c\bar{s}$.

The tree-level nature of these transitions results in negligible theoretical uncertainties when interpreting the measured observables in terms of γ. Therefore, assuming the absence of new physics at tree level, the measurement of γ provides a strong test of the SM when compared to indirect determinations. The decay mode $B^+ \to D(K^0_S h^+h^-)h^+$ allows a complicated model-independent method to determine γ (for more detail see [18]). Using Belle and Belle II data, the Belle II collaboration found $\gamma = (78.4 \pm 11.4 \pm 0.5 \pm 1.0)^\circ$, where the first uncertainty is statistical, the second is the experimental systematic uncertainty and the third is from the uncertainties on external measurements of the D-decay strong-phase parameters.

1.3.3 CPV in charm

In the charm sector many channels are under investigation with direct CPV measurements. The objective is the measurement of the CP asymmetry $\mathcal{A}_{CP}$ as defined in Eq. 1.22, however experimentally a quantity called raw asymmetry is measured:

$$\mathcal{A}_{RAW} = \frac{N_{D^0} - N_{\overline{D^0}}}{N_{D^0} + N_{\overline{D^0}}}, \tag{1.26}$$

where $N_{\overset{(-)}{D^0}}$ is number of reconstructed $\overset{(-)}{D^0}$ in the signal channel. The raw asymmetry is not exactly equal to $\mathcal{A}_{CP}$, but it has more components, in case of small asymmetry $\mathcal{A}_{RAW}$ can be expressed as:

$$\mathcal{A}_{RAW} = \mathcal{A}_{CP} + \mathcal{A}_{det} + \mathcal{A}_{FB} \tag{1.27}$$

The detection asymmetry $\mathcal{A}_{det}$ is related to the reconstruction of the slow pion $\pi_s^\pm$ used to tag the D^0 or $\overline{D^0}$:

$$D^{\pm *} \to \pi_s^\pm \overset{(-)}{D^0}. \tag{1.28}$$

There is an asymmetry in the π^+ and π^- reconstruction due to the fact that the detector is made of matter, thus causing an asymmetry in the D^0 and $\overline{D^0}$ samples. The production asymmetry, called forward-backward asymmetry at Belle II, $\mathcal{A}_{FB}$, is related to the acceptance of the detector coupled to the asymmetric production of D^0 and $\overline{D^0}$ in the CM polar angle θ^*. To measure $\mathcal{A}_{CP}$ from $\mathcal{A}_{RAW}$, the other nuisance asymmetries need to be corrected for. The detection asymmetry is usually measured on data on control channels, while $\mathcal{A}_{FB}$ can be cancelled using its property to be odd in θ^*, while $\mathcal{A}_{CP}$ is independent of it. Singly Cabibbo-suppressed (SCS) decays are of special interest as the possibility of interference with NP amplitudes could lead to larger CPV than predicted by SM, the $D^0 \rightarrow K_S^0 K_S^0$ decay is one such channels. In 2017 an analysis of CP direct violation was published with Belle data with the result $\mathcal{A}_{CP} = (-0.02 \pm 1.53 \pm 0.17)\%$.The most precise measurement up to date in this channel was performed at the LHCb experiment with the result $\mathcal{A}_{CP} = (-3.1 \pm 1.2 \pm 0.5)\%$ [19].

Chapter 2

Super-KEKB and the Belle II experiment

The Belle II experiment is located at the KEK laboratories in Tsukuba, Japan. Here, the SuperKEKB accelerator run since 2019 and it is currently in its second run. The Belle II detector has a state-of-the-art silicon tracking detector able to make time-dependent CPV measurements. In this chapter a brief description of the SuperKEKB accelerator and of the Belle II detector is provided, with a focus on the Silicon Vertex Detector (SVD).

The accelerator is described and the differences with its predecessor, KEKB, are reported, highlighting how the increase of luminosity is implemented. Additionally, a concise description of the backgrounds caused by the beams is also reported, with a particular focus on their impact on the SVD detector.

Concerning the detector itself, each sub-detector is briefly presented, with special attention dedicated to the SVD, offering a more detailed examination of its design and performance. At the end, the software framework of Belle II is introduced and the SVD reconstruction discussed.

2.1 B-factory

In the search for physics beyond the SM, B-factories, such as SuperKEKB [20, 21, 22], are working at the intensity frontier, searching for deviations from the SM predictions or for rare physics reactions.

The SuperKEKB accelerator, shown in Fig. 2.1, collides 7 GeV electrons with 4 GeV positrons, resulting in center-of-mass (CM) energies in the region of the Υ resonances; the range of beam energies covers from the $\Upsilon(1S)$ to the $\Upsilon(6S)$ resonance states according to the SuperKEKB design [23]. For physics operation the majority of the data are taken at the $\Upsilon(4S)$ resonance ($m_{\Upsilon(4S)} = 10.58\,\mathrm{GeVc^{-2}}$), that decays in a $B\overline{B}$ entangled pair. Tab. 2.1 reports the production cross section of this process together with others of interest for physics analysis.

The asymmetric beam provides a $\beta\gamma = 0.28$ boost of the CM system that allows for time-dependent CP violation measurements. It is lower than at KEKB ($\beta\gamma = 0.42$) and, therefore it requires better vertex reconstruction resolution. Nonetheless it is advantageous for analysis with neutrinos in the final state that requires good detector hermeticity.

The two beams do not collide head-on, but with at a crossing angle $2\phi = 83\,\mathrm{mrad}$, as shown in Fig. 2.2, to avoid the hour-glass effect. The crossing angle reduces the size of the interaction region, that is not anymore dominated by the length of the bunches (σ_z)

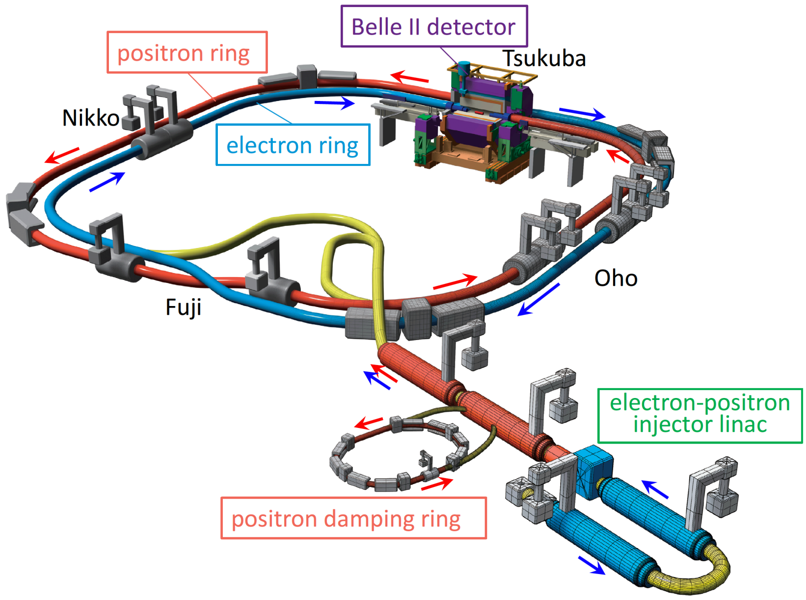

Figure 2.1: Scheme of the SuperKEKB accelerator. The rings, built in the KEKB tunnel, have a circumference of approximately 3 km: the HER (high-energy ring) hosts bunches of electrons and the LER (low-energy ring) bunches of positrons.

like for head-on collisions, but by the following quantities (assuming the same horizontal size σ_x^* for the two beams):

$$\begin{aligned} a &= \frac{\sigma_x^*}{\sin 2\phi}\sqrt{2 - 2\cos 2\phi} \simeq 10\,\mu\text{m} \\ b &= \frac{\sigma_x^*}{\sin 2\phi}\sqrt{2 + 2\cos 2\phi} \simeq 247\,\mu\text{m}. \end{aligned} \tag{2.1}$$

The relatively large crossing angle also allows [24]:

- a new final focusing system with superconducting quadrupole magnets (QCS) to reside closer to the interaction point (IP)
- separate beamlines for the HER (high-energy ring) and LER (low-energy ring).

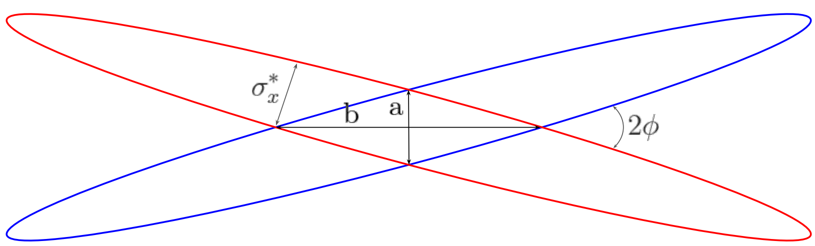

Figure 2.2: Top view of the collision of the two beams with a crossing angle.

The main goal of the SuperKEKB upgrade over KEKB is to increase the luminosity. The luminosity is an important parameter of colliders: it represents the interaction rate per unit cross section for colliding particles. It can be expressed as:

$$L = \frac{N_{e^+} N_{e^-} f}{4\pi\sigma_x^*\sigma_y^*} R_L, \tag{2.2}$$

Table 2.1: Production cross sections of $b\bar{b}$, $c\bar{c}$ and $\tau^+\tau^-$ events from the collision of electrons with positrons at the CM energy of the $\Upsilon(4S)$. The cross section for the scattering of the electron and the positron (Bhabha scattering) is reported for comparison since it is the highest one in such collisions and it's the main source of luminosity background, see section 2.1.2 for more details.

Process		σ [nb]	
$e^+e^- \to b\bar{b}$	$B^0\overline{B^0}$	0.5654	
	B^+B^-	0.5346	
$e^+e^- \to c\bar{c}$		1.329	(full angle)
$e^+e^- \to \tau\tau(\gamma)$		0.919 ± 0.003	(full angle)
$e^+e^- \to e^+e^-(\gamma)$		294 ± 2	$([10, 170]^\circ)$

where $N_{e+(-)}$ is the number of positrons (electrons) in a bunch, f is the collision frequency of the bunches (number of bunches multiplied by the rotation frequency), $\sigma^*_{x(y)}$ is the horizontal (vertical) beam size at the IP and R_L is the reduction factor due to the crossing angle and the hourglass effect.

SuperKEKB has a design luminosity of $6 \cdot 10^{35}\text{cm}^{-2}\text{s}^{-1}$, about 30 times larger that of KEKB's recorded peak. To reach such target, an innovative *nano-beam* scheme is implemented: it consists in the reduction of the beam size (proportional to $\sigma^*_{x(y)}$) at the collision point (IP) by a factor of 20, from about 1 µm to 50 nm vertically (σ^*_y), and in increasing the currents (proportional to $N_{e+(-)}$ and f) by a factor of 2, compared to the KEKB values [5]. The concept of the luminosity increase strategy is illustrated in Fig. 2.3.

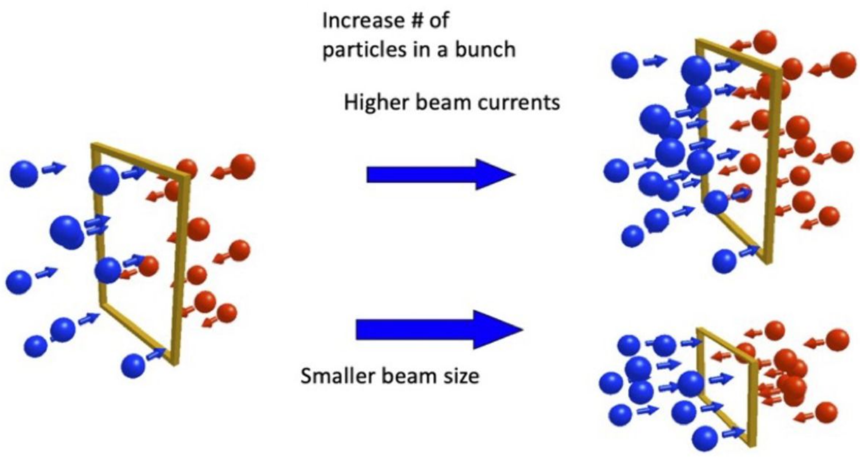

Figure 2.3: Representation of the approach taken at SuperKEKB to increase luminosity: a higher beam current and a smaller beam size increase the density of the number of particles in a bunch. The image is taken from [25].

In Fig. 2.4 the measured luminosity and average current of KEKB and the first stage of SuperKEKB are compared: even with a smaller current SuperKEKB has surpassed KEKB peak luminosity in less than a year

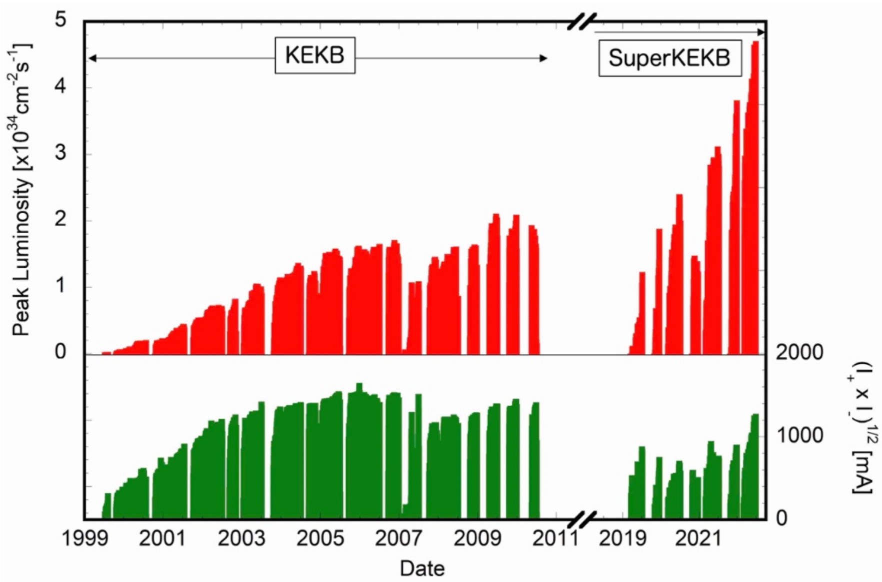

Figure 2.4: The peak luminosity and average beam currents in the HER and LER of KEKB and SuperKEKB [25].

2.1.1 Data taking

From the start of the experiment in 2019, Belle II has recorded an integrated luminosity of 488.02 fb^{-1}, as shown in Fig. 2.5. During Run 1 (2019-2022) 424 fb^{-1} were recorded: 363 fb^{-1} at the $\Upsilon(4S)$ resonance, 42 fb^{-1} off resonance (60 MeV below) and 19 fb^{-1} energy scan above resonance ($[10.6, 10.8]$ GeV). In June 2022, SuperKEKB achieved the record instant luminosity of $4.7 \cdot 10^{34}\mathrm{cm}^{-2}\mathrm{s}^{-1}$, even with smaller beam currents than those used at KEKB[25].

In 2022 operations stopped for the long shutdown 1 (LS1). The main purpose of LS1 was the full installation of the PiXel Detector (PXD) that was missing most of its second layer; the detector was opened and the VerteX Detector (VXD) was extracted and then reassemble: the PXD and the piece of beam pipe attached to it were completely replace with new ones, while rest of it was maintained. Other improvements were made in the CDC, additionally the maintenance of the machine has been performed.

2.1.2 Beam background

The intense luminosity of SuperKEKB causes high beam induced background [24, 27] that the detector and the software are required to tolerate. When beam particles deviate from the nominal orbit, they hit the beam pipe's inner wall generating shower particles; if those showers reach the Belle II detector its dose and hit rates increase.

This is the so-called *beam (induced) background* and it complicates the accurate reconstruction of events due to the increased rate, affecting the software performance in terms of efficiency, purity, and time consumption.

There are different sources of beam background at SuperKEKB:

- those coming from each single beam: Touschek scattering, Beam-gas scattering, and Synchrotron radiation

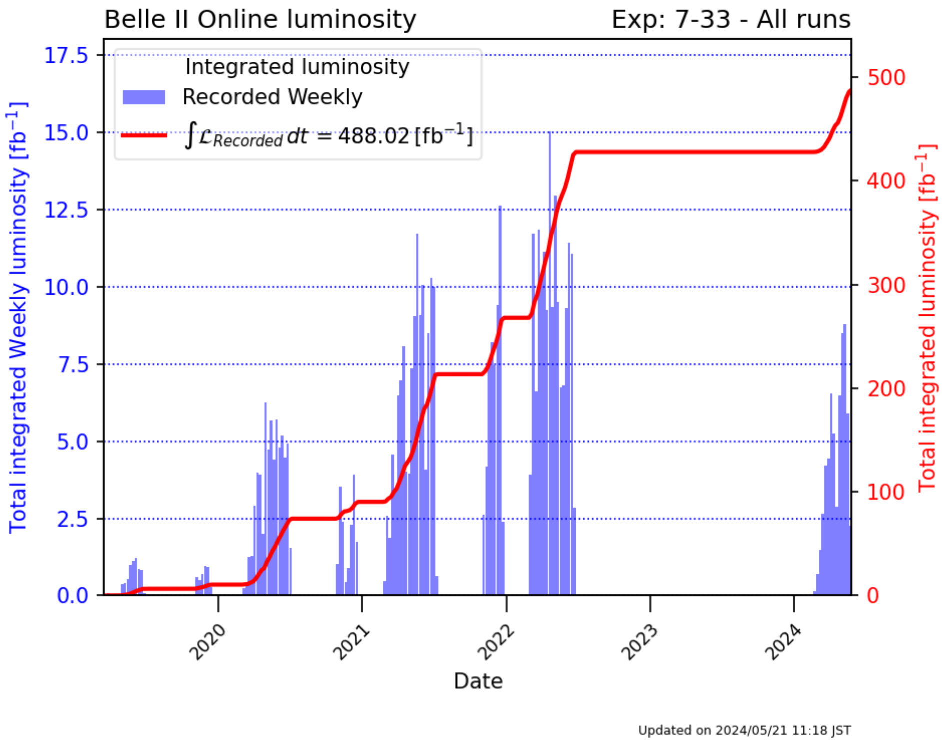

Figure 2.5: The weekly and total integrated luminosity of SuperKEKB, from the start of the Belle II experiment till now (21th May 2024); from July 2022 to March 2024 the operations stopped for the Long Shutdown one (LS1) [26].

- those dependent from the luminosity: radiative Bhabha process and two photon process
- others: injection background and background from Sudden Beam Loss (SBL).

According to beam background simulation in Run 1 the most important sources are Touschek scattering and beam–gas interactions from the LER.

Touschek scattering The Touschek effect occurs when Coulomb scattering between two particles of the same bunch causes their energies to deviate from the nominal energy. These particles are eventually lost by hitting the beam pipe inner wall while they propagate along the ring, producing an electromagnetic shower. The Touschek background rate is parameterized as

$$\mathcal{O}_T = T\frac{I^2}{\sigma_y n_b}, \tag{2.3}$$

where I is the beam current, n_b is the number of bunches, σ_y is the vertical beam size and T is the constant corresponding to the Touschek background rate per unit beam parameters. This effect is amplified by the 'nano-beam' scheme since the reduction of the beam size obviously increases the interaction probability of two particles from the same bunch: simple extrapolation based on beam size predicts that the Touschek background at SuperKEKB will be a factor of ~ 20 higher than at KEKB. To mitigate Touschek background, collimators and metal shields are located at different positions around the ring.

Beam-gas scattering When residuals of gas molecules are present in the beam pipe, there are two main processes that can cause background by scattering: Coulomb scattering, which changes the direction of the beam particles, and Bremsstrahlung scattering, which decreases their energy. Beam-gas scattered particles are lost like the Touschek-scattered particles, by hitting the beam pipe. Collimators and metal shields are useful to reduce this background as well, horizontal collimators suppress bremsstrahlung scattering and vertical collimators reduce Coulomb scattering. The rate of beam-gas scattering is proportional to the beam current I and to the vacuum pressure P in the beam pipe:

$$\mathcal{O}_B = BIP, \tag{2.4}$$

where B is the constant of proportionality. The rate of Beam-gas Bremsstrahlung losses is negligible compared to the Touschek loss rate in the detector. However, the beam-gas Coulomb scattering rate is expected to be a factor of ~ 100 higher than at KEKB, because the SuperKEKB beam pipe radius inside the detector is smaller and the current is higher.

Synchrotron radiation When high energy electrons (or positrons) are forced to curve, they emit a radiation, called synchrotron radiation (SR) in a modern circular accelerator. Since the SR power is proportional to the beam energy squared and magnetic field strength squared, the HER beam is the main source of this type of background. To absorb SR photons before they reach the Belle II inner detectors and damage them, the inner surface of the beryllium beam pipe is coated with a gold layer, and ridge structures on the inner surface of incoming pipes prevent scattered photons from reaching the interaction point.

Radiative Bhabha process The Bhabha scattering is the electron-positron scattering process $ee \to ee(\gamma)$. Photons produced by the radiative Bhabha process propagate along the beam axis direction and interact with the iron of magnets. In these interactions, there is a very large production rate of neutrons or low energy gamma rays. The rate of neutron production by radiative Bhabha events is proportional to the luminosity, so it is expected to be ~ 30 times higher than KEKB once the nominal luminosity is achieved. Additional neutron shielding in the accelerator tunnel is required to stop these neutrons. Meanwhile the low energy gamma rays are a significant source of background in the central drift chamber (CDC) and in the Time-Of-Propagation counter(TOP).

Two photon process In a two-photon process $ee \to e\gamma e\gamma \to eeee$ electron-positron pairs are produced at very low momentum. Such pairs spiral around the solenoid field lines leaving multiple hits in the Belle II inner detectors. In addition to the emitted pairs, primary particles lose large amounts of energy or scatter with a large angle and they can be lost inside the detector.

Injection background During physics data taking when the total beam current is 1% below the nominal beam current, charge is injected into buckets with low bunch-current. This generates an increase in background rate for a few milliseconds. To avoid the saturation of the readout, trigger vetoes are applied leading to a dead time in data acquisition and therefore a reduction in recorded luminosity.

Large beam loss accidents The stored beam sometimes becomes unstable to the point of causing sudden large beam losses. These occurrences in Run 1 were particularly common when the beam current was above 0.5 A. One potential explanation for these incidents is the presence of dust particles trapped within the beam pipe; however analysis is still ongoing. This is a catastrophic event that can damage heavily the detector.

2.2 Detector

Like every collider experiment, Belle II has various detectors arranged in cylindrical layers around the beam pipe. Given the cylindrical structure it is natural to use cylindrical or spherical coordinate:

$$\begin{cases} x = r\sin\theta\cos\varphi \\ y = r\sin\theta\sin\varphi \\ z = r\cos\theta \end{cases} \tag{2.5}$$

where the origin is where the two beams collide nominally, the z axis is the direction of the magnetic field along the length of the detector, the y axis goes upwards perpendicular to the soil and the x axis is parallel to the soil and point towards the outside of the SuperKEKB ring; Fig. 2.6 shows the coordinate system with respect to the detector.

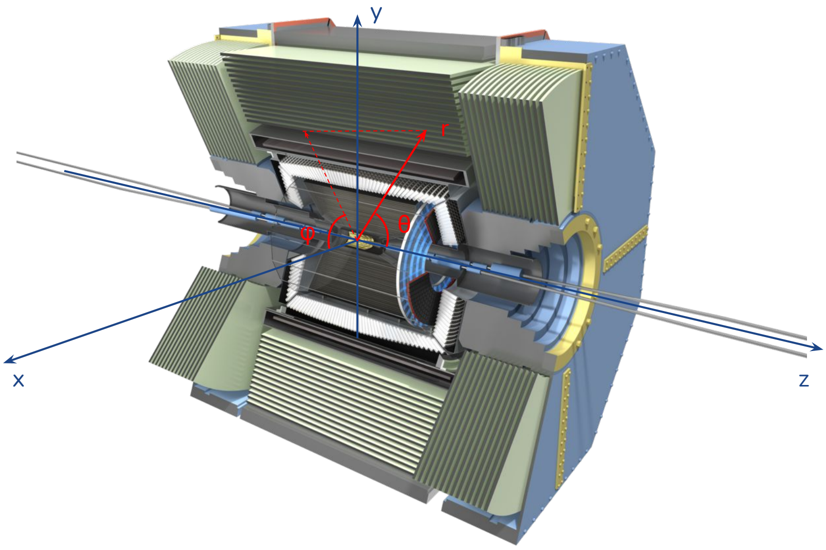

Figure 2.6: Coordinate frame in Belle II: in blue Cartesian coordinates and in red spherical ones. The x axis in this image is drawn in the opposite direction than it should be, the correct direction is toward the outside of the ring.

The main components of the Belle II detector are:

- the vertex detector (VXD)
- the central drift chamber (CDC)
- the particle identification sub-detectors (TOP and ARICH)
- the electromagnetic calorimeter (ECL)
- the superconducting solenoid magnet ($\vec{B} = 1.5\,\mathrm{T}\hat{z}$)
- the K^0_L and muon detector (KLM)

◇ the trigger and the DAQ system

In the following sections a brief description of the Belle II detector is reported, a more detailed one can be found in the *Belle II technical design report* [28].

2.2.1 VerteX Detector

The VerteX Detector (VXD), shown in Fig. 2.9 on the left, is composed of two sub-detectors: the silicon PiXel Detector (PXD), in Fig. 2.9 on the right, and the Silicon Vertex Detector (SVD). The six silicon layers composing the VXD are organized in ladder and sensor, as shown in Fig.2.8.

The layers are placed at different transverse distances from the beam axis, starting at 14 mm and finishing at 135 mm (the beam pipe has a 10 mm radius). The ladders, placed around the beam axis, along the φ coordinate. The sensors are placed along the beam axis (z coordinate). The ladders of the VXD are overlapped to cover completely the φ angle, while the acceptance on the polar angle θ is from 17° to 150°. This detector plays a crucial role in the tracking reconstruction, in particular the PXD allows a precise measurement of primary and secondary decay vertices and the SVD is very useful for low-momentum particle reconstruction, in track finding as well as in particle identification.

The PXD and SVD combined offer an average decay-time resolution of about 70 fs and 60 fs, respectively for the D^0 and D^+ proper times [29].

2.2.2 PiXel Detector

The PXD detector [30] is a self supporting structure composed of two layer of pixelated sensors, based on the Depleted P-channel Field Effect Transistor (DePFET) technology, which allows it to be very thin, about 75 µm, so that the material budget is kept very low to minimize multiple scattering: $\approx 0.2\% X_0$ for layer. The layers are placed at the distance of 14 mm and 22 mm from the beam axis and are comprised of 8 and 12 ladders respectively; in the PXD a ladder is formed by two PXD monolithic modules glued together with a joint introducing a 0.85 mm gap in the middle between the active areas. The sensitive region of each module consists of a matrix with 250 × 768 DePFET pixels, a summary table of the geometry of the sensor is reported in Tab. 2.2.

Table 2.2: Geometry summary of the PXD [5]. The smaller pixel are adopted in the region of the matrix closer to the interaction point.

	sensor size [mm^2]	pixel size [µm^2] a	b	n. ladders	d_T [cm]
Layer 1	15 × 136	50 × 50	50 × 60	8	1.4
Layer 2	15 × 170	50 × 75	50 × 85	12	2.2

The hit efficiency, defined has the ratio between the number of tracks with an associated hit and the total number of tracks intercepting the PXD sensors, in Run 1 for the PXD modules was 96% on average; not considering some known dead region caused by recent beam loss events, the hit efficiency was about 99%. The resolution of the transverse and longitudinal impact parameter of the track, coming from the PXD, was studied based on a small data sample collected in May 2019 and it was found to be (13.64 ± 0.08) µm

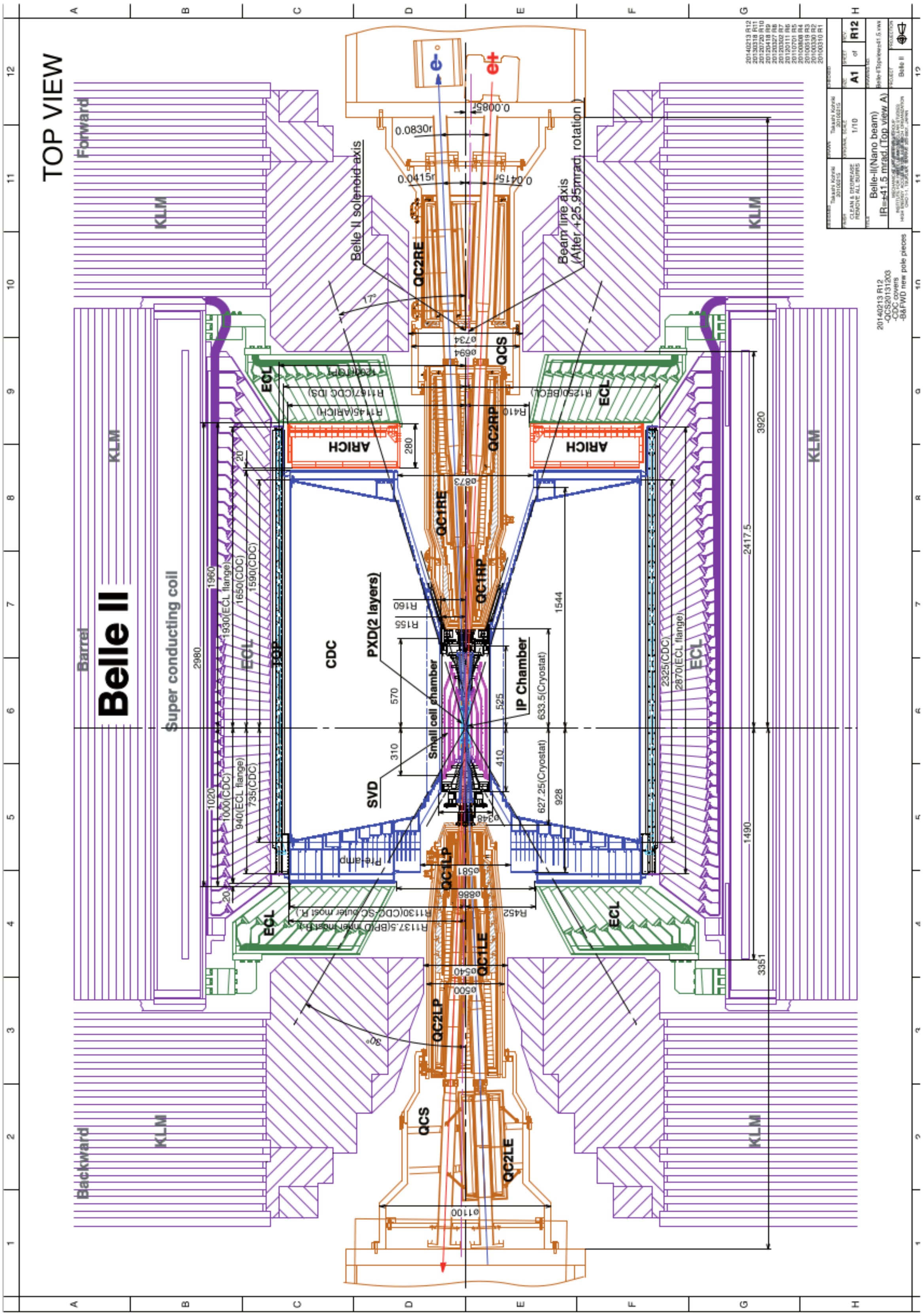

Figure 2.7: Belle II detector: it is about 10 m wide and just as high, it weighs 1500 tons.

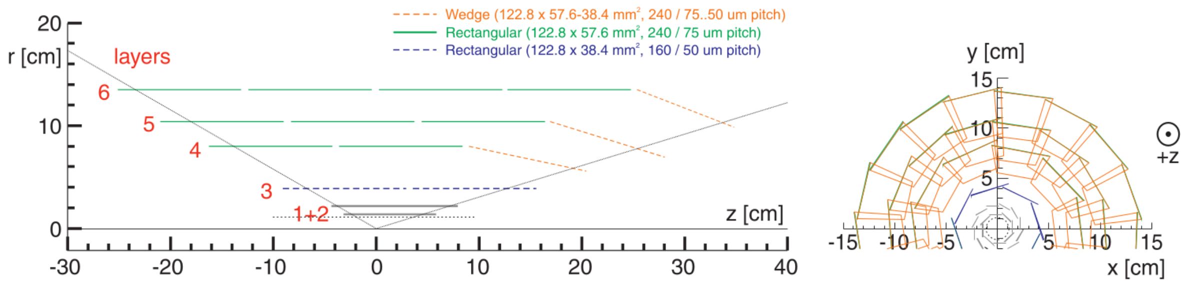

Figure 2.8: Lateral view of the VXD on the left and on the right the frontal view of SVD layers and ladders.

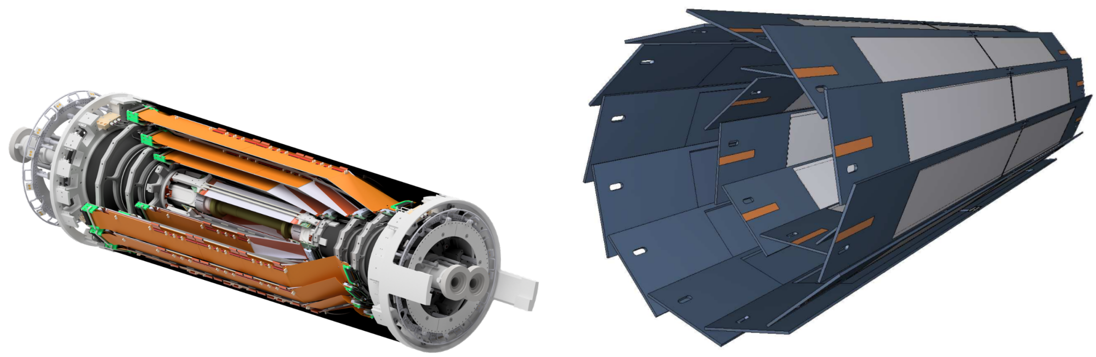

Figure 2.9: The VXD detector on the left and a zoom on the PXD on the right.

and $(14.92 \pm 0.07)\,\mu m$, respectively. During the recent LS1 that ended in February 2024, a new and complete PXD has been installed [29], till then the outer layer had only two over twelve ladders installed.

The PXD information is not an input for the HLT due to the high integration time needed by the rolling-shutter read out, it is about $20\,\mu s$. Instead regions of interest are identified for each track reconstructed by SVD and CDC detectors, and PXD hits from this region are saved in the raw data. A more complete description of tracking reconstruction is discussed in chapter 3.

2.2.3 Silicon Vertex Detector

The SVD [31, 32] consists of four layers of double-sided silicon strip sensors composed respectively of 7, 10, 12 and 16 ladders with 2, 3, 4 and 5 sensors each (Fig. 2.8). They are placed at the transverse distance of 3.9 cm, 8.0 cm, 10.4 cm, 13.5 cm respectively, as reported in Tab. 2.3.

Table 2.3: Geometry summary of the SVD.

	n. ladder	n. sensors	d_T [cm]	slant angle [°]
Layer 3	7	2	3.9	3.9
Layer 4	10	3	8.0	11.9
Layer 5	12	4	10.4	16.0
Layer 6	16	5	13.5	21.1

Each sensor has two sides: a p-side with r/φ strips and a n-side with z strips. The sensors have different shapes and dimensions, as shown in Fig. 2.10:

- small rectangular sensors with 768 readout strip on both sides and a readout pitch of 50(160)µm on p(n)-side, they used in the third layer
- big rectangular sensors used on the layer 4,5 and 6 with 768(512) readout strip the p(n)-side and 75(240)µm readout pitch on p(n)-side
- wedge-shaped sensors with 768(512) readout strip the p(n)-side and therefore the same readout pitch on p(n)-side as the big rectangular sensor, and $50 - 75(240)$µm readout pitch on n-side, they are used on the layer 4,5 and 6 in the forward region.

While the rectangular sensors maintain a straight alignment, the wedge shaped sensors are slanted, at 11.9, 16.0, and 21.1° angles, on the forward region of the SVD. This design choice minimizes material budget and the sensors' number while improving hit quality.

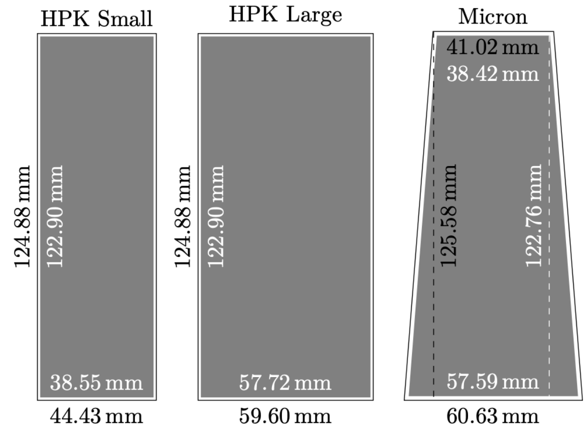

Figure 2.10: Shape of the silicon sensor of the SVD: the HPK small are used in the third layer, while the HPK large and the Micron are used in the fourth, fifth and sixth layers respectively in the barrel and forward region.

Rectangular sensors are 320 µm thick and slanted sensors 300 µm thick.

Each side of the sensor provides measurements on the position in local coordinates (called u and v), the collected charge and time of the hit.The p-side measures the u coordinate, corresponding to the φ global coordinate, while the n-side measures the v coordinate, corresponding to the z global coordinate. The local coordinate u and v are perpendicular to each other in every sensor except for the forward ones who have a trapezoidal shape. On these sensors, the u coordinate is a function of the v coordinate. There is a third local coordinate, w, representing the axis perpendicular to the (u, v) plane and it's not measured but is known by the position of the sensor and the orientation of its two sides. In layer 3 the v-side is facing the IP, while in all the other layers is the opposite, with the u-side that faces it. Combining the measurements coming from the two sides, one can get the 3D position of the hit.

The SVD readout electronics uses the APV25 chip, a technology originally developed for the CMS experiment [33]. Thanks to the *Origami* design developed for the Belle II SVD [34], the APV25 chips are installed on the same side of the sensor both for u and v strips for the central modules, thus allowing less material budget of the cooling system that needs to be only on that one side. The averaged material budget per layer of SVD is

0.7 % of a radiation length [35]. The APV25 chip shapes the signal coming from each of the 128 strips and provides to the Flash Analog/Digital Converter (FADC) six samples for each signal strip corresponding to the triggered event. The FADC digitizes the signals and applies the cut on signal-over-noise ratio to be > 3, to reduce the number of strips fired on electronic noise.

2.2.4 Central Drift Chamber

One of the core instruments of the Belle II spectrometer is the central tracking device, a large-volume (inner radius 160 mm, outer radius 1130 mm, length 2.3 m) drift chamber with small drift cells ($\sim 1 - 2$ cm). The chamber gas consists of 14336 sense wires arranged in 56 layers immersed in a $He : C_2H_6$ 50:50 mixture, as shown in Fig. 2.11. The combination of the wires' orientation, axial (aligned with the solenoidal magnetic field) or stereo (skewed with respect to the axial wires), allows to fully reconstruct three dimensional helix tracks. There are nine superlayer that alternate axial wires to stereo wires. Besides the information about the track, the CDC provides some particle identification by the measurement of energy loss.

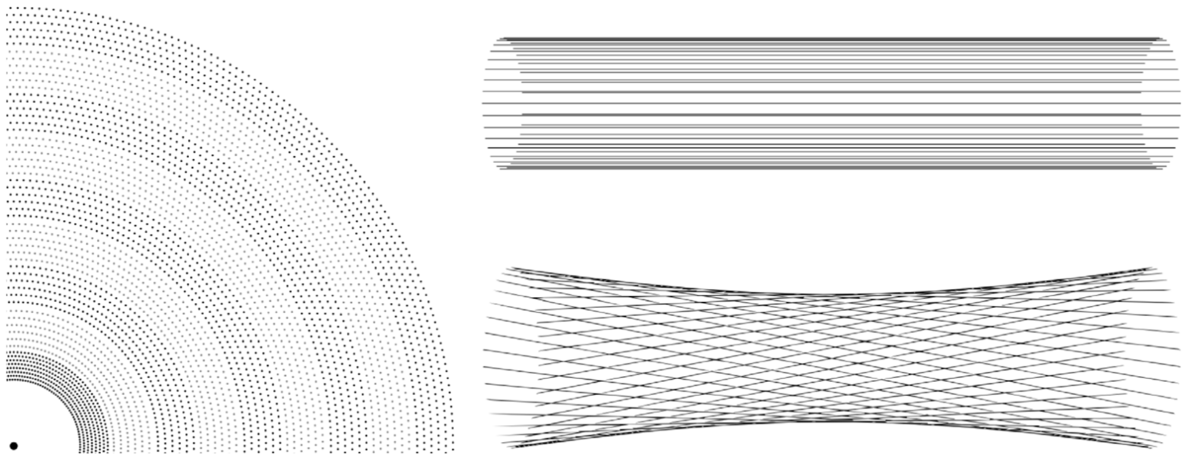

Figure 2.11: Geometry of the CDC. On the left the nine superlayer in which the wires are divided into are visible; it can be noticed that the first one has smaller cells. On the right a representation of the the difference between axial and stereo layer.

2.2.5 TOP and ARICH

For the particle identification there are two types of Cherenkov detector: a time-of-propagation counter (TOP) in the barrel region and a proximity focusing Cherenkov ring imaging detector (ARICH) in the forward end-cap region .

The TOP has 16 modules ($260 \times 45 \times 2\text{cm}^3$) composed of a quartz bar, drawn in Fig.2.12 with, at the end of the sensor, an expansion volume, about 10 cm long, that introduces some additional pinhole imaging, relaxes slightly the precision timing requirements, and reduces the hit occupancy at the photo-detector. At the exit window of the wedge, two rows of sixteen fast multi-anode photon detectors are mounted. In the TOP detector the two-dimensional information of the Cherenkov ring image is computed with the time of arrival and the impact position of Cherenkov photons at the photo-detector. The requested time resolution of 100 ps for a single-photon is achieved by using a custom

16-channel microchannel plate (MCP) photomultiplier tube (PMT). The TOP detector provides 85% K identification efficiency at a 10% π misidentification rate in the data at the early stage of the experiment, with 94.4% operational channels on average [36].

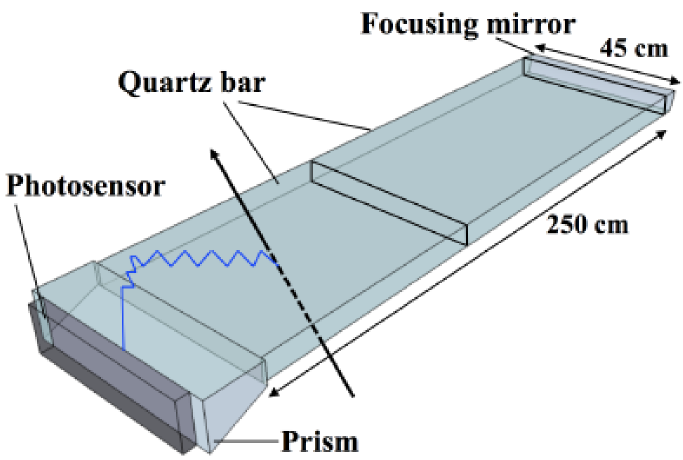

Figure 2.12: A module of the TOP detector.

The ARICH is used to identify charged particles and it requires a low momentum threshold for pions and good separation of pions and kaons of energy from 0.4 GeV/c up to about 4 GeV/c. Thanks to a new method, the number of detected Cherenkov photons is increased: two 2 cm-thick layers of aerogel with different refractive indices ($n_1 = 1.045$ upstream, $n_2 = 1.055$ downstream) are used to increase the yield without degrading the Cherenkov angle resolution (Fig. 2.13). A hybrid avalanche photon detector (HAPD) is used as a single-photon-sensitive high-granularity sensor, its dimensions are $73 \times 73\text{mm}^2$ and it has 144 channels. Here the photo-electrons are accelerated and detected in avalanche photodiodes (APD).

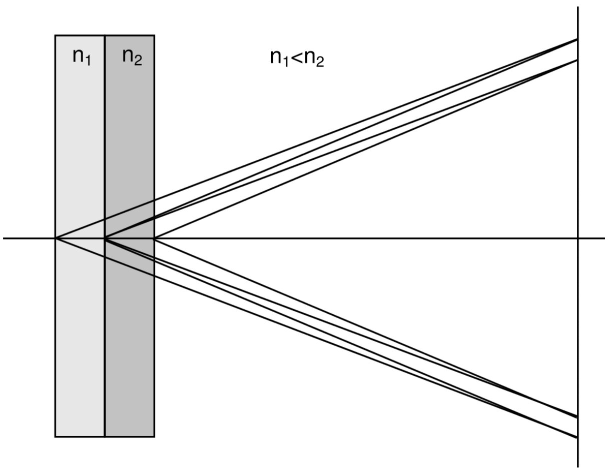

Figure 2.13: Representation of the ARICH operation.

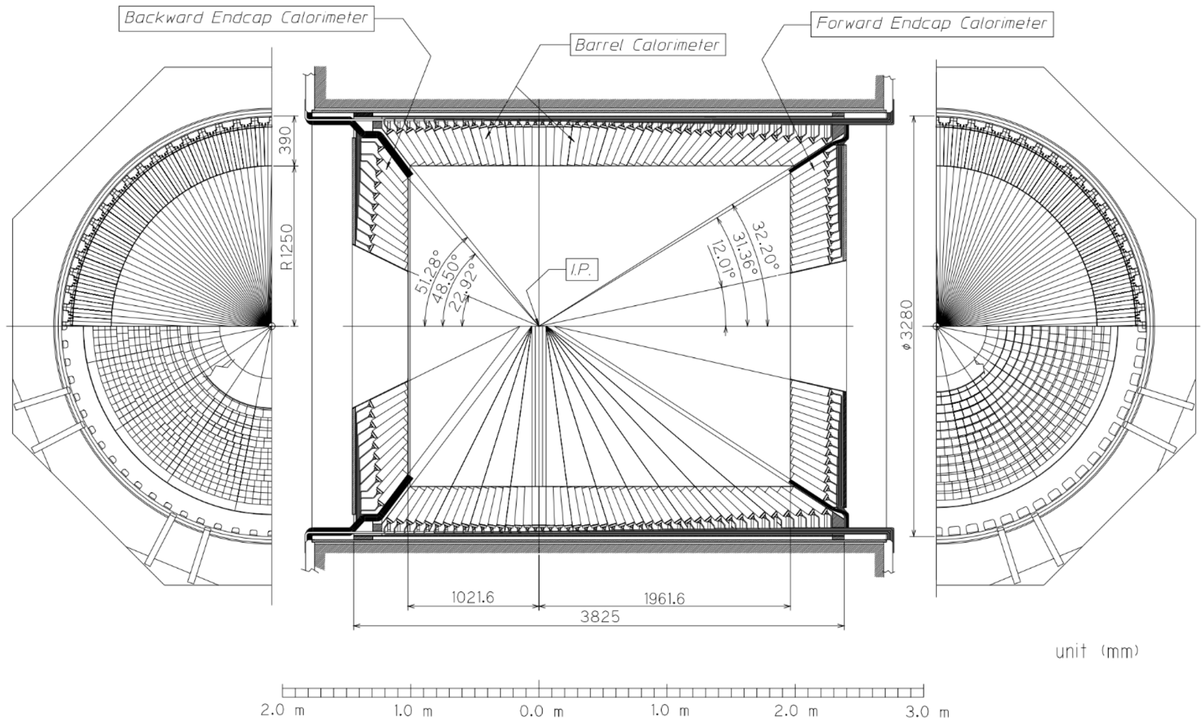

Figure 2.14: Structure of the electromagnetic calorimeter at Belle II [37].

2.2.6 Electromagnetic CaLorimeter

The electromagnetic calorimeter was designed to detect gamma rays and to identify electrons, i.e. separate electrons from hadrons, in particular pions. It is a highly segmented array of Caesium Iodide CsI(Tl) crystals doped with Thallium and assembled in a projective geometry shown in Fig. 2.14. The crystals have the form of truncated pyramids of an average size of about 6×6 cm^2 for the base and 30 cm ($16.2X_0$) high. With a total of 8736 crystals, it covers about 90% of the solid angle in the center-of-mass system.

2.2.7 K_L and Muon chamber (KLM)

The KLM [5], located outside of the superconductive solenoid, consists in 4.7 cm thick iron plates alternated with active detector elements. The iron plates serve as the magnetic flux return for the solenoid and provide 3.9 interaction lengths of material, in which K_L^0 mesons can shower hadronically. The Belle II KLM has layers of scintillator strips with wavelength shifting fibers to cope with the expected large background rates from neutrons. The read out is carried out by silicon photomultiplier (SiPMs, Geiger mode operated APDs), these are also damaged by the high neutron background and so increase the dark count rate in the light sensor; however irradiation tests have demonstrated that this detector system can be reliably operated by appropriately setting the discrimination threshold.

2.2.8 Trigger

When a bunch of electrons and one of positrons from the two beams collide with each other, the e^+e^- interaction generates a final state with a certain number and types of particles that travel through the detectors; this is called an *event*. The trigger system of

Belle II has the crucial role to identify events of interest during data-taking. Given the increasing physics scope at Belle II than previous generation B-factories, more dedicated triggers are required. The Belle II trigger system is composed of two levels: a hardware-based low-level trigger (L1) and a software-based high-level trigger (HLT).

Most of the dominant beam background's processes are characterized by the presence of less than two charged particle tracks in the CDC, accompanied by one or two clusters in the ECL. These topologies are similar to those of primary collision events to low-multiplicity production modes, and therefore they are challenging for such physics studies and the DAQ system.

The flagship measurements for Belle II in B and D flavor physics are expected to be highly robust to trigger implementation, where events will be easily identified from the presence of at least three tracks in the CDC trigger and a large deposition of energy in the ECL. The trigger for most B and D decays will be close to 100% efficient for events that are reconstructed by offline algorithms.

The nominal L1 trigger has a maximum trigger output rate of 30 kHz, limited by the read-in rate of the DAQ. To cope with the high event rate and background level at Belle II, a series of upgrades have been implemented at L1 with respect to Belle. The key areas of improvement involve the implementation of firmware-based reconstruction algorithms and trigger logic.

As a key component of the DAQ, the HLT must reduce online event rates from 30 kHz to 10 kHz for offline storage, and it must identify track regions of interest for PXD readout to reduce data flux. The HLT reconstructs the event with the same algorithms of offline reconstruction, allowing access to full-granularity event reconstruction using all detectors output signals except for the PXD. One of the information use in the HLT-trigger is the time of the EventT0 calculated with SVD-based computation, that is faster than the CDC-based computation, while maintaining a similar resolution (~ 1 ns).

2.3 Belle II software

The Belle II analysis software framework, called *basf2* [38, 39], is designed in independent blocks, called *modules*, that are executed linearly within a path performing smaller tasks. The modules communicate to each other by passing information to and from a common object store, called the *Data Store* (DS), which also keeps track of relations between objects in each event. In the DS, physics quantities extracted from raw data, like CDC hits, are saved together with more high level objects, such as tracks. For the analysis most of this information stored in the DS are reduced (by a factor of ~ 40) to particle-level information, such as four-momentum and event shape variables from the high-level objects.

The software takes care of the event reconstruction both in the online (HLT) and offline reconstruction. The reconstruction always starts from the raw data of the detector, however the offline reconstruction uses an optimized calibration and the HLT has not at its disposal the information coming from the PXD, since otherwise the execution time would be too high. Instead a region of interest (ROI) on the PXD is identified for each reconstructed track, and all the pixels inside these regions are saved in the raw data, to be used later on in the offline reconstruction.

The generation, simulation and reconstruction of Monte Carlo (MC) events are implemented as well in basf2, for example to calculate the performance of the software. The MC generates an event, starting from the final state of the collision e^+e^- till the stable daughter particles that reach the detector. The objects that it generates are called *MCParticles* and they contain the identity of the particle, the momentum and the position at which they are created. Such event goes through a simulation of the detector response and then the outputs are processed with the reconstruction in the same way as raw data, this way the detector effects are taken into account as well. During the simulation, also the true information are built using Geant4 starting from the MCParticle and the geometry of the detector, like the *SVD TrueHit*: space point of the true intersection of the MCParticle with the SVD layers. Generated quantities are matched with the relative reconstructed objects, for instance the MC particles with the SVD clusters that the particle leaves on the detector layers. Using this truth matched information it is possible to compute the expected performance of the reconstruction.

2.3.1 SVD reconstruction

The SVD output is the digitized electrical signal coming from a single strip, however the charge left by the crossing particle can be collected by adjacent strips assembled in a cluster. In the SVD, the electrical signal coming from a strip needs to have signal-over-noise ratio (SNR) above three to form a cluster and at least one strip in the cluster is required to have a SNR above five. A cluster holds information on the measurements of the released charge, the position and the time of the passage of the particle. Each side of an SVD layer can give only a one dimensional information on the passage of the particle, hence in a SVD layer the two sides, u and v, need to be combined to build a three dimensional space point (two dimension from the u and v cluster and one from the geometry of the crossed layer). It is possible, mostly due to beam background, that more than one particle crosses the same sensor in one event, so that the pairing of the u and v clusters is not obvious and a conspicuous number of wrong pairs, called *ghost hits*, are created. In Fig. 2.15 the cluster pairing is drawn when three particles cross the same sensor; a total of nine space points are created, however six of them are ghost hits. To reduce this effect, time selection criteria have been developed for high luminosity (and thus higher background): $|t_{u,v}| < 50ns$ and $|t_u - t_v| < 20ns$, where $t_{u(v)}$ is the time of $u(v)$ side cluster.

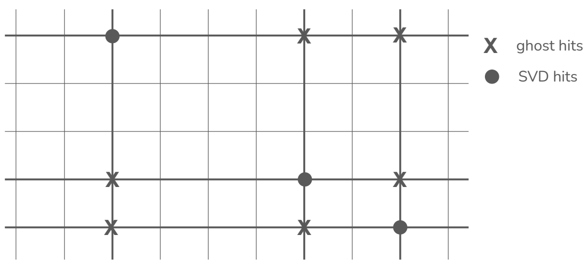

Figure 2.15: Representation of the u and v clusters pairing when three particles cross the same sensor. The strips market are those with a SVD cluster. The dots are the true hit of the particle in the SVD sensor, while the X are the wrong pairs, or *ghost hits*.

To evaluate the performance of the SVD reconstruction the *efficiency* and the *occupancy* are defined. In data, the efficiency of a sensor is defined as the fraction of intercepts of the reconstructed tracks with the sensor that have a reconstructed cluster in the vicinity. The occupancy of a sensor is the number of strips that have an electronic signal passing the threshold over the number of strips of the sensor in a event. In Fig. 2.16 the average efficiency and the occupancy for each side of the layers are reported for data acquired in June 2024. The efficiency is greater than 98.5% and the occupancy is less than 0.75% for all the sensors in this run. The third layer, being the nearest one to the beam axis, is the one with higher occupancy, and due to the lower SNR it has slightly lower efficiency than the others.

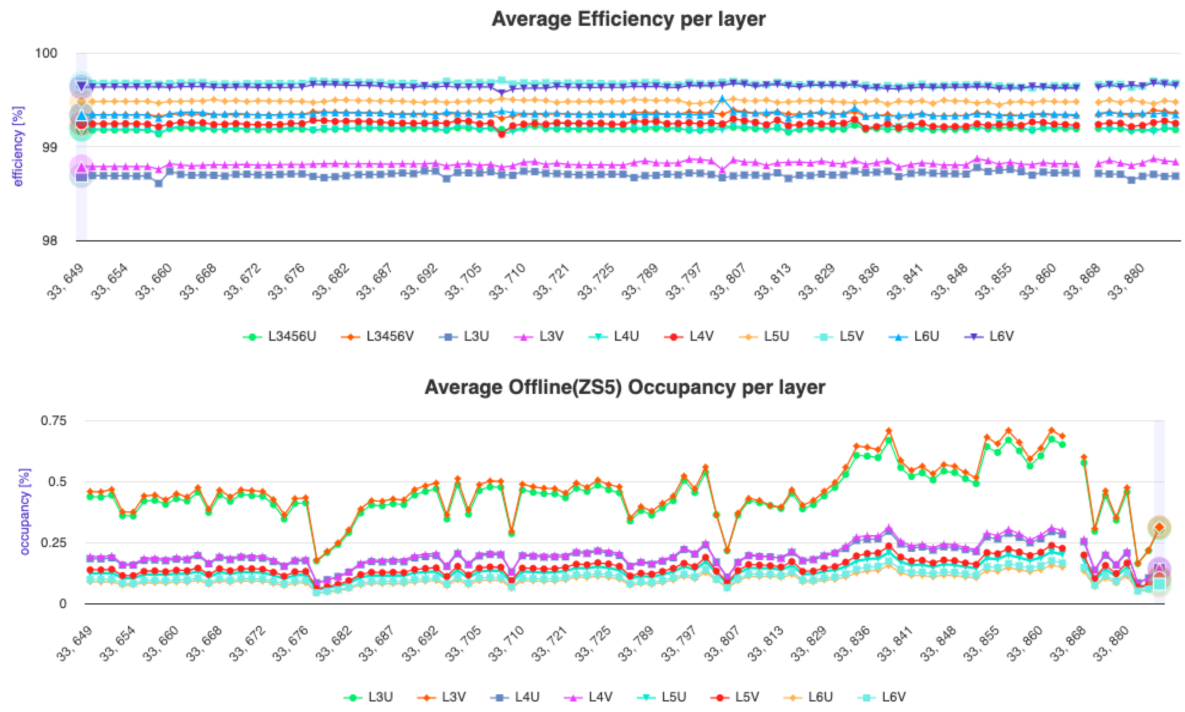

Figure 2.16: Average efficiency and occupancy of the SVD layers for data taken in June 2024.

The cluster position resolution is estimated from the residual of cluster position against unbiased track extrapolation using $e^- e^+ \to \mu^- \mu^+$ events. The resolutions are $7 - 12$µm for u strips and $15 - 25$µm for v strips, in agreement with expectations.

The SVD offers an excellent hit time measurement,measured from the residuals of the hit time with respect to the time of the $e^- e^+$ collision (also called EventT0) : 2.9(2.4)ns) for the $u(v)$ side.

Beam background and radiation effects in SVD

The beam-induced background has two effects on the SVD detector [24]: the radiation damage to the sensors and the increasing of the occupancy. Radiation damage can affect the sensor leakage current, strip noise, and the full depletion voltage of sensors; while the increase of the hit occupancy leads to a degradation of tracking performance. The limit for degradation of the tracking performance is 5% occupancy of the SVD innermost layer (L3), that is the layer more affected by beam background. During Run 1 the average hit occupancy on layer 3 sensors was less than 0.5% (now it is a little bit higher as shown in Fig. 2.16). Fig. 2.17 illustrates the expected occupancy at each SVD layer under the nominal extrapolation [35], that is still under the 5% occupancy limit. However, background simulations are affected by large uncertainties and a more conservative extrapolation yields a layer 3 occupancy as high as 8.7%, exceeding the limits of the occupancy for good tracking performance; this motivate the vertex detector upgrade during the LS2. Before that, the SVD will be able to withstand, with a good safety margin, the background levels.

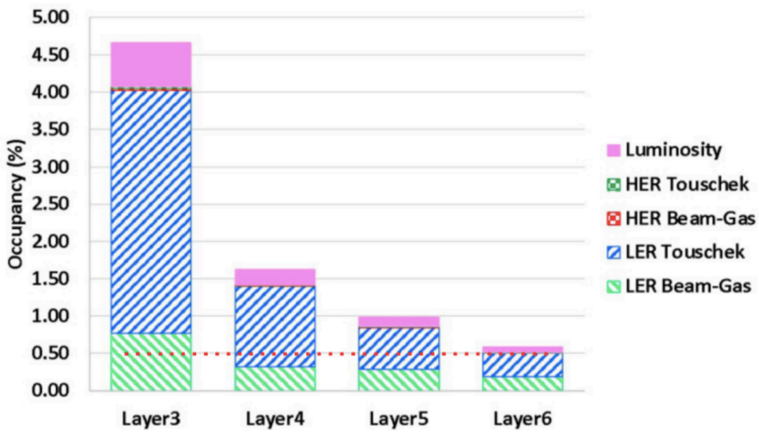

Figure 2.17: Prediction of hit occupancy for each SVD layer at nominal luminosity. The plot is taken from [35]

The SVD occupancy due to single beam backgrounds originates from two main sources: Touschek and beam-gas scattering.

Chapter 3

Tracking at Belle II

Tracking is one of the main steps of an *Event Reconstruction*: the process where the electric signal coming from the detectors is interpreted and transformed into particles used for physics analysis. In particular, tracking determines the charge and the trajectory of charged particles and the position of the displaced verteces ($V0$). The tracking software, implemented in the Belle II software framework (basf2), is applied both for online (HTL) and offline reconstruction. The detectors dedicated to such task are the VXD and the CDC described in chapter 2; given the different output signals of these detectors, custom tracking algorithms are implemented for the track finding. In this chapter, after an introduction on the trajectory of the charged particles in the magnetic field, the tracking algorithms implemented in the Belle II software are reported. At the end, the performance of the tracking software is shown and a study on the reconstruction efficiency and inefficiency of the K_S is discussed.

3.1 Charged particle in magnetic field

In collider experiments the particles created from the collision travel inside a magnetic field, therefore charged particles are subjected to the magnetic force

$$\overrightarrow{F_m} = q\overrightarrow{v} \wedge \overrightarrow{B} \tag{3.1}$$

and have a non linear trajectory unlike the neutral ones. In the ideal case in which the magnetic field $\overrightarrow{B}$ is constant and the particles travel in the vacuum, the magnetic force F_m acts as the centripetal force on the plane transverse to $\overrightarrow{B}$, resulting in the charged particle following a helical trajectory: an uniform circular motion on the transverse plane and a uniform linear motion on the same direction of $\overrightarrow{B}$.

The helix can be described by five parameters (see Fig. 3.1) defined at a specific point of the trajectory, in Belle II such point is chosen to be the perigee, or point of closest approach (POCA) to the origin, in the (r, φ) plane. The parameters are:

- d_0, the signed distance of the POCA from the origin in the transverse (x, y) plane. The sign depends on the direction of the angular momentum of the track at the POCA with respect to the magnetic field
- z_0, the z coordinate of the POCA
- φ_0, the angle between the transverse momentum at the POCA and the x axis

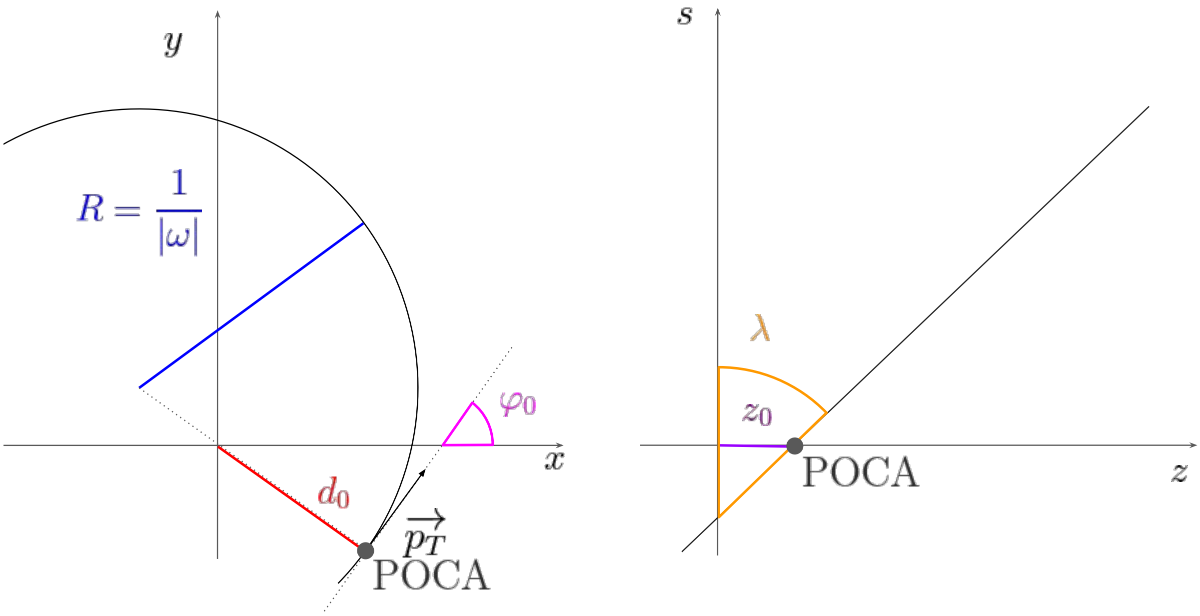

Figure 3.1: Visualisation of the five parameters the charged particles that define a helix. The variable s is the length of the helix traveled from the POCA to a chosen point on the helix.

- $\tan\lambda$: the tangent of the angle between the momentum at the POCA and the transverse plane
- ω, the curvature, where the sign corresponds to the charge assigned to the track.

Given these five parameters it is possible to calculate the position and the momentum of the particle in any point P of the trajectory using the following equations

$$\overrightarrow{X}(s) = \begin{pmatrix} \cos\varphi_0 & -\sin\varphi_0 & 0 \\ \sin\varphi_0 & \cos\varphi_0 & 0 \\ 0 & 0 & 1 \end{pmatrix} \begin{pmatrix} \frac{\sin s\omega}{\omega} \\ \frac{\cos s\omega - 1}{\omega} - d_0 \\ s\tan\lambda + z_0 \end{pmatrix} \tag{3.2}$$

$$\overrightarrow{P}(s) = \frac{qB_z}{\omega} \begin{pmatrix} \cos\varphi_0 & -\sin\varphi_0 & 0 \\ \sin\varphi_0 & \cos\varphi_0 & 0 \\ 0 & 0 & 1 \end{pmatrix} \begin{pmatrix} \cos s\omega \\ -\sin s\omega \\ \tan\lambda \end{pmatrix}, \tag{3.3}$$

where s is the length of the helix traveled from the POCA to the chosen point P, B_z is the magnetic field along the z coordinate (in Belle II the direction of $\overrightarrow{B}$ is the z axis, thus $B = B_z$) and q is the charge of the trajectory's particle.

The main task of a tracking algorithm is to find the helix trajectories of charged particles, exploiting their interaction with the active material. While the charged particles travel inside the magnetic field, they cross the detector and they interact with it leaving electronic signals. These signals are elaborated in three-dimensional (3D) space points, also called *hits*. By connecting correctly these hits, the track is found; to find a single helix at least three 3-dimensional space points are needed: the helix has 5 unknown parameters, while each space point provides two equations from the equation system in 3.2, not three because one of the equation is taken out by the lack of knowledge of the position s on the helix. Tab. 3.1 reports the numbers of degrees of freedom for the calculation of the helix parameters with one, two or three 3D space points. To resolve the problem uniquely, 2.5 space points are needed (each space point has a different s coordinate).

Table 3.1: Numbers of degrees of freedom in the calculation of the helix parameters when having one, two or three, 3D measurements. The number of unknowns increase because each space point has a different s coordinate.

n° space points	n° unknowns	n° equations	n° dof
1	5+1	2	3
2	5+2	2+2	1
3	5+3	2+2+2	-1

In real experiments the magnetic field is not uniform in the detector volume, for example at Belle II it varies up to 1% of the nominal value. Moreover the particles cross the detector material: the interaction with the detector can change the 4-momentum of the particle. Its direction is modified by multiple scattering and its energy decreased due to ionisation. Therefore the trajectory of a charged particle inside the detector volume is more similar to adjoin arcs of different helices separated by detector material. It is important to consider such effects during the track finding and the track fitting of the tracks.

3.2 Tracking in Belle II

The main task of the tracking software is the reconstruction of charged particles originating from the primary and secondary decay vertices. Most of the tracks originate from inside the beam pipe, except for the charged decay products of the long-lived $V0$-like particles (K_S^0 , Λ, and converted photons) that can be created also outside the beam pipe. The latter decay into two charged particles displaced from the interaction point. The tracking algorithms must identify the two oppositely charged decay products of $V0$ particles decaying inside the tracking volume and pair them.

The tracking algorithms [40, 38] are implemented in the Belle II analysis software framework (basf2) described in Section 2.3. Tracking reconstruction provides to the analyst the track fit result for charged particles and the decay vertex for $V0$ particles. The track fit result contains the position and momentum at the POCA. Since the same track can be fitted with two or more different mass hypotheses, two particles from two different lists could be related to the same reconstructed track with different track fit result. For the $V0$ the track fit results of the two daughter particles are stored, with the position and the momentum at the decay vertex position. The $V0$ algorithm is used to reconstruct K_S^0 , Λ, and photon conversion.

Charged particle reconstruction can be divided in two main parts:

- track finding: the detector hits belonging to a single track are identified in a sea of background hits, beam background or electronic noise of the detector, and collected together into a track candidate
- track fitting: the track five helix parameters are determined by fitting the track candidate.

Track finding consists in applying pattern recognition algorithms to determine track candidates. Since the features of the detector hits in the CDC and the VXD are different, dedicated track finding algorithms for each detector have been developed. The VXD track finder (VXDTF2) algorithm is based on the cellular automaton (CA) and Sector Maps , while two complementary algorithms are employed for CDC track finding: a global track finder based on the Legendre algorithm and a local track finder employing cellular automaton [5]. In addition combinatorial Kalmar Filters (CKF) are applied to tracks found by one detector to attached hits of the other detectors. The following sections will describe these algorithms in more detail.

The main track fitting algorithm used in Belle II reconstruction is the deterministic annealing filter (DAF), which takes in consideration the not perfect helix trajectory of the particles with different mass hypothesis. The DAF is based on the KF but is more robust against background hits and outliers since it can remove them.

Fig. 3.2 shows a simplified overview of the workflow of the tracking algorithm, some steps are missing but are explained in the next section.

3.2.1 Tracking workflow

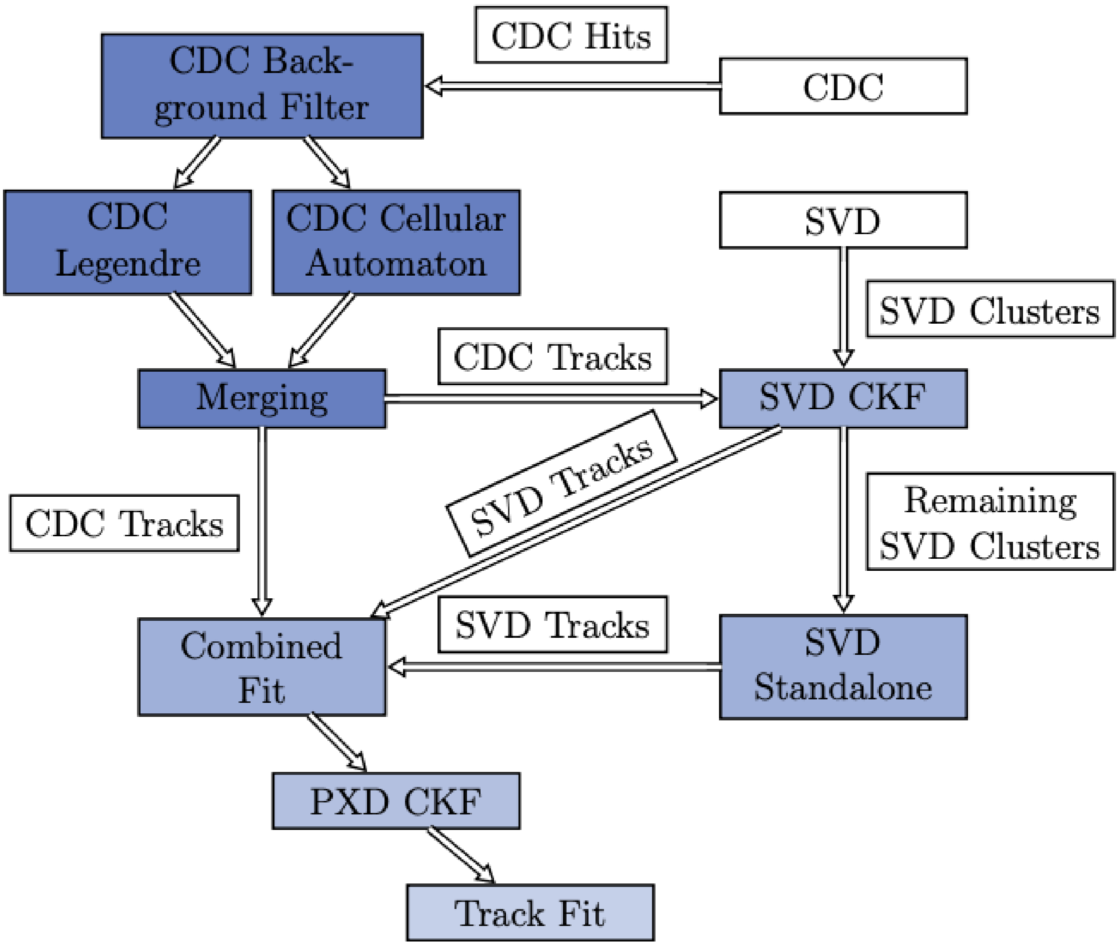

Figure 3.2: Workflow of the tracking algorithm. Some steps are missing, for example the CDC CKF.

At first, the hit signals in the CDC are filtered and reconstructed by the two independent algorithms, in particular the track candidates coming from the global track finder are taken as baseline. The results of both algorithms are merged and then these tracks are passed to a CKF that extrapolates them to the SVD and attaches SVD hits. The remaining SVD hits are used as input for the SVD standalone track finding. If there are CDC standalone tracks which don't have SVD hits attached to them from the first CKF, they are combined with SVD standalone tracks found in the previous step using another CKF. SVD tracks, that still don't have CDC hits, are extrapolated to CDC to attach CDC hits with a CKF (CDC CKF missing in Fig. 3.2), these are usually high-curvature tracks that did not produce enough hits in the CDC.

At this step the track finding stage is completed and the SVD and CDC tracks are merged and fitted. For the fit, a specific particle hypothesis must be assumed to calculate the energy loss and the material effects correctly. In Belle II, all reconstructed tracks are fitted with the π, K and p hypotheses.

For offline reconstruction a further step in track finding is needed at this point of the workflow, where the merged SVD+CDC tracks are extrapolated to PXD to attach PXD hits with a CKF.

After all the tracks are found, special classes of tracks are searched for, in particular tracks with displaced vertices to reconstruct K-short, Lambda and photon-conversions (see section 3.2.3).

It's possible that some tracks have the correct pattern but the charge assignment is wrong. This happens mostly for low momentum tracks in the transverse plane. A module, called Flip&Refit, was implemented in the offline reconstruction to reduce this issue.

The found tracks can be classified, using the MC truth, in:

- *found*, reconstructed tracks that are related to an MCParticle
- *clone*, reconstructed tracks that are related to an MCParticle but are actually just a piece of the trajectory who was not reconnected to the principal piece
- *fake*, tracks not related to an MCParticle.

3.2.2 Track fitting

The trajectories of tracks in Belle II are not ideal helices, as the charged particles interact with both passive and active detector material inside the tracking volume, losing a fraction of their energy and undergoing multiple scattering. In addition, the magnetic field provided by the superconducting solenoid is not constant in space. These effects are all taken into account in the tracking algorithms, in particular in the track fitting and track extrapolation stages. In order to correctly treat the interaction of particles with matter, a hypothesis on the mass of the particle must be made. Track fitting uses the GENFIT package [41], where both a standard Kalman filter and a robust extension, the deterministic annealing filter (DAF), are implemented. The Kalman filter is an iterative least square method to estimate the track parameters and their covariance matrix. The algorithm starts with some prior information on the parameters from the pattern recognition and it updates them when it adds the next predicted measurement. The DAF [42] is designed to be robust in the presence of outliers and background hits. In one iteration of the DAF, the Kalman filter runs twice over all measurements, once in the forward and once in the backward direction and removes hits that decrease the quality of the fit.

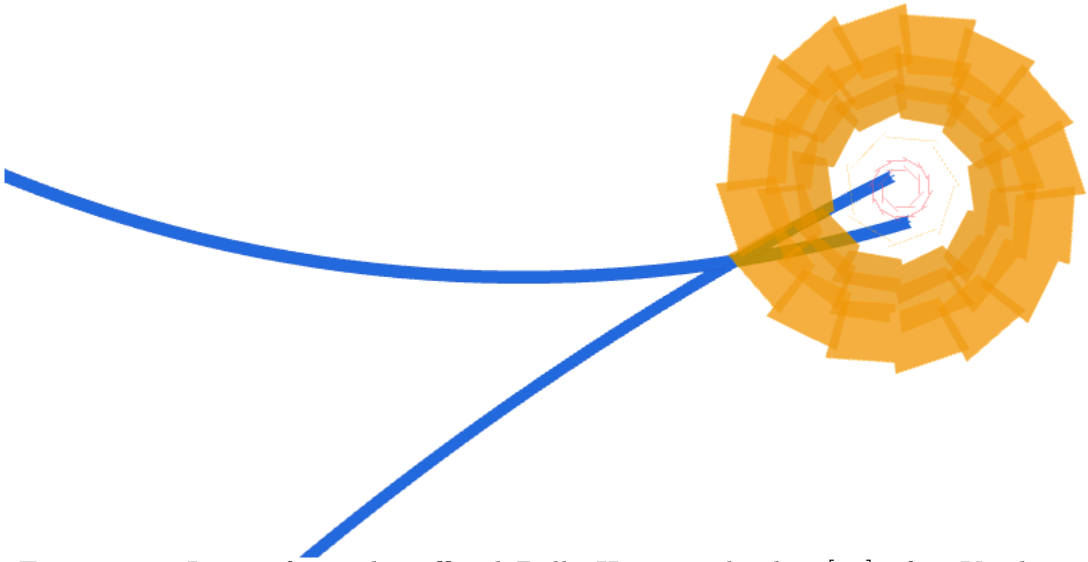

Figure 3.3: Image from the official Belle II event display [43] of a K_S decaying in two charged pions inside the VXD (ladders in orange). The two blue lines represent the reconstructed tracks of the daughters extrapolated towards IP.

3.2.3 V0 finder

The $V0$ particles, called by the V-shape, as shown in Fig. 3.3, of the two daughters' tracks, are reconstructed using a dedicated algorithm. The $V0$ particle lists include K_S, Λ and converted photons. These neutral particle are generated in the proximity of the interaction point (IP), however they are long-lived particles and decay into two charged particles displaced from the interaction point.

The reconstruction of the $V0$ that decay outside the beam pipe takes place after the reconstruction of single charged particles and not at the analysis level where the material information for the extrapolation of the tracks is not available. The goal of $V0$ reconstruction is to keep good $V0$ candidates originating from outside the beam pipe whose reconstructed mass is close to the mass of the mother particle. $V0$s originating from inside the beam pipe are not saved by the $V0$ finder since no extrapolation is needed to correctly save the information of the daughter particles and the $V0$ can be reconstructed at analysis level using the standard reconstruction procedure. The $V0$ reconstruction algorithm pairs all oppositely charged tracks and a range of the invariant mass is computed for all the combination, if the range don't overlap with any mass window the pair is rejected. Each accepted combination is processed by the vertex reconstruction package RAVE. If the vertex fit succeeds and the combination satisfies the selection criteria on the χ^2 and the mass window around the nominal $V0$ mass, it is marked as a $V0$ particle.

3.3 CDC standalone pattern recognition

The CDC hits are represented by drift circles around the wire that collected the charge coming from the interaction between the charged particle with the gas of the chamber; the radius of the circles is calculated using a calibrated x-t relation with the drift time (the difference between the moment the drift electrons arrive on the wire and the trigger). The particle trajectory is tangent to each drift circle. Both the local and the global pattern recognition use these hits as inputs, starting from the axial hits and then adding the stereo hits.

3.3.1 The (global) Legendre Track Finder

The global track finder of the CDC is highly efficient for tracks coming from the IP, even when there are missing hits. It exploits the Legendre transformation to search for patterns of hits consistent with a helix, it's called global since it exploits all the hits not already assigned to a track, simultaneously.

The first step of this algorithm is to apply to the hits coming from axial wires a conformal mapping, with the center at the origin (IP)[1]:

$$u = \frac{x}{x^2 + y^2}, \quad v = \frac{y}{x^2 + y^2}, \tag{3.4}$$

the drift circles are on the transverse plane (x, y) where the trajectories of the charged particles are circular. The conformal mapping converts the trajectories coming from the IP to straight lines, while the drift circles remain circles, as shown in Fig. 3.4.

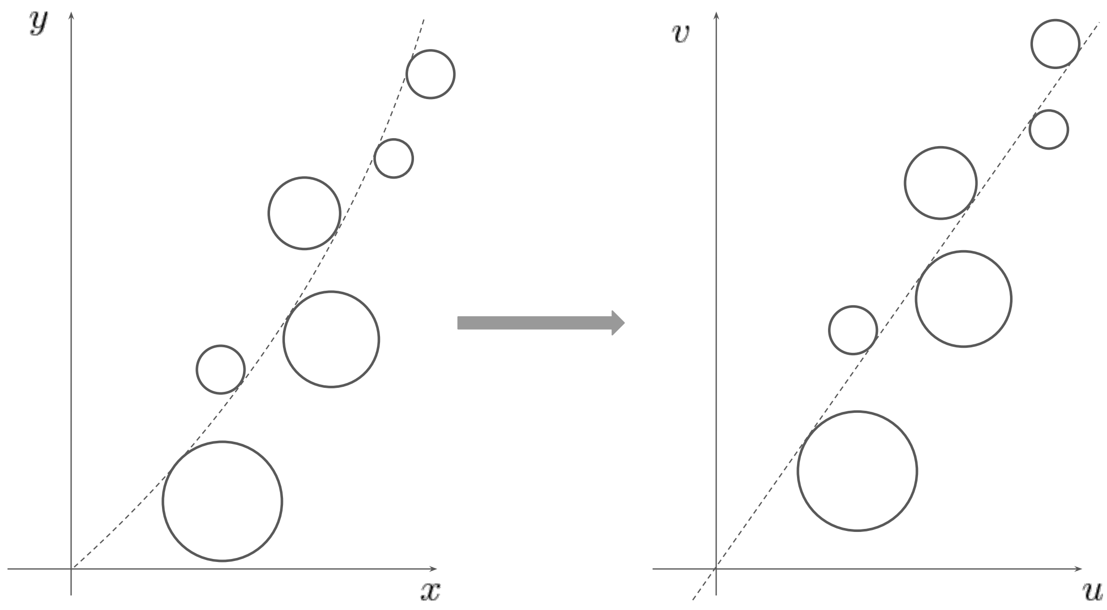

Figure 3.4: Conformal mapping that converts circles passing by the origin in straight lines (dotted line) while other circles remain unchanged.

The equation of a line tangent (the trajectory) to a circle (the drift circle) can be express by the two Legendre parameters ρ and θ as

$$\rho = x_0 \cos\theta + y_0 \sin\theta \pm r \tag{3.5}$$

where x_0, y_0 and r are the coordinates of the centre and the radius of the drift circle. Each drift circle maps to a sinusoidal function in the (ρ, θ) space. This double mapping is called Legendre transformation [44] and is commonly used for pattern recognition problems in drift tubes detector. At this point a two-dimensional binary search algorithm takes place

[1]These u and v are not the local coordinates of the SVD hits even if the notation is the same.

to find the most populated regions in the (ρ, θ) space: it represents a trajectory tangent to the most drift circles. The (ρ, θ) space is divided into four equally sized bins and the most populated of them is selected for further subdivision, until the bin size becomes smaller than a resolution parameter that is taken to be dependent on ρ and that take into account the smearing of the track parameters caused by energy loss, non-uniformity of the magnetic field, displaced IP, uncertainty of the drift circle radii and wire displacements. A representation of the algorithm is shown in Fig. 3.5 with an example.

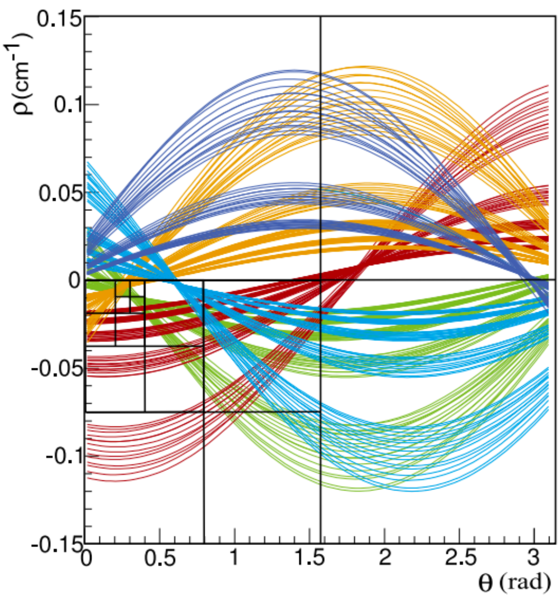

Figure 3.5: An example of the standard two-dimensional binary search algorithm. Plot taken from [40].

If the found track candidate satisfies certain quality criteria, it is stored and the process is repeated iteratively removing the CDC hits (or drift circles) attached to the track candidates already found. Before adding the information from the stereo wires, the track candidates are fitted and merged when possible to remove clone tracks, that are usually created by low momentum particles that loops several times inside the detector volume. Additionally, some hits can be removed, reassigned, or added based on the new insights provided by the fit results.

The information on the z coordinate is added at the next step, using the hits on the stereo wires. Each (r, φ) trajectory found in the previous step is exploited to reconstruct the position information of each stereo measurement. The drift circle on the stereo wire can be enclosed or not to the trajectory circle, hence two solutions (z_{rec}) for the reconstruction of the z coordinate are found (they are discarded if they are far outside the volume of the detector). The problem is similar to the one on the (r, φ) plane, but this time the trajectory are searched for on the plane (z, s) where they are straight line, described by the equation

$$z_0 = z_{rec} - \tan \lambda s_{rec}. \tag{3.6}$$

If some hits are compatible with more than one $(r\varphi)$ track, they are discarded to increase purity.

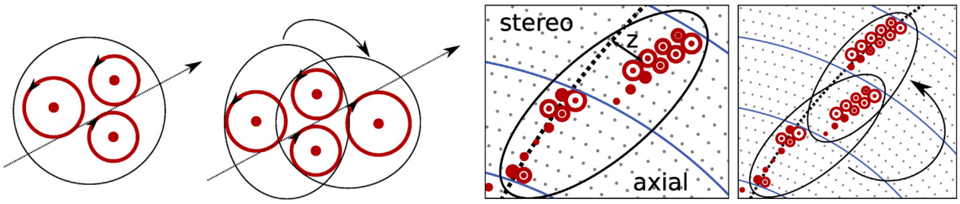

Figure 3.6: A representation of vertices and edges in the two step of the CDC local track finder: On the left the construction of superlayers segments, on the right the one of the track candidates.

3.3.2 The (local) Automaton Track Finder

The local track finder of the CDC searches for segments and tracks using a cellular automaton and the neighbourhood relations between hits. The track finder is robust against energy losses and tracks that do not originate from the IP. [5]

The local algorithm is complementary to the global one by detecting tracks displaced from the IP (such as the charged daughters of $V0$ particles like the K_S) and short tracks, as it does not make an assumption on the origin of the tracks. It searches for connected hits in the superlayers and then it combines them in longer tracks using weighted cellar automation method [45], as sketched in Fig. 3.6. In the first step, sets of three hits are combined and a linear trajectory tangent to the drift circles is fitted, the results from the fit are used to assign the weight of the triplet (*vertex*). If two triplets have two drift circles in common (passing some loose selection) a similar fit and weight assignment is done for the quadruplet (*edge*). Segments in the superlayers are built by maximising the weights of the triplets and the quadruplets.

The second step that connects axial segment to stereo one into track candidates exploits the same method with the combination of a pair of axial- and stereo-wire segments as vertices and as edges the combination of two vertices.

In the current implementation of the tracking algorithm the CDC local algorithm is not fully applied, in particular it does not provide completed tracks but only segments. Otherwise the fake rate would have been too high ($> 10\%$).

In the merging of the tracks coming from the two finding algorithms of the CDC, the segments found by the local finder are added to the global tracks using a multivariate method trained with simulation.

3.4 VXDTF2

This algorithm is commonly referred to as SVD-standalone algorithm since it uses only SVD hits, mainly for tracks that are not reconstructed by the CDC due to the few hits (low momentum particles with a transverse momentum of less than 100 MeV/c). It has three steps: the creation of candidate tracks using the Sector Map, a first evaluation of the former with a CA and a second selection to choose the best track. The tracking algorithm of the VXD uses as input already manipulated data by the SVD reconstruction, explained in 2.3.1,the SVD clusters. The three steps are described in the next two sub-sections.

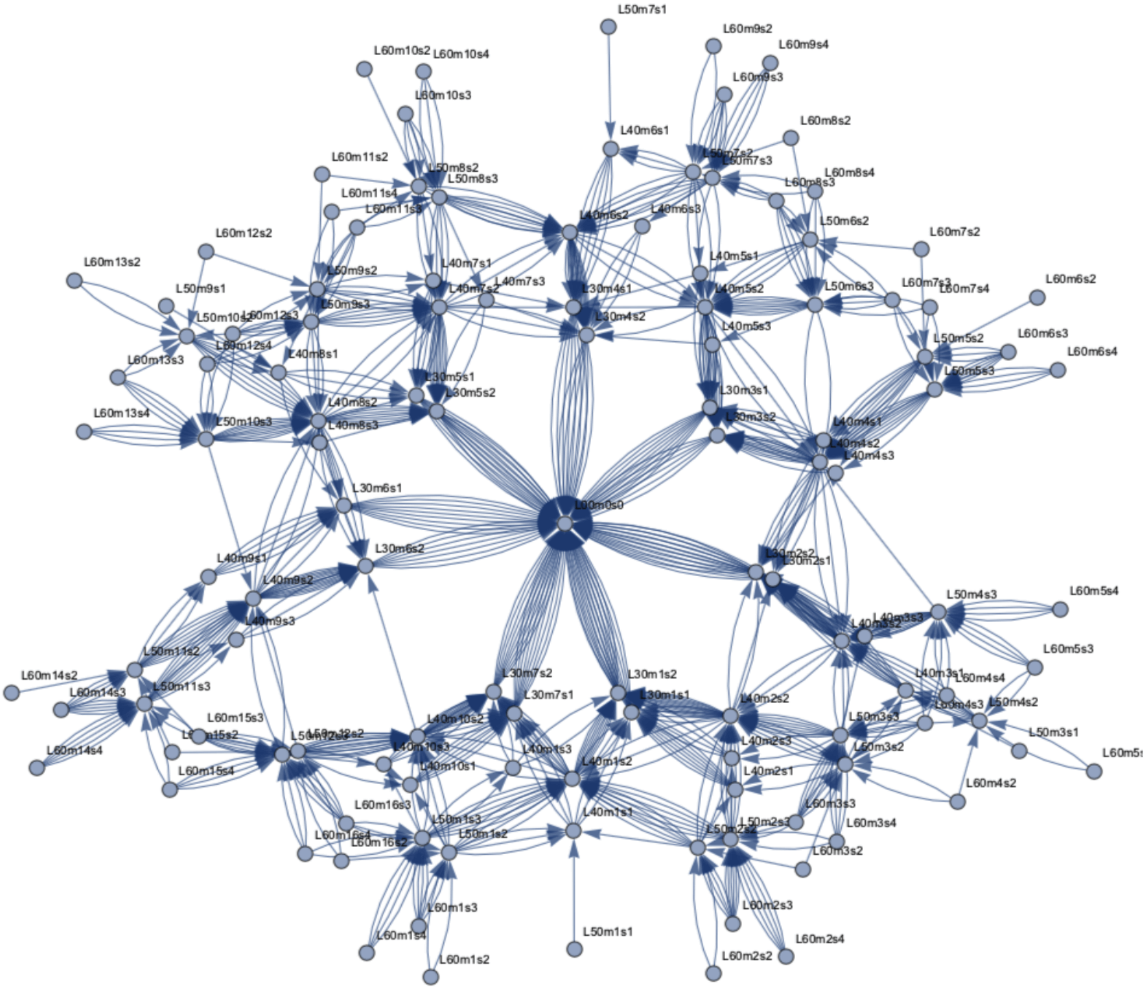

Figure 3.7: Simplify scheme of a sector map.

3.4.1 Track candidate with sector maps

A sector map is a data structure containing the possible relations between different regions of the detector connected by a track, a simplified SVD Sector Maps is reported in Fig. 3.7. These regions called *sectors* are obtained by dividing a sensor in four sections: two parts along its width and two parts along its length. It also holds some selection criteria, called *filters*, to remove pairs and triplets space point on connected sectors to reject background. The sector map is created with a simulated training sample. It can be trained with different samples, such as high and low momentum or $\Upsilon(4S)$ or Bhabha events. During this training process, the Sector Map learn the geometry of the SVD and its defects, as long as they are correctly modeled in the simulation.

In the first step of the SVD track finding algorithm, a *sector network* is created from the sector map: it holds the relations between all the active sectors (i.e. containing clusters). Then a second graph is built connecting space points of related sectors that pass the selection criteria of the Sector Map; a pair of space points is called *segment* hence the graph is called *segment network*. A path in the segment network that contains three or more space points is considered a track candidate. In the creation of these networks a limitation on the number of nodes and edges is requested to handle some problematic Bhabha events where the electron creates a shower in the SVD generating many clusters in small region of the detector; in such cases the combinatorial time would exceed the limit for the HLT. For the same reason, a selection with a quality indicator, the same of this algorithm's final step , is employed for paths that have one segment (a pair of space points) in common: it is not a selection with threshold, instead a fixed number of paths pass the selection.

3.4.2 Cellular automaton and best path

In the second step a cellular automaton algorithm selects the longest paths, as shown in Fig.3.8, starting from the outermost layers that have less hits by background particles.

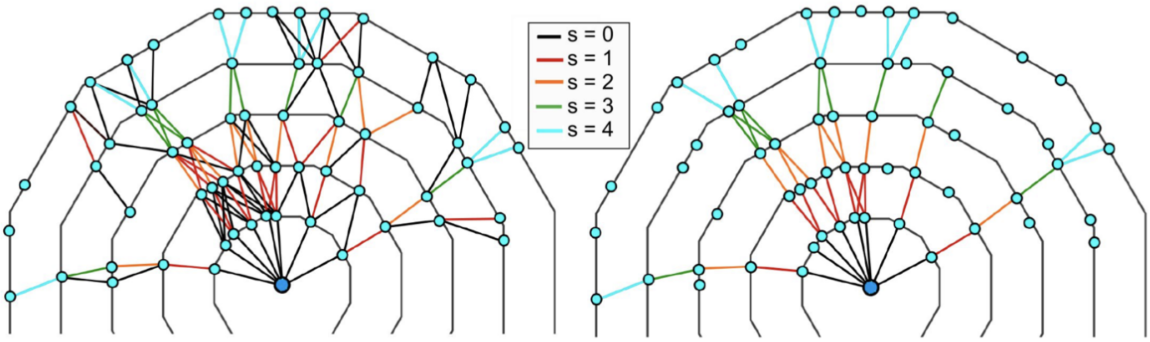

Figure 3.8: Selection of the logest paths with cellular automaton in the VXD.

The final step consists of selecting the best path when two or more paths share a cluster: a rating involving a fast fit that considers multiple scattering is applied to each one of these paths and all the possible sub-paths that have at least three space points. The track with the highest p-value of the fit is chosen to be the best one.

3.5 Track extrapolation and CKF

When talking about extrapolation, two different cases need to be considered, depending on which object is extrapolated:

- a complete track with hits measurement and track fit result
- a seed track with only the initial state: the momentum and the position of the particle in a specific point (or the track parameters).

In the first case the fitted track, composed of all the arc helices caused by the interaction of the detector, is available and the extrapolation consists of moving along the track till a specific point or plane. The value of the momentum and position of the particle in that specific point or the track parameters of the arc helix to which the point belongs to are then available. In Belle II, this case is used for instance in the $V0$ finder, to save the parameters of the $V0$ daughter tracks at the $V0$ decay vertex, and in the CKF.

In the second case only the helix built from the seed is available. Usually the seed is an approximate estimate that will be updated when measurements are added to the track. The extrapolation in this case also consists of moving along the trajectory, but this time along a single helix. When it crosses the detector material, it defines *intercepts*, for example with VXD layers, that are used to search for measurements to add to the track. The extrapolation takes into account the interaction with the material considering multiple scattering and energy loss effects. This is also used in the Combinatorial Kalmar Filter, when it attaches to the track coming from a detector, hits from another detector.

3.5.1 CKF

The CKF is an iterative local algorithm that uses extrapolation: it considers multiple hypotheses at a time if more than one hit could be attached to the extrapolated track, and it updates only those that pass certain criteria. Similar CKFs are used in the tracking algorithm depending on the input. The general idea is to start from a seed for the parameters of a track and to extrapolate it forward or backward to attach new measurements. For example, starting from a CDC track candidate produced by the CDC pattern recognition and the DAF, the seed, for the tracks to extrapolate toward the SVD layers, is the momentum and position of the CDC track extrapolation to edge between the CDC and the SVD.

Now the track can be extrapolated towards the SVD layers. Each time it reaches a layer multiple candidate hits are found and selected using a FastBDT. If more than one hit passes such selection the track is duplicated and both hits are attached to the tracks, one for each track. The process is iterated till the last SVD layer, at this point multiple options have been generated for one CDC track candidate but the FastBDT will select the best one together with a DAF that also evaluates material effects. As described in section 3.2.1 the CKF is used four times and not only from CDC to SVD: once going from CDC track to SVD clusters, once from SVD tracks to CDC hits, once from CDC plus SVD tracks to PXD clusters and once for the merger og CDC and SVD tracks.

3.6 Performance

To evaluate the performance of the tracking algorithm five figures of merit are taken into account; as anticipated in section 2.3, they are defined comparing the output of the reconstruction of simulated data with the truth coming from the simulation of the MCParticle interaction with the detector. In the next definition the following notation is used:

- MC track, a track of TrueHits
- PR track, a track coming from the reconstruction of the simulated events.

The *hit efficiency* is defined as the fraction of hits of an MC track contained in the relative PR track, and indicates how well the pattern recognition identifies all the hits belonging to a single track.

The *hit purity* is defined as the fraction of hits of a given PR-track contained in an MC-track, and quantifies how precise the pattern recognition is in identifying the hits belonging to only one particle.

A PR-track is defined as *matched* to a given MC track if the hit purity and efficiency exceed respectively 66% and 5%. The low hit efficiency requirement accounts for low transverse momentum tracks curling in the tracking volume (especially if p_z is small as well) which may leave several hundreds of true hits, that the algorithm is not interested in recovering all, it just needs the first arm inside the detector. If two or more PR-tracks are matched to the same MC-track, the one with the highest hit purity is defined as the correctly identified match and the remaining ones are defined as *clones*. If multiple PR-tracks have the same hit purity, the hit efficiency is considered in addition to the purity to identify the match.

The *track finding efficiency* is defined as the fraction of MC-tracks that are matched. If the PR-track fails the purity requirement, e.g. the PR-track is made up of hits from two MC-tracks, each one with a hit purity below 66% or the PR-track is made of background hits, it is defined as a *fake*.

The *fake rate* is defined as the fraction of PR track candidates which are labeled as fake.

The *clone rate* is defined as the ratio between the number of clone tracks and the number of found plus clone track.

In Fig.3.9 on the left, the tracking efficiency of the CDC is reported as a function of the transverse momentum. This distribution can be compared to the one for the SVD on the right (Fig.3.9), as expect the SVD is more efficient for particles with lower momentum.

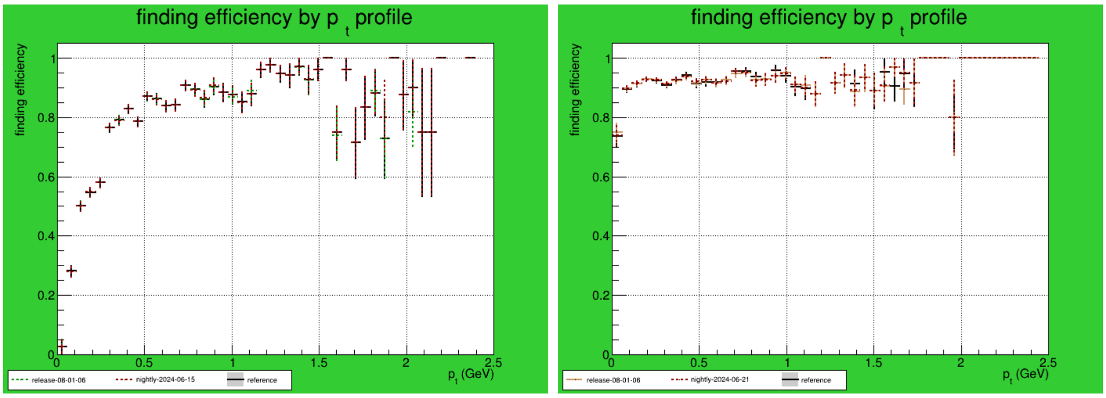

Figure 3.9: Efficiencies of the track finding algorithm of the CDC (on the left) and the SVD (on the right) in $B\overline{B}$ events with nominal background.

The previous performance is evaluated on an independent set of simulated $\Upsilon(4S)$ events, including beam-induced background simulated for the design instantaneous luminosity. The tracking efficiency for most of the charged particles expected at a typical Belle II collision is higher than 93% with double of the expected beam background, see Fig. 3.10 on the left, for the tracking efficiency for different primary particles. This is an integrated number, for example is lower for low momentum particles, as shown in Fig. 3.10 on the right.

3.7 Current K_S reconstruction performance at Belle II in $B\overline{B}$ events

Usually the K_S is reconstructed in the decay $K_S \to \pi^+\pi^-$: the tracks of two opposite charged pions are found and a vertex fit is performed to find the decay vertex of the K_S , using the algorithm described in section 3.2.3.

I have evaluated the tracking efficiency of the K_S in $B\overline{B}$ events, plotted in black in Fig. 3.11, as a function of the transverse distance of the decay vertex. It is about 84.9% near the interaction point (IP) and it decreases when the decay vertex distance increases until after the fourth SVD layer (at 10.4 cm), when it becomes almost constant, around 57%. This can be explained, since for an SVD track at least three hits are needed to

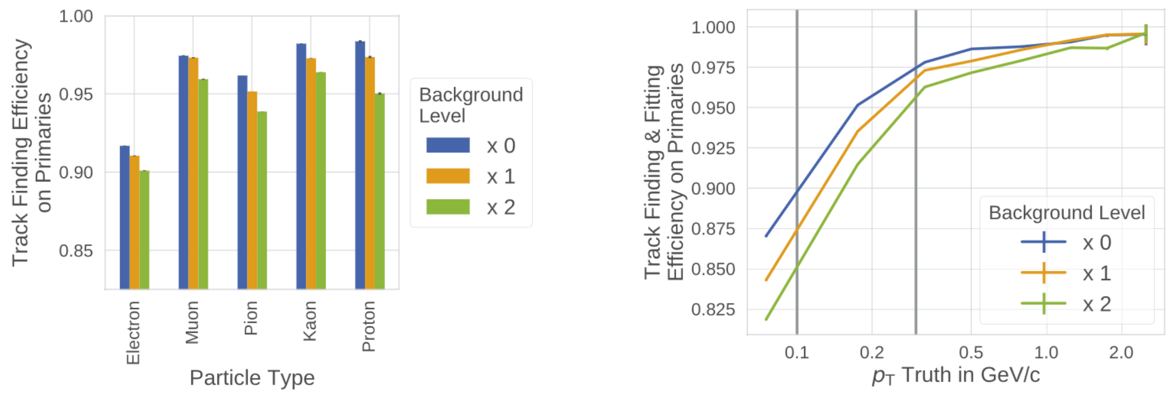

Figure 3.10: On the left, the tracking efficiency for the most important primary particles in a B decay with different scenarios of beam background. On the right, the finding efficiencies as a function of the transverse momentum with three background hypotheses are plotted. Plots taken from [40].

perform a fit, therefore for the daughters coming from a K_S that decays after the fourth layer of the SVD, the reconstruction of the tracks relies only on CDC detector for the most displaced particles.

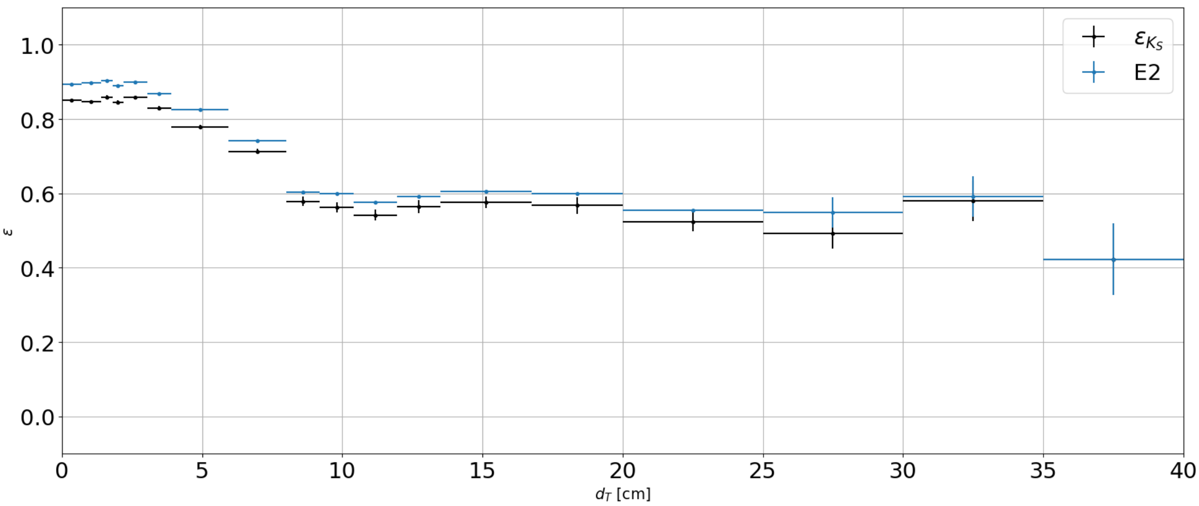

Figure 3.11: In black the efficiency (ϵ_{K_S}) of the K_S reconstruction in $B\overline{B}$ events as a function of d_T, the transverse distance of the K_S decay vertex. In light blue the probability of reconstruct both daughter of the K_S with the correct charge (E2) in $B\overline{B}$ events.

3.7.1 Inefficiency

The reconstruction of the K_S can fail for two reasons: the vertex fit does not converge or one of the daughters is not correctly reconstructed or found.

In Fig. 3.11 the probability of finding both of the daughters' tracks with the correct charge is compared with the K_S efficiency; the small differences between the two histograms are due to the failure of the vertex fit: the integrated efficiency of 80.8% with the vertex fit versus the 83.02% without the vertex fit.

Excluding the failing of the vertex fit, two other types of mistakes can be made in the K_S reconstruction, and they both concern the reconstruction of one or both of the daughters: the track of the pion is not found at all (it's missing) or the track is found but the wrong charge is assigned to it (the latter can happen especially when the particle has high momentum or when it loops inside the CDC, $\tan\lambda \sim 0$ and $p_T < 250\,\mathrm{GeV}$). The combination of these two types of failures generate five types of inefficiencies in the K_S reconstruction labelled as in the following list (in parentheses the probability to fall in that category):

- E2W2: two reconstructed daughters both with the wrong charge ($0.014 \pm 0.004\%$)
- E2W1: two reconstructed daughters, one with the wrong charge and one with the correct one ($3.28 \pm 0.06\%$)
- E1: one reconstructed daughter with the correct charge and one missing daughter ($14.72 \pm 0.13\%$)
- E1W1: one reconstructed daughter with the wrong charge and one missing daughter ($0.21 \pm 0.02\%$)
- E0: both daughters missing ($0.73 \pm 0.03\%$).

In Fig. 3.12 these inefficiencies are plotted (for $B\overline{B}$ events) as a function of the transverse distance of the K_S decay vertex, with also the sixth case where both daughter are reconstructed with the correct charge (that, as said before, is basically the same as the K_S tracking efficiency).

The algorithm described in the next chapter (Chapter 4) aims to recover the K_S decaying inside the SVD that have one reconstructed daughter with the correct charge and one missing daughter; in fact this is the biggest source of inefficiency but also the easiest case to study. It's important to keep in mind that to perform a fit and find the five helix parameters, three space points usually are needed. However for the case under study, just two space points should be sufficient, since the decay vertex of the K_S can act as the third point. This requires to fit the two tracks together skipping the single fit where each track is fitted by itself). This is why the algorithm can recover only K_S decaying inside the fifth SVD layer.

Implementation of `isTrackFound` variable To produce the plots in Fig. 3.11 , 3.12 and 3.13, I implemented a new analysis variable in basf2 that indicates if an MC particle (a true particle generated by the MC) was reconstructed by the tracking software. This variable, called `isTrackFound`, can have four values: 0 if the track is not found, 1 if the track is found with same charge of the MC particle, -1 if the track is found with assigned charge opposite to that of the MC particle, and NaN for other cases, like a neutral particle. This variable in used to identify the inefficiency of K_S reconstruction, as it was explained before in this section. There is a discrepancy between the overall efficiency to find both of the daughters with the correct charge when I compare it with the K_S tracking efficiency (83.02 %) versus the fraction complementary to the sum of the fractions listed in the bullet list above (81.05 %). This is caused by a correction, needed for `isTrackFound` variable to be able to compare it correctly with the K_S efficiency, that was calculated using the analysis variable `isSignal`. The variable `isSignal` is a complicated variable for reconstructed tracks that indicates if the track is related to an MCParticle, meaning it

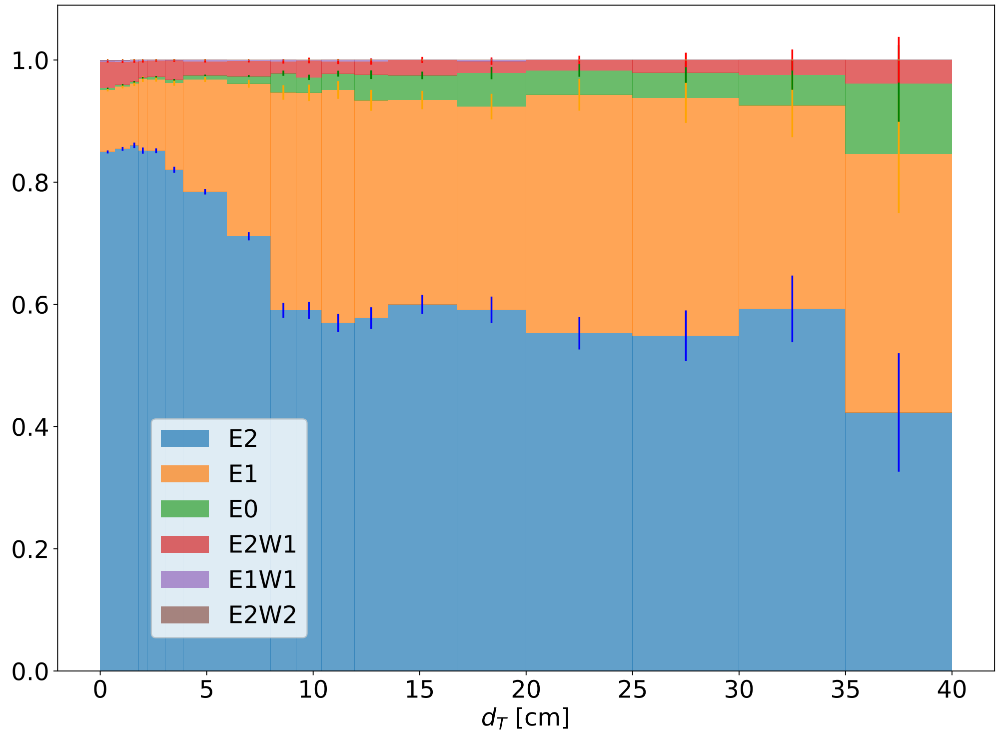

Figure 3.12: Probability of the different types of failures of the K_S reconstruction, classified by the (un)correct reconstruction of one or both daughters, in light blue the probability of reconstructing both daughters with the correct charge is plotted as well. The smaller percentages are not seen, but are still plotted.

comes from a true signal particle or not. Ideally these two variables should be symmetric, however an asymmetry can be spotted when looking to just one of the daughters and a correction can be computed. This correction is minimal and it was only applied in the plot 3.11, since it is not relevant for the plots in Fig. 3.12 and 3.13 and the next steps, leading to the highlighted discrepancy.

In the following section I will discuss the E1 case, where only one of K_S daughter is reconstructed.

3.7.2 E1 case

The E1 case (the K_S which has one reconstructed and one missing daughters) is the one that I want to focus on for the development of the new algorithm. In Fig. 3.13 its probability as function of the transverse distance of the decay vertex (d_T) is plotted. The maximum gain in efficiency ($14.72 \pm 1.3\%$) is distributed in intervals of d_T as follows:

1. $d_T \in [0, 2.2]$ cm (inside PXD) $E1 = 5.82 \pm 0.08\%$
2. $d_T \in [2.2, 4.9]$ cm (outside PXD, inside L3 SVD) $f_{E1} = 2.24 \pm 0.05\%$
3. $d_T \in [4.9, 8.0]$ cm (between 3th and 4th layer of SVD) $f_{E1} = 3.52 \pm 0.07\%$
4. $d_T \in [8.0, 10.4]$ cm (between 4th and 5th layer of SVD) $f_{E1} = 1.30 \pm 0.04\%$

5. $d_T \in [10.4, 13.5]$ cm (between 5th and 6th layer of SVD) $f_{E1} = 0.89 \pm 0.03\%$

6. $d_T > 13.5$ cm (outside SVD, inside CDC) $f_{E1} = 0.94 \pm 0.03\%$.

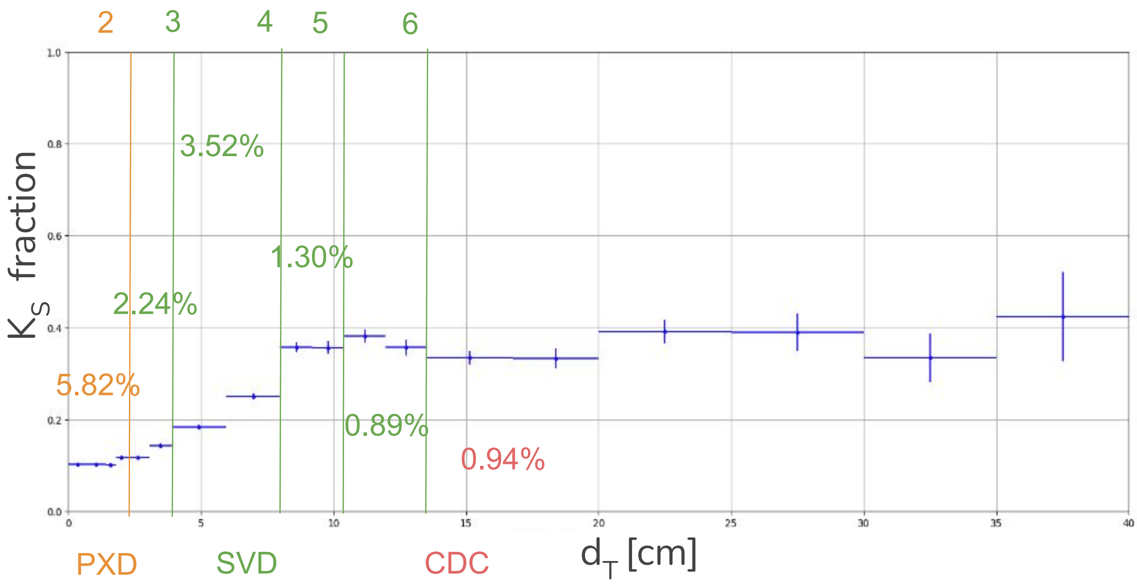

Figure 3.13: Probability of finding only one reconstructed daughter of the K_S with the correct charge as a function of the transverse distance of the K_S decay vertex. The vertical lines correspond to the position of the VXD layers (in the barrel region), as exception of the first layer, and the percentages represent the fraction of E1 in each interval.

Since I aim to recover only those K_S decaying inside the fifth SVD layer, the maximum gain I can obtain is 12.88% (sum in the first four intervals). Fig. 3.14 shows the same probability of the plot in Fig. 3.13 in the (d_T, z) plane: it is higher at the edge, in the forward and backward region of the detector. That is indeed a more complicated region for tracking being on the edge of the acceptance.

In the next chapter, a dedicated dataset is used to study the development of the new algorithm to have higher statistics in the regions of the detector where K_S efficiency is lower; at the same time it's important to remember that in physics events the majority of gain in term of statistics is near the beam line, not just $B\overline{B}$ as shown in Fig. 3.13, but in $c\bar{c}$ too, and that at least two hits are needed and an estimation of the vertex position to fit the track, that's why I can only consider the K_S decaying inside the fifth SVD layer.

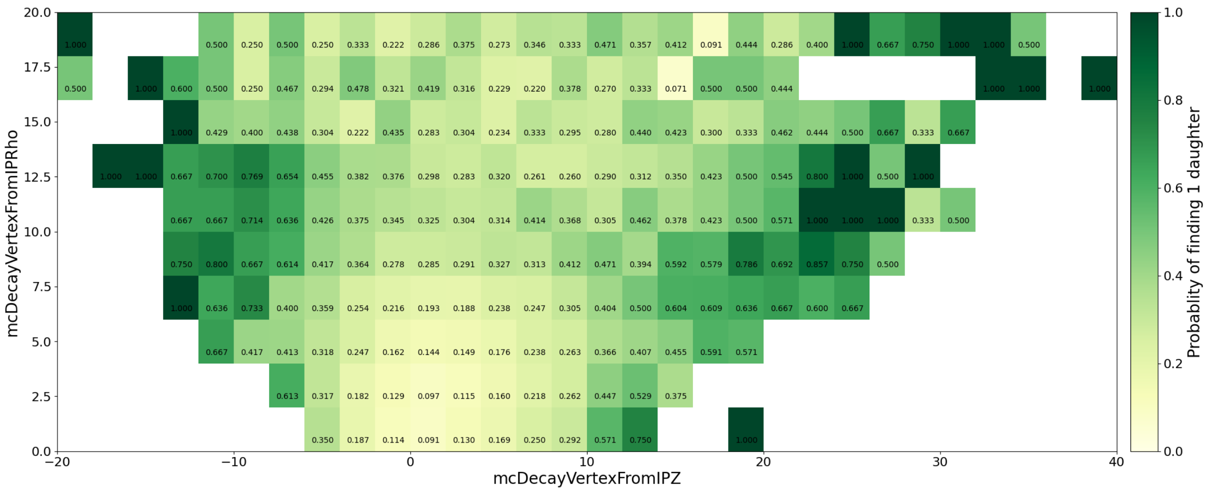

Figure 3.14: Probability of finding the E1 case as a function of the position of the K_S 's decay vertex.

Chapter 4

Algorithm to improve K_S tracking efficiency

This chapter presents a new algorithm to recover K_S mesons missed by the present track finding process, in particular the K_S that decays inside the SVD detector volumes in two charged pions, one reconstructed with the correct charge and one missed, the case E1 defined in Section 3.7.2).

After a brief introduction on the physics of the decay, with a focus on the kinematics of the two body decay, the new algorithm is described step by step. The results of its efficiency are reported for a particle-gun dataset, with and without beam background. The algorithm is implemented as a module in the Belle II software framework.

4.1 The K_S^0 decay

The K^0 is a strange meson, composed of a d quark and a $\overline{s}$ antiquark; at Belle II it is produced in the decay of heavier meson, where the b or c quark generates the s quark via weak decay processes (an example for each quark is reported in Fig. 4.1), or directly in the primary collision in the process $e^+e^- \to s\overline{s}$.

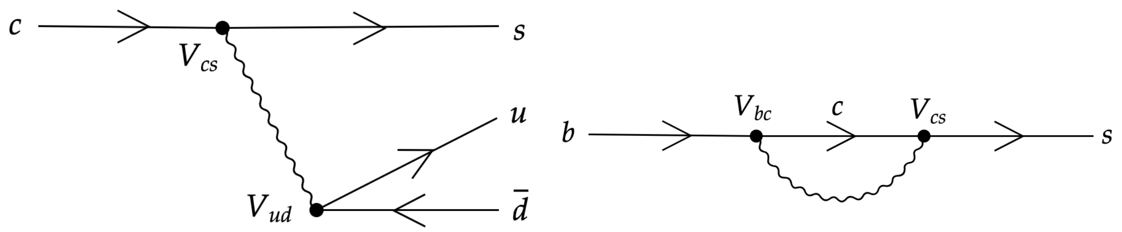

Figure 4.1: Feynman diagram of the examples of the b and c quark's weak decays in the s quark.

As described in Section 1.2.1, the K^0 has two mass eigenstates that differ little in mass and a lot in decay width. They are called K-short (K_S) and K-long (K_L), since they have quite different lifetimes: $(8.954 \pm 0.004) \cdot 10^{-11}$s for the K_S and $(5.116 \pm 0.021) \cdot 10^{-8}$s for the K_L [6].

Due to CPV in mixing, described in Section 1.2, the K_S and the K_L are not CP eigenstates and they can both decay in two pions (conserving CP for K_S and violating it for K_L) or three pions (violating CP for K_S). Nevertheless they both decay nearly always conserving CP, for example the branching fraction (BF) of $K_L \to \pi^+\pi^-$ is $1.967\,10^{-3}$ [6].

The most probable decays for the K_S are in two charged pions, with BF($K_S \to \pi^+\pi^-$)= 69.20 %, or in two neutral pions, BF($K_S \to \pi^0\pi^0$)= 30.69 %. For physics analysis, the K_S is usually reconstructed in the fist channel, $K_S \to \pi^+\pi^-$: it is more precise in the determination of the decay vertex position, since there are the tracks of the two charged daughters coming from it, and it is less affected by background.

The project of this thesis aims to recover K_S using only SVD information, hence it concerns only the ones decaying inside of this detector, more specifically inside the fifth layer, to have at least the two space points needed for the vertex fit. Inside this volume the maximum flight distance from the IP is around 31 cm. In Tab. 4.1 the average flight distances in the laboratory frame for K_S and K_L with different momenta are compared. The flight distance is calculated as $d = \beta\gamma c\tau$ where τ is the average decay time and $\beta\gamma$ is the ratio between the momentum and the mass of the particle in the laboratory framework.

Table 4.1: Average flight distances of K_S and K_L with different momenta in the laboratory frame.

p [GeV]	d_{K_S} [cm]	d_{K_L} [cm]
10^{-2}	0.05	30.82
0.2	1.08	616.39
0.3	1.6	$9.2 \cdot 10^2$
0.5	2.70	$15.41 \cdot 10^2$
1	5.39	$30.82 \cdot 10^2$
2	10.7	$61.4 \cdot 10^2$
3	16.18	$92.46 \cdot 10^2$
6	32.36	$184.92 \cdot 10^2$
7	37.76	$215.73 \cdot 10^2$

On average, a K_L decaying inside the fifth layer of the SVD needs to have a momentum less than < 10 MeV. Comparing such value with the K_L distribution of momentum in $B\overline{B}$ simulated events, plotted in Fig. 4.2 on the right, it shows that the probability to find a K_L decaying inside the SVD is low. Adding this fact to its extreme rare decay in two pions, I can safely assume that the new algorithm described in section 4.2 will recover only K_S (and in general the reconstruction of $\overset{(-)}{K^0} \to \pi^+\pi^-$ reconstruct only K_S).

The plot on the left of Fig. 4.2 shows that the majority of the K_S has the momentum less than 3 GeV, hence they mostly decay inside the SVD. In other types of events, for example $\tau^+\tau^-$ and $c\bar{c}$ the momentum spectrum of the particles is still quite soft and, in any case, the K_S momentum could not be more than ~ 7 GeV, that corresponds to the K_S produced directly from e^+e^- collision, completely forward (therefore not in the acceptance of the detector).

4.1.1 Kinematics

In a two-body decay, such as $K_S \to \pi^+\pi^-$, most of the kinematics is fixed by the mother particle's momentum: the only arbitrary variable is the angle α^* (see Fig. 4.3) between the momentum of one of the daughters in the center of mass (CM) frame and the direction of

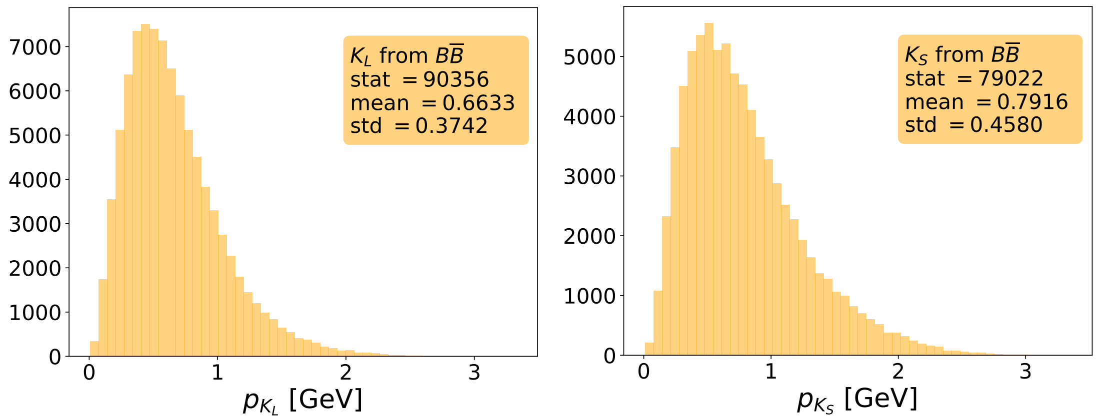

Figure 4.2: Momentum distribution of K_S (on the left) and K_L (on the right) particles in simulated $B\overline{B}$ events.

the CM frame, i.e. the momentum of the mother in the laboratory frame; the energies and momenta of the daughters in the CM are fixed by the conservation of the 4-momentum.

In Fig. 4.3 the schemes of the decay in the CM (on the left) and laboratory (LAB on the right) frames are drawn.

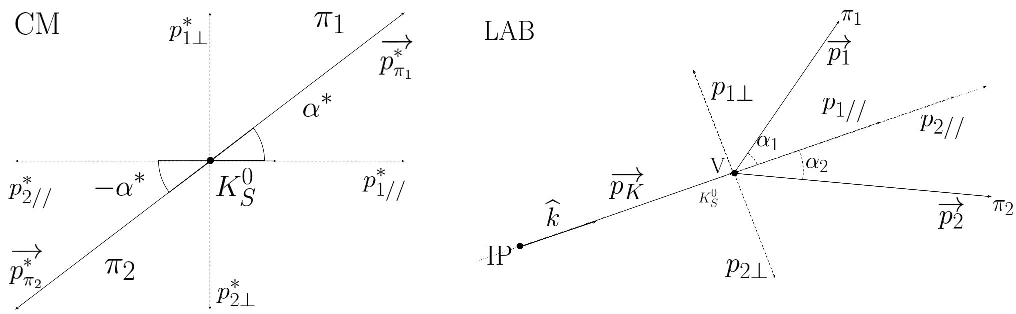

Figure 4.3: Two-body decay kinematics in the center of mass (CM, on the left) and laboratory (LAB, on the right) frames. The unit vector $\widehat{k}$ represents the direction of the K_S momentum in the laboratory frame. The other variables are described by Eq. 4.1 and 4.3

In the CM frame the 4-momenta of the mother particle (labeled with K) and the two daughter pions (labeled with $i = 1, 2$) are:

$$\begin{cases} P_K^* = (m_K, 0) \\ P_1^* = (m_K/2, \overrightarrow{p_1^*}), \quad |\overrightarrow{p_1^*}| = \sqrt{m_K^2/4 - m_\pi^2} \\ P_2^* = (m_K/2, \overrightarrow{p_2^*}), \quad \overrightarrow{p_2^*} = -\overrightarrow{p_1^*} \end{cases} \tag{4.1}$$

where the daughters' energies and momenta are calculated using the conservation of the 4-momentum:

$$P_K^* = P_1^* + P_2^*. \tag{4.2}$$

In the laboratory frame the 4-momentum of the daughters can be calculated by applying the Lorentz transformation with the boost $\beta\gamma$ of the mother particle:

$$P_K = (E_K, \overrightarrow{p_K}) \quad \gamma = E_K/m_K \quad \overrightarrow{\beta} = \overrightarrow{p_K}/E_K$$

$$P_1 = (E_1, \overrightarrow{p_1}) \quad P_2 = (E_2, \overrightarrow{p_2})$$
$$\begin{cases} E_i = \gamma(m_K/2 + \beta p^*_{i//}) \\ p_{i//} = \gamma(\beta m_K/2 + p^*_{i//}) \\ p_{i\perp} = p^*_{i\perp} \end{cases} \tag{4.3}$$

where the "*" indicate the quantities in the CM frame. Since $p_{i\perp}$ is by definition perpendicular to the boost $p_{i\perp} = p^*_{i\perp}$ and since $p^*_{1\perp} = -p^*_{2\perp}$ thus $p_{1\perp} = -p_{2\perp}$.

An interesting quantity to analyze is the product of the 4-momentum of the K_S, P_K, and one of the daughters, for instance P_1. Since it is a relativistic invariant, $P_K P_1$ generates the following equation:

$$m_K(m_K/2) - 0 = E_K E_1 - \overrightarrow{p_K} \cdot \overrightarrow{p_1} \tag{4.4}$$

where on the left side the quantity is calculated in the CM frame and on the right side in the laboratory frame. Replacing E_K with the known equivalent quantity $\sqrt{m_K^2 + p_K^2}$ and making explicit the scalar product between the momenta of the K_S and π, the following relation is obtained from Eq. 4.4:

$$\begin{gathered} \sqrt{m_K^2 + |p_K^2|}E_1 - |p_K| p_{1//} - \frac{m_K^2}{2} = 0, \\ \text{with } p_{1//} = p_1 \cos\alpha_1 = \overrightarrow{p_1} \cdot \widehat{k}, \end{gathered} \tag{4.5}$$

$p_{1//}$ is the projection of the pion momentum on the flight direction of the K_S ($\widehat{k}$). This relation (Eq. 4.5) will be used next in the algorithm described in section 4.2.

4.2 New algorithm

In the section 3.7.1, the source of inefficiency of the K_S reconstruction were presented and it was shown that the majority of the missed K_S are due to the failure of reconstruction of one of the daughters. The new algorithm aims to recover this case, labeled as E1, where one daughter is reconstructed with the correct charge and the other one is missed by the current track finder algorithm. The algorithm is based on the knowledge of the kinematics variables of the decay, described in the previous section by the Eq. 4.3.

Let's assume that the daughter labeled as "1" is correctly reconstructed ($\pi_1 = \pi_{reco}$), while the second is missed by the standard algorithm ($\pi_2 = \pi_{miss}$).

At this point it is useful to remember that the momentum $\overrightarrow{p_1}$ is a function of the position on the helix (s). Assuming that the energy loss by ionisation is negligible, the only known variable from the Eq. 4.3 is the absolute value of the π_{reco} momentum (p_1). The helix parameters of the π_{reco} and its momentum are known at the POCA ($s = 0$), but not at the decay vertex (s_V) of the K_S , since this is unknown as well, while the pion's momentum in Eq. 4.3 is the one at the decay vertex of the K_S .

If the information on the position on the vertex was known, the following variables could be computed in the given order:

- the 3-momentum of the π_{reco} , p_1, by extrapolating the helix at the K_S decay vertex; the extrapolation is along the fitted track, as discussed in section 3.5
- the energy of π_{reco} , using the well know equation $E_1 = \sqrt{m_\pi^2 + p_1^2}$
- the direction of the K_S momentum, $\widehat{k}$ (assuming the K_S comes from the IP)

- the parallel ($p_{1//}$) and perpendicular ($p_{1\perp}$) component of π_{reco} momentum to the direction of the K_S
- the perpendicular ($p_{2\perp}$) momentum of π_{miss} to the direction of the K_S since $p_{2\perp} = p_{1\perp}$
- the module of the K_S momentum, using Eq. 4.5 where that is the only unknown variable at this point
- the parallel ($p_{2//}$) momentum of π_{miss} to the direction of the K_S , since $p_{2//} = p_K - p_{1//}$
- the 4-momentum of the π_{miss}.

Therefore, fixing the vertex position and assuming that the K_S is coming from IP, every variable from Eq. 4.3 can be computed.

Most of the K_S in Belle II come from a D or B meson (if not directly by the e^+e^- collision), and since the size in z of the IP (the largest one), given by the intersection of the electron and positron beams (described in section 2.1), and the average flight distance of D and B mesons are of the order of 100 µm, the point of origin of the K_S can be assumed to be the interaction point (IP).

It's important to notice that the position of the K_S decay vertex is a one dimensional information: if I assume that the vertex is on the helix trajectory of the reconstructed daughter, just one coordinate is needed, all the others are fixed by Eq. 3.2.

The algorithm is divided in three main steps:

- make an hypothesis for the position of the decay vertex
- calculate the momentum of the K_S and the one of the missing π
- build the seed of the missing track with the momentum and the vertex from the previous steps, and search for SVD clusters in the regions around the SVD intercepts of the seed track.

4.2.1 Vertex selection

The position of the vertex can be delimited to be on the helix of the reconstructed pion, in particular on the helix arc between the inner most u and v pair of SVD clusters of the pion, from now on called *first hit*, and the *previous intercept*. The latter is defined as the intersection point of the backward extrapolation of the π_{reco} 's helix on the inner layer with respect to the *first hit*, as shown in Fig. 4.4. In particular, the selection will be done using the z coordinate of the two points.

4.2.2 Momenta calculation

After the estimation of the position of the decay vertex, the calculation of the K_S momentum is done using the following formula, obtained by isolating p_K in the equation 4.5

$$p_{K\pm} = \frac{m_K^2 p_{1//} \pm \sqrt{m_K^4 p_{1//}^2 - 4m_K^2(E_1^2 - p_{1//}^2)(m_K^2/4 - E_1^2)}}{2(E_1^2 - p_{1//}^2)}, \tag{4.6}$$

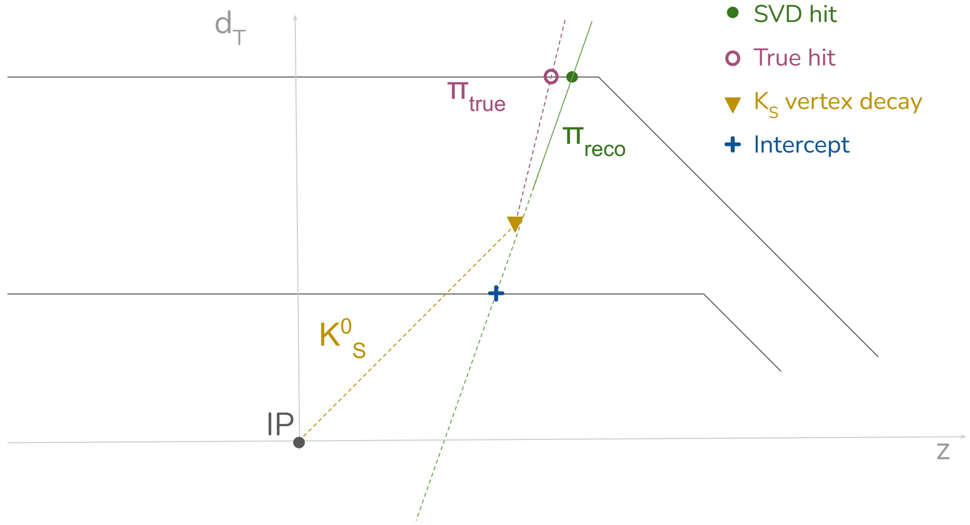

Figure 4.4: A sketch of two SVD layers between which the K_S particle (in yellow) decays, only one daughter, the reconstructed one is drawn (green for the reconstructed track and magenta for the actual trajectory given by the MC truth). The yellow triangle mark the position of the decay vertex, known by the MC truth, the magenta circle is the true position of the generation of the signal from the pion interaction with the detector (true hit), the green dot is the innermost hit attach to the track of the pion and the blue cross in the *previous intercept*.

where the two solutions are a consequence of the fact that Eq. 4.5 is a second degree equation. There is no reason why one of them should not be physical, on the contrary they come from the lack of knowledge of the K_S boost and thus of the $p_{2//}$ direction: it can be in the same direction of the K_S $(-)$ or in the opposite one $(+)$, creating two solution for the p_K and therefore also for p_2. Both of them need to be studied; obviously only one solution will be the right one, but it is impossible to know it a priori. The missing pion momentum is given by

$$p_{2\pm} = \sqrt{p_{1\perp}^2 + (p_{K_S\pm} - p_{1//})^2}, \tag{4.7}$$

and it is calculated for both solutions.

From now on I will refer to the two solutions as the *first* (the one with the '+') and *second* one (with the '−'). To help readability from now on I will change the notation for the pions as well, the index 1 will be replaced by the label *reco* and the index 2 by the label *miss*. For example p_2 will be from now on indicated as p_{miss}).

4.2.3 Building the π_{miss} track

By using the estimation of the vertex position and the calculated missing momentum, a temporary helix is built, and it is used to search for SVD clusters belonging to the missing pion. Essentially, the algorithm is looking for SVD clusters in the vicinity of the intercept of the π_{miss} seed track with the SVD layers outside the estimated decay vertex. Both helices, coming from the two solutions of the K_S (see Eq. 4.6) and π_{miss} momenta, are constructed and are retained at this stage.

4.2.4 Performance quantities

For the implementation of this algorithm at least three quantities should be calculated to study its performance: the efficiency, the fake rate and the execution time of the module.

At this stage, the most important quantity to measure is the fraction of the K_S that the algorithm manages to recover (efficiency) in absence of beam background. Even without background the algorithm could fail in different ways: the calculation of the π_{miss} 's momentum or the research of the correct clusters could fail, for example if the π_{miss} 's temporary helix does not intercept the correct sensor, i.e. the one with the clusters related to the π_{miss} 's track.

When adding the background the efficiency will probably decrease because of the higher occupancy of the sensor and the difficulty to select the correct clusters of the π_{miss} 's track among the many clusters created by beam background. Moreover there will be an increase of the fake rate, the fraction of reconstructed tracks that are not actually related to the missing daughter's MCParticle, that needs to be studied.

The third thing to take in consideration is the execution time: as said before the same software is usually used both for online and offline reconstruction, hence the algorithm should be developed to stay inside the time limit given by the HLT. Ideally the algorithm should be applied only to pions coming from a K_S not already reconstructed, but this is obviously impossible to know. Applying it to all the tracks is also not possible and not efficient, therefore some selections will be needed. Apart from the obvious selection to not apply the algorithm to tracks that the $V0$ finder already assign to a $V0$ vertex other possible selections to consider are:

- the position of the innermost VXD hit
- the momentum associated to the track
- the PID information from other detectors.

For this thesis I focus on the computation of the efficiency of the algorithm: with poor efficiency the estimation of the fake rate and execution time are not needed. The purity and the execution time calculation are therefore beyond the purpose of this thesis.

In the next section the algorithm will be applied to a data sample generated with a particle gun. The relative efficiency of each step will be discussed to better understand the weak steps of the algorithm in terms of efficiency. The total efficiency of the algorithm will be the product of the relative efficiencies of each step:

$$\epsilon = \epsilon_{vtx} \cdot \epsilon_{p\pi} \cdot \epsilon_{1i} \cdot \epsilon_{1h} \cdot \epsilon_{2i} \cdot \epsilon_{2h}, \tag{4.8}$$

where:

- ϵ_{vtx} is the efficiency in the selection of the z range of the vertex between *first hit* and *previous intercept*
- $\epsilon_{p\pi}$ is the probability to have at least one solution for the momentum of the missing pion after a selection on the momentum of the K_S
- ϵ_{1i} is the probability to find an intercept for the missing track inside the same sensor of its true SVD cluster
- ϵ_{1h} is the probability to find a pair of u and v SVD clusters (one SVD hit) in the vicinity of the intercept that are related to the π_{miss} MCParticle

- ϵ_{2i} and ϵ_{2h} are defined similarly to ϵ_{1i} and ϵ_{1h} but for the second intercept and relative hit.

Possible improvement I already anticipate possible improvement, discussed deeper in section 5.3, that can be taken into consideration if the efficiency is not satisfactory. This algorithm could be extended by also using information coming from the PXD and the CDC; it can also be improved taking in account the dead areas of the SVD detector between the sensors. It is expected that these additions would affect the performance of the algorithm in the choice of the position of the vertex, in the search for hits near the extrapolated π_{miss} track and its building.

4.3 Study with a particle gun data set

To study the performance of the algorithm a dedicated non physical data set has been generated with a particle gun: each generated event is just one K_S produced at the IP, decaying in two charged pions with a uniform distribution inside the SVD detector volume, as shown in Fig. 4.5, and a uniform K_S momentum distribution between 0 and 3 GeV; as anticipated, the beam background is not simulated at first. I generated a total of 40000 events with the particle gun but I saved only the events with both the charged daughters of the K_S inside the SVD acceptance: the (45.4 ± 0.2) % of the generated sample survives the selection.

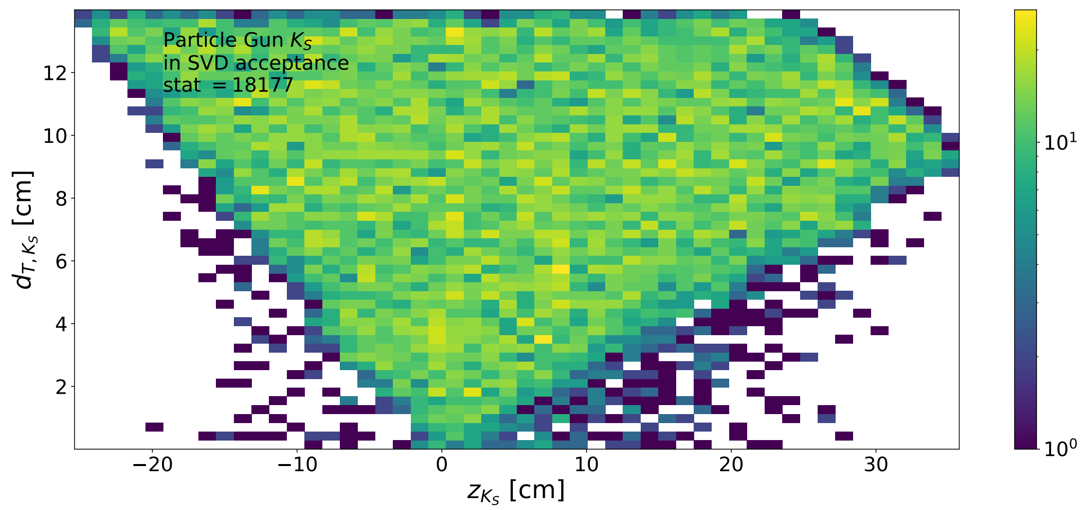

Figure 4.5: Uniform K_S decay vertex distribution of the particle gun sample. The events represented are K_S decaying into two charged daughters both in the SVD acceptance.

E1 in particle gun

From the particle gun sample I selected the E1-type K_S that decay inside the fifth SVD layer, they are 2523 events, i.e. the (13.9 ± 0.3) % of the saved sample. This will be my base data sample on which the algorithm will be tested.

Fig. 4.6 reports the distribution of the true momentum of the missing and reconstructed pions. As expected, the range of the distributions is less than 3 GeV since that is the maximum momentum of the mother particle. The main difference between the two distributions is at low momentum where the π_{miss} momentum histogram is more populated. Indicating that the standard tracking is less efficient on low-momentum displaced pions.

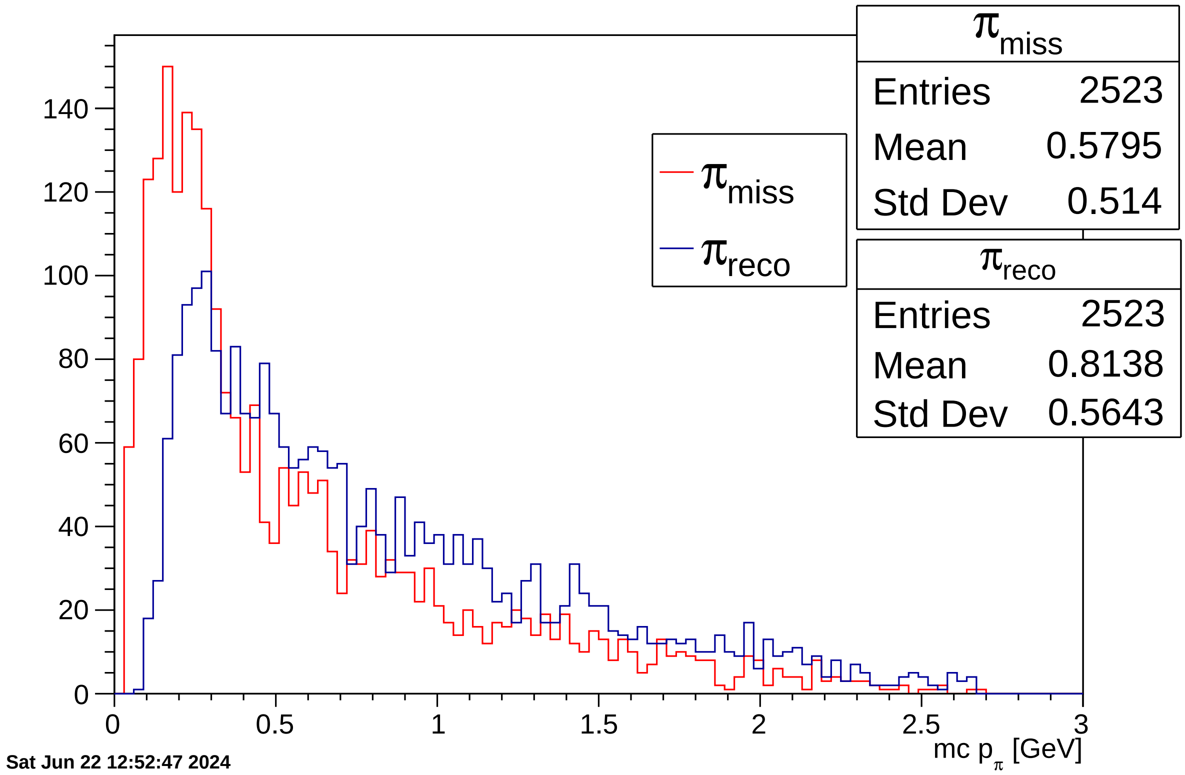

Figure 4.6: Distribution of the true momentum of the missing pion in blue and in red the true momentum of the reconstructed pion.

4.3.1 Vertex selection

As said in the previous section, the estimation of the vertex is done by delimiting the region of its position to the helix arc of the reconstructed daughter between the *first hit* (the innermost SVD u and v clusters pair) and the *previous intercept* (the intercept of the backward extrapolation of the track with the previous layer).

The *first hit* is identified as the two innermost SVD clusters (u and v pair) related to the π_{reco} track; if no SVD clusters are found[1], this is due to a failure of the CKF from the CDC to the SVD (explained before in section 3.5.1) and of the VTXTF2.

After the identification of the *first hit*, the *previous intercept* is searched for. The π_{reco} track is extrapolated backward towards infinite planes containing the SVD sensors (of the previous layer). The extrapolation returns the local position on the plane and the extrapolation uncertainties along the u and v direction, σ_u and σ_v. From the list of

[1]**Missing SVD clusters:** I discovered that this happens almost always when the K_S has decayed after L5 (events that the algorithm does not take into consideration), when adding the background, it increases for the K_S that decays before L5 as well; this problem is not investigated further in this context.

the intercepts the last one[2] inside the sensitive area within one σ_u and σ_v is selected as *previous intercept*.

If no intercept satisfying the above criteria exists, the POCA of the π_{reco} track is used, this happens $(27.5 \pm 0.9)\,\%$ of the times that the *first hit* is found. It is important to notice that this always happens when the innermost hit is on the third layer of the SVD. Since there are no previous SVD layers, the *previous intercept* does not exist. Overall the algorithm is built to always define a *previous intercept* (or POCA) if the *first hit* exists.

For the next step an hypothesis on the position of the vertex needs to be made. In Fig. 4.7 a sketch explains how the cylindrical coordinates of the K_S vertex can be delimited: while on z and d_T the vertex range is given by the *first hit* and *previous intercept* coordinates:

$$\begin{aligned} min(z_i, z_h) < z_V < max(z_i, z_h) \\ min(d_{T,i}, d_{T,h}) < d_{T,V} < max(d_{T,i}, d_{T,h}), \end{aligned} \tag{4.9}$$

where z_h and z_i are the z coordinate of the *first hit* and of the *previous intercept*, respectively; this is not the case for the φ coordinate.

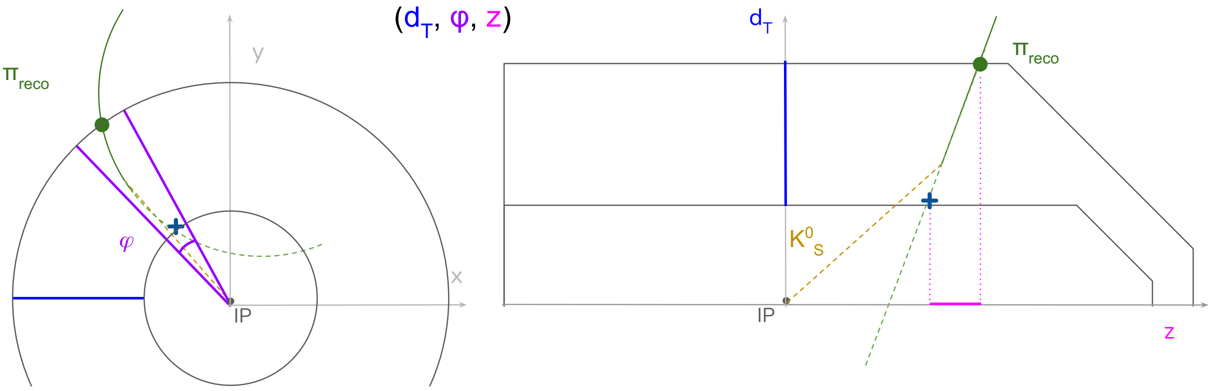

Figure 4.7: Frontal and lateral sketch of the reconstructed track. Respectively in green and blue are marked the *first hit* and the *previous intercept*, between which the position of the vertex is assumed to be. In blue, purple and fuchsia are marked the range of the coordinate to have the vertex inside such region.

Therefore a slightly different approach is adopted: the hypothesis on the position of the vertex is taken by fixing the z coordinate and calculating the global position on the transverse plane x and y with the Eq. 3.2. Three hypotheses are considered for the z position of the vertex:

$$\begin{aligned} (i) \quad & z_V = \tfrac{z_h+z_i}{2} \\ (ii) \quad & z_V = \tfrac{z_h+z_i}{2} - \tfrac{|z_h-z_i|}{4} \\ (iii) \quad & z_V = \tfrac{z_h+z_i}{2} + \tfrac{|z_h-z_i|}{4}. \end{aligned} \tag{4.10}$$

In the next section (4.3.2) how the choice among the three hypotheses is made will be explained .

The percentage of K_S that have the z coordinate of the vertex inside the selected range ϵ_{vtx} is $(88.6 \pm 0.6)\,\%$; the inefficiency is divided into:

- missing SVD cluster of the π_{reco} track, $(55 \pm 3)\,\%$

[2]we need to take the last one given the order of the ladders on which the intercepts are created

- use of the POCA as *previous intercept*, $(23 \pm 2)\,\%$
- wrong *first hit*, $(22 \pm 2)\,\%$.

The last one refers to a inefficiency of the current tracking algorithm to attach all the SVD hits to the π_{reco} track, if the innermost hit is not attached to the track I will not recover it and the *first hit* will be identified with one of the next ones. Fig. 4.8 reports the residual of the z, φ and d_T coordinates of the vertex: the distribution in green represents the events that pass the selection on the vertex for the calculation of the efficiency (true K_S decay vertex inside the z range delimited by the *first hit* and the *previous intercept*), the one in red represents those that fail this selection. The residuals are defined as the difference between the true position of the K_S decay vertex and the estimated one using one of the hypotheses made for the vertex listed in Eq. 4.10.

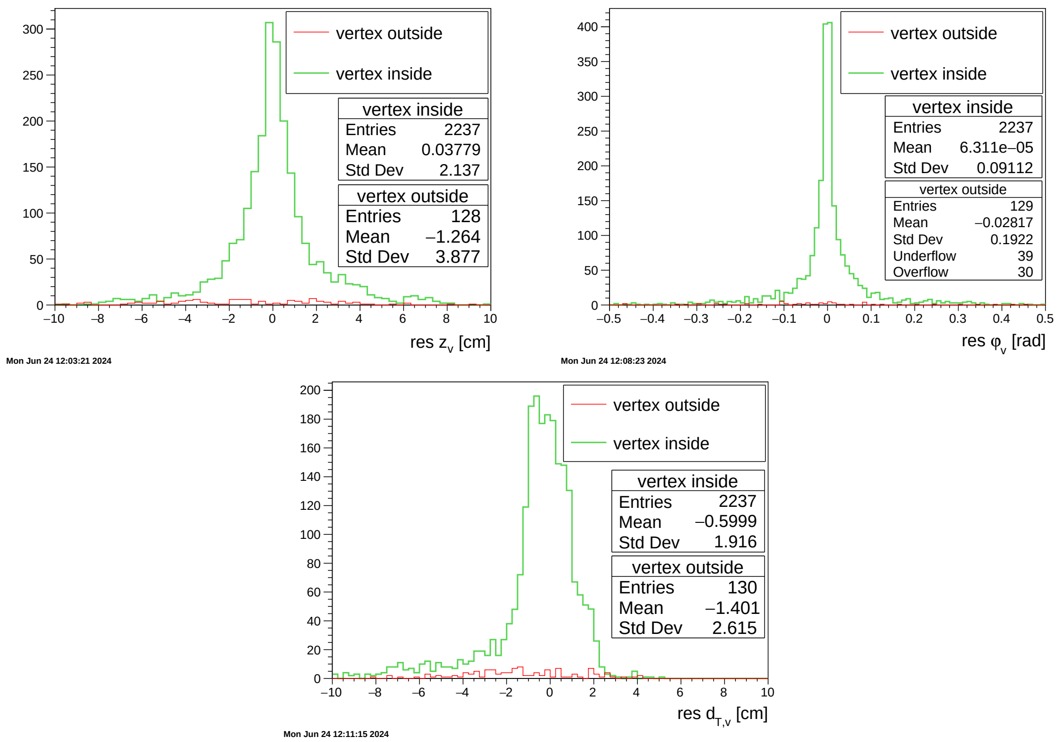

Figure 4.8: Residual of the z, φ and d_T coordinates of the vertex estimated using the hypotheses listed in Eq. 4.10. The red histogram refers to those events whose the true vertex is not inside the selected z range, while the green one refers to those that have the true K_S decay vertex in the range.

The asymmetry in the transverse distance coordinate d_T is due to the order on which the three hypotheses are tested.

4.3.2 Momenta calculation

When calculating p_K using the equation 4.6, two things need to be remarked:

- the ambiguity of the two possible solutions (mentioned in section 4.2.2 as well)
- the square-root whose rooting could be negative if the hypothesis of the vertex is not the correct one.

The last observation intrinsically links the vertex position hypothesis with the calculation of the K_S momentum, in particular a different hypothesis (from Eq. 4.10) is made if with the previous one the rooting results negative.

The hypotheses are made on the z coordinate and are chosen in the same order as they are written in Eq. 4.10. If, with the first one, the rooting in Eq. 4.6 is negative, the second one is tried, the rooting is checked again and so on; if the rooting is still negative after the third hypothesis (this happen around 1 % of times) no other hypothesis is made (the third one is kept), but the rooting itself is fixed to be zero. In Fig. 4.9 the residuals of the K_S momentum for all the events that pass the selection on the vertex and for those that have the square root fixed to zero are reported; the latter don't deviate much from the zero with respect to the first distribution, in particular for the first solution.

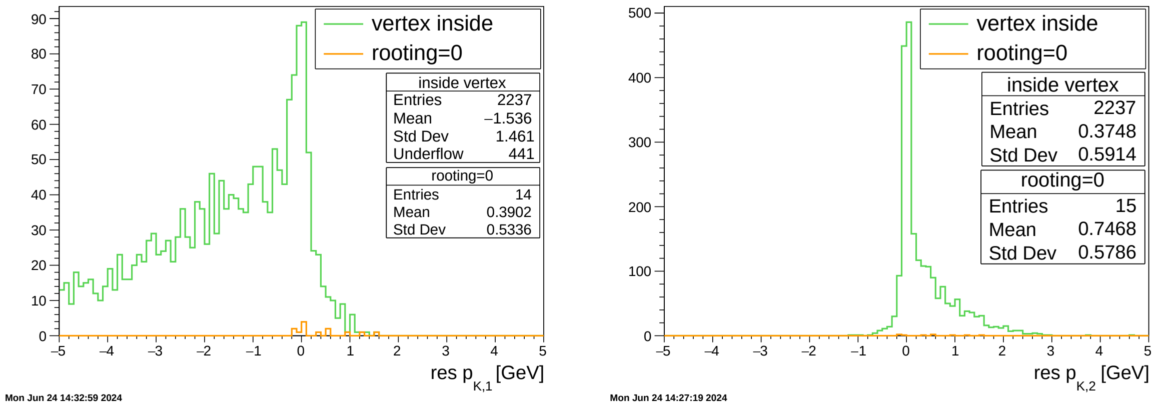

(a) *First solution* (b) *Second solution*

Figure 4.9: The residuals of the K_S momentum for all the events that pass the selection on the vertex (in green) and for those that have the square root fixed to zero (in orange).

Fig. 4.10 reports the residuals of the K_S momentum for the events that don't have the vertex inside the z range and those that pass this selection.

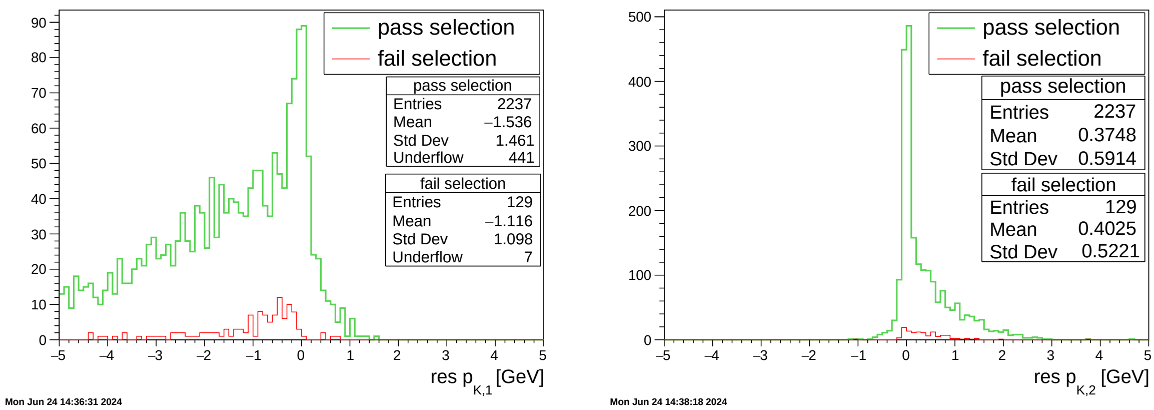

(a) *First solution* (b) *Second solution*

Figure 4.10: The residuals of the K_S momentum for all the events that pass the selection (in green) and for those that don't have the true vertex inside the selected z range (in red).

This selection on the vertex is not highly efficient in the selection of the correct K_S

momentum, few K_S are discarded and only in the tails; this is expected since the range in z (reported in Fig. 4.11) is quite large for K_S in the forward and backward direction and these kinds of K_S are common in the E1 case (see Fig. 3.14). It is observed that the first solution returns momentum with a large residual (larger than 1 GeV) and the second one has a more pronounced peak at zero and the tails are smaller. This suggests that the second solution is the favorite one and it will be confirmed by next observations.

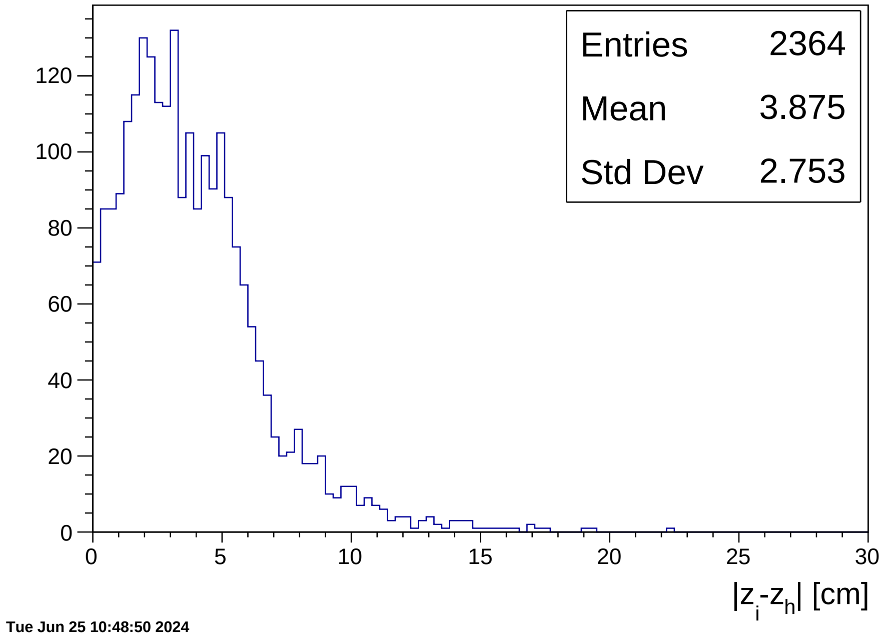

Figure 4.11: Range in z delimited by the *first hit* and the *previous intercept*.

By looking at the 2D distribution of the two solutions in Fig. 4.12, it is visible how in some cases it is possible to exclude one of the two solutions since the momentum can not be negative (Eq. 4.6 calculates the magnitude) and can not be more than 7 GeV in Belle II, actually, from simulation of $B\overline{B}$ events in Fig. 4.2, there are already very few K_S at 3 GeV for instance.

From now on, I select the reconstructed momentum of the K_S to be in $[0, 3]$GeV, since it is also the range chosen in the particle gun production. Fig.4.12 shows that the cut on the lower edge is more relevant for the second solution while the cut on the higher edge is more relevant for the first solution. The events that are excluded from both solutions are less than 3 %; it should be noted that is possible to recover one of the two solutions: the first solution if $p_K < 0$ GeV (in absolute value) and at the second if $p_K > 3$GeV. But these events are anyway lost in the next step when searching for the π_{miss} intercepts (in section 4.3.3). This cut on p_K is one of the selections to optimize later on for the performances in the physics samples.

At this point, the momentum of the missing pion is calculated using Eq 4.7. Fig. 4.13 reports the distributions of the π_{miss} 's momentum for the two solution, both for the K_S that pass and do not pass the previous selections for the calculation of the efficiency: the cut on K_S momentum and the one on vertex (to be inside the z range created by the *first hit* and the *previous intercept*).

The percentage of K_S that pass the selections for at least one of the two solutions $\epsilon_{p\pi}$ is (97.8 ± 0.3) %: (47.0 ± 1.1) % have at least the first solution and (92.6 ± 0.6) % have at least the second one. The second solution has a higher efficiency and narrower residuals,

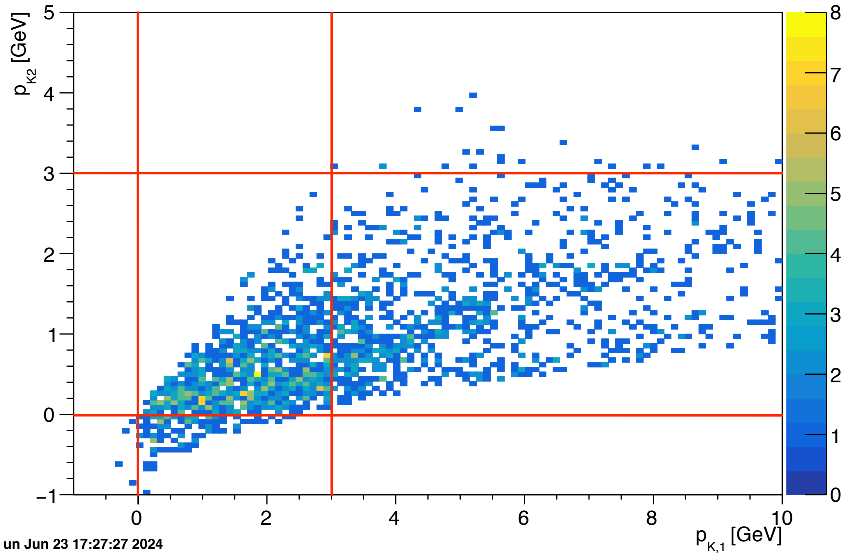

Figure 4.12: 2D-distribution of the K_S momentum's two solutions, on the x axis the first solution and on the y axis the second one. The red lines indicate the cut made to exclude one or both the solutions.

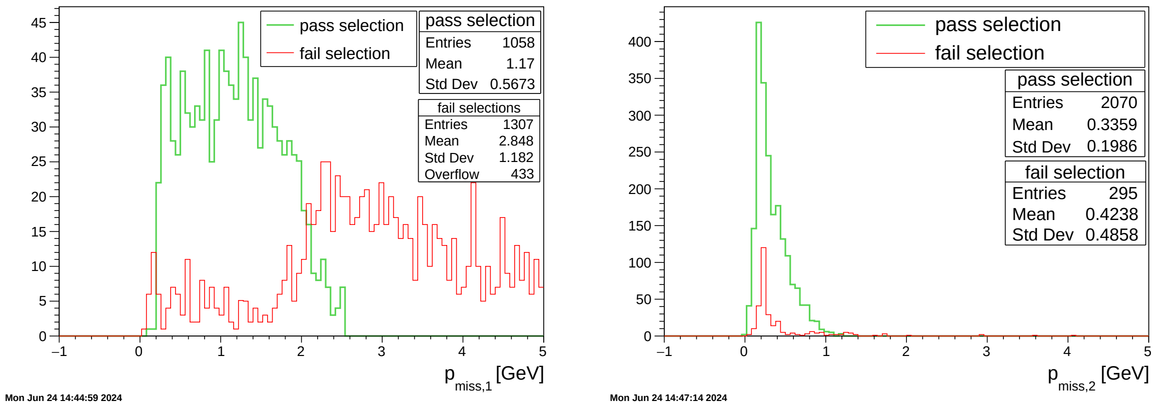

(a) *First solution* (b) *Second solution*

Figure 4.13: The π_{miss} momentum for the two solutions, in red the events that fail the selection on the vertex or on the momentum of the K_S , in green those that pass it.

as shown in Fig. 4.14.

The first solution tends to overestimate the π_{miss} momentum (being the solution with the $+$), then it is more precise for smaller π_{miss} momentum, while the second solution underestimates it and it is a better estimator for π_{miss} at higher momentum. Thus the first solution refers to the $p_{miss//}$ in the opposite direction of the K_S momentum, and the second one refers to $p_{miss//}$ in the same direction, as was anticipated in section 4.2.2.

4.3.3 Adding clusters

With the hypothesis on the vertex and the relative π_{miss} momentum, a temporary helix is built. The track is extrapolated to all the SVD layers outside the position of the estimated vertex and the intercepts that are inside the active area of the sensors within one σ (both

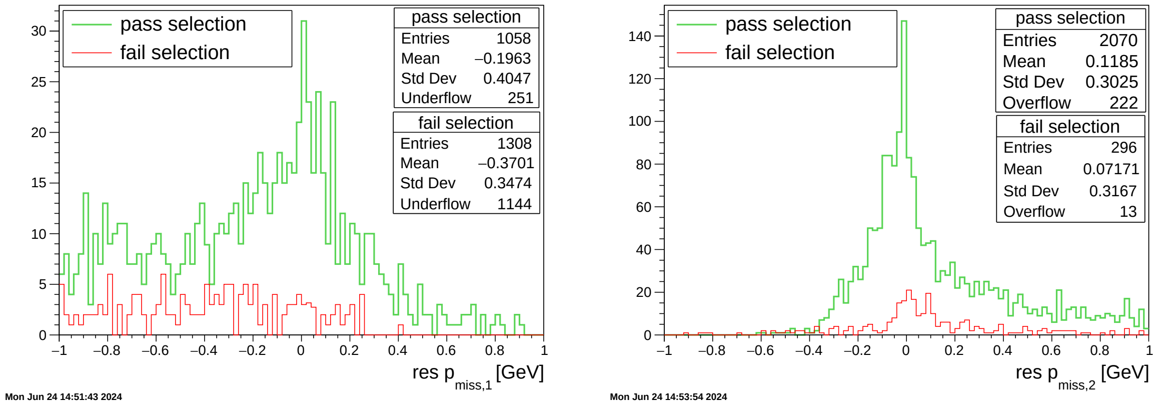

(a) *First solution* (b) *Second solution*

Figure 4.14: The residuals of the π_{miss} 's momentum for the two solutions, with in red the events that do fail the selection on the vertex or on the momentum of the K_S .

in u and v) are selected to search for SVD clusters.

Fig. 4.15 and 4.16 reports the residuals (always defined as $MC - reco$) of the local coordinates of the first and the second intercepts, the plots shown here are just the one for the second solution since it is has more statistics. Fig. 4.17 reports the plots of the local coordinates' residuals of the closest u and v clusters for the first and the second intercepts of track for the second solution. In all these plots two distributions are reported:

- the ones in blue represent all the events, even those that do not pass the selection, obviously they still need a true SVD cluster on the sensor hit by the intercept to calculate the residuals
- the ones in green represent the events that pass the selection for the calculation of the efficiency (ϵ_{1i}, ϵ_{1h}, ϵ_{2i} and ϵ_{2h}).

It is important to notice from Fig. 4.17, that almost half of the clusters that are in the vicinity of the intercept and peaking at zero are not selected, this is caused by the fact that it is required that both u and v clusters are related to the π_{miss} MCParticle: so a cluster may be selected in u but not in v or vice-versa. More about this is discussed in section 5.3.

The probability to have at least one intercept on the SVD sensor with the true SVD hit for at least one of the two solutions is $\epsilon_{1i} = (58.4 \pm 1.0)\,\%$: $(24.6 \pm 0.9)\,\%$ for the first solution and $(55.8 \pm 1.1)\,\%$ for the second one.

For these intercepts, the u and the v clusters closest to the intercept, not farther than $5\sigma_u$ and $5\sigma_v$ respectively are selected as *closest hit*. The probability ϵ_{1h} from Eq. 4.8 that this closest hit is found and it is related to the π_{miss} MCParticle is $\epsilon_{1h} = (11.6 \pm 0.9)\,\%$: $(12.1 \pm 1.4)\,\%$ for the first solution and $(11.3 \pm 0.9)\,\%$ for the second one. At this point the same probabilities are defined for the second intercept, $\epsilon_{2i} = (61 \pm 4)\,\%$, and its closest hit, $\epsilon_{2h} = (26 \pm 5)\,\%$. For the first solution $\epsilon_{2i} = (65 \pm 5)\,\%$ and $\epsilon_{2h} = (9 \pm 4)\,\%$. For the second solution $\epsilon_{2i} = (61 \pm 4)\,\%$ and $\epsilon_{2h} = (26 \pm 5)\,\%$.

In Tab. 4.2 a summary of the relative efficiencies for the first, second and at least one solution is reported.

Till the search of the first π_{miss} intercept the algorithm efficiency remains high enough, however it drops when the *first hit* is searched for, this may due to the quality of the

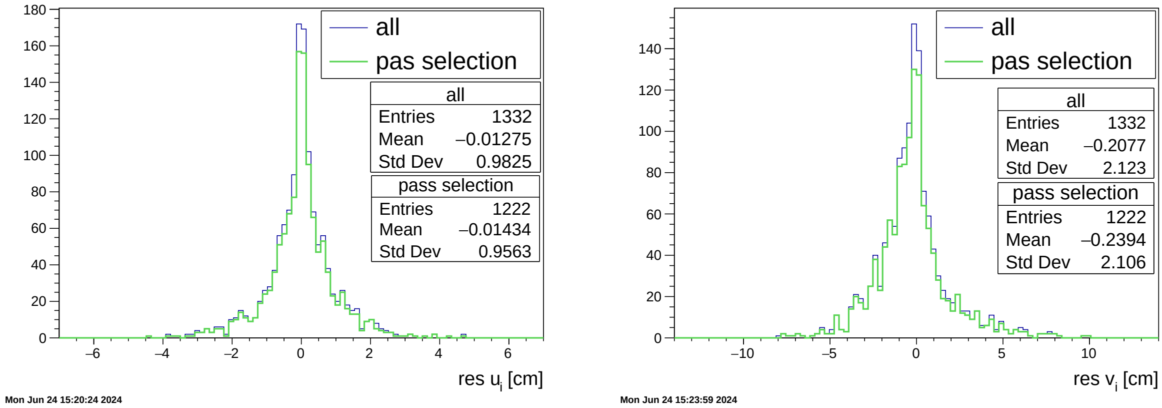

(a) *First intercept*

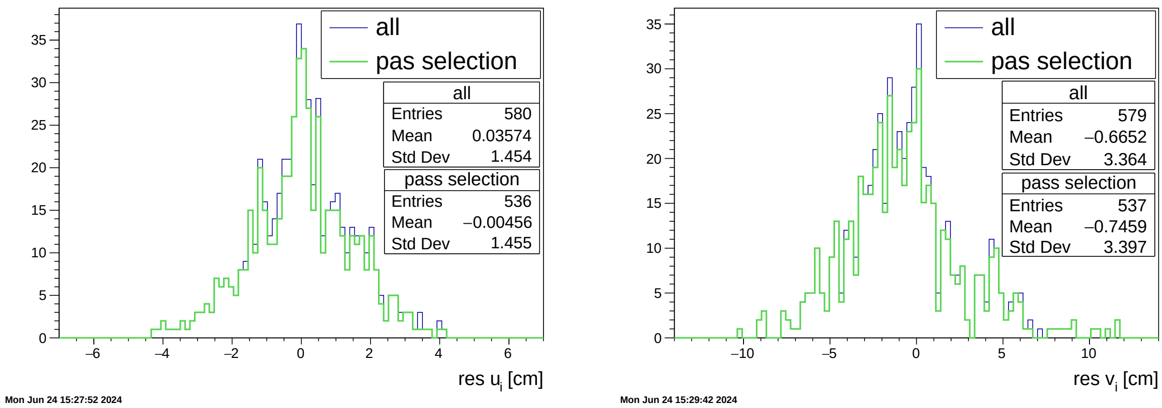

(b) *Second intercept*

Figure 4.15: Residuals on the local u and v coordinates of the intercepts on the first and the second intercepts for the second solution. In green the intercepts that pass the selections. In blue all of them (if there is a true SVD cluster on the same sensor).

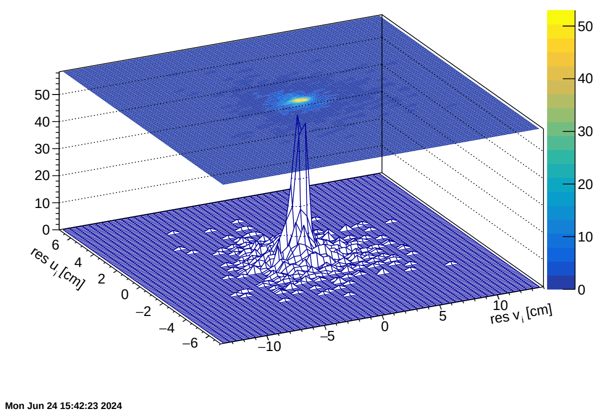

(a) *First intercept*

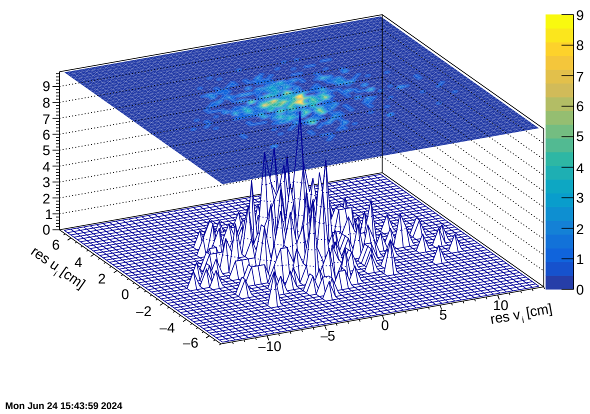

(b) *Second intercept*

Figure 4.16: Residuals of the local coordinates of the first and the second intercepts for the second solution in two dimensions.

seed track. Another thing to notice is that ϵ_{2h} is higher than ϵ_{1h}, meaning that if the extrapolation at the first intercept is correct it is more probable to find the second one. Improvements are discussed in section 5.3.

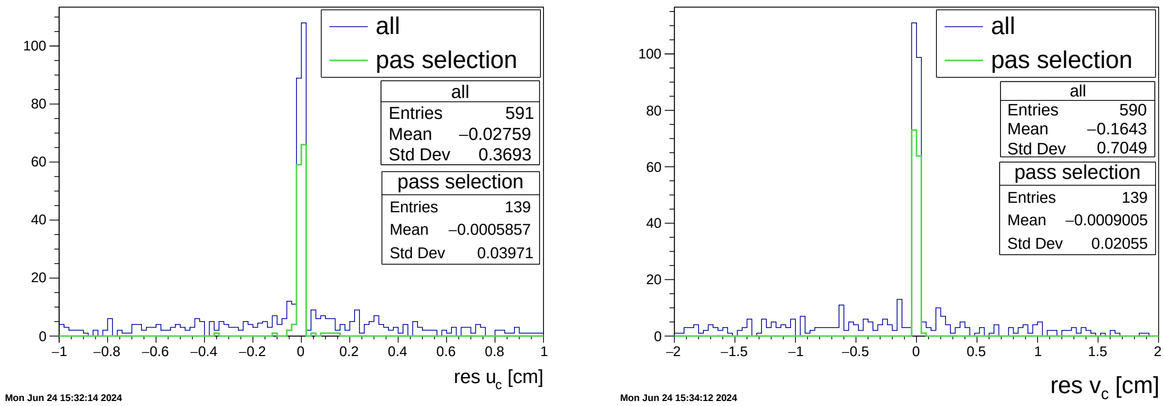

(a) *First cluster*

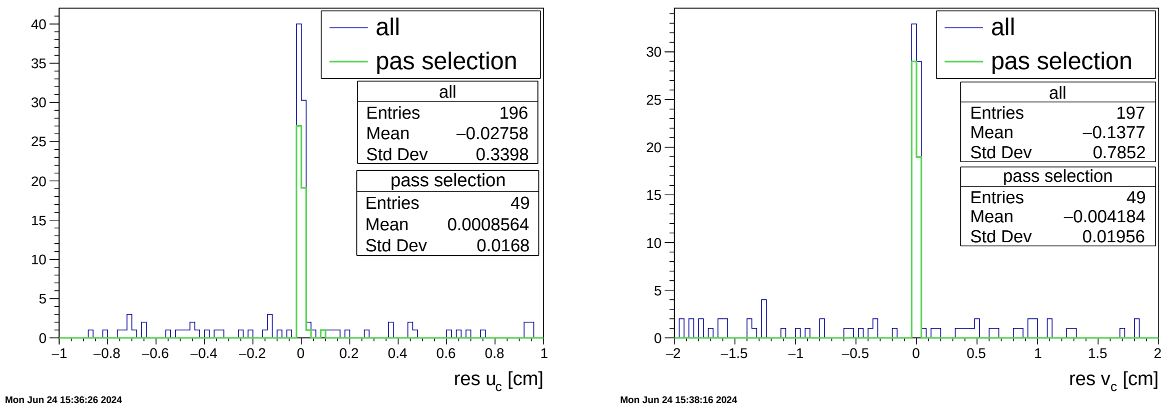

(b) *Second cluster*

Figure 4.17: Residuals on the local u and v coordinates of the closest clusters on the first and the second crossed layers for the second solution. In green the clusters that pass the selections. In blue all of them (if there is a true SVD cluster on the same sensor).

Table 4.2: Relative efficiencies calculated in the particle gun sample. The overall efficiency is the product of the efficiencies for at least one solution of that row and the rows above.

	solution 1	solution 2	at least one solution	overall efficiency
ϵ_{vtx}	-	-	$(88.6 \pm 0.6)\,\%$	$(88.6 \pm 0.6)\,\%$
$\epsilon_{p\pi}$	$(47.0 \pm 1.1)\,\%$	$(92.6 \pm 0.6)\,\%$	$(97.8 \pm 0.3)\,\%$	$(86.7 \pm 0.7)\,\%$
ϵ_{1i}	$(24.6 \pm 0.9)\,\%$	$(55.8 \pm 1.1)\,\%$	$(58.4 \pm 1.0)\,\%$	$(50.6 \pm 1.0)\,\%$
ϵ_{1h}	$(12.1 \pm 1.4)\,\%$	$(11.3 \pm 0.9)\,\%$	$(11.6 \pm 0.9)\,\%$	$(5.9 \pm 0.5)\,\%$
ϵ_{2i}	$(65 \pm 5)\,\%$	$(61 \pm 4)\,\%$	$(61 \pm 4)\,\%$	$(3.6 \pm 0.4)\,\%$
ϵ_{2h}	$(9 \pm 4)\,\%$	$(26 \pm 5)\,\%$	$(26 \pm 5)\,\%$	$(0.91 \pm 0.19)\,\%$

4.4 Adding background

To see how the beam background affects these results, I simulated the same events from the particle gun (generated with the same random seed) with the background simulated for Run 1.

Of the 40000 generated events the $(9.01 \pm 0.14)\,\%$ are the E1 case with both daughters inside the fifth layer of the SVD, versus the $(6.31 \pm 0.12)\,\%(= 45.4\,\% \cdot 13.9\,\%)$ of before.

The fact that I observe a higher probability of the E1 case with background with respect to the no background case is expected, since the background reduces the efficiency of tracking.

The algorithm is applied as described before. In the following we discuss the performance of each step.

Vertex selection The vertex is fixed as before and the same selection is applied to it for the computation of the algorithm's efficiency. The probability to have the z coordinate of the vertex between the *first hit* and the *previous intercept* in this sample is ϵ_{vtx} : $(68.6 \pm 0.8)\,\%$; its inefficiency is divided into:

- no SVD clusters attached the π_{reco} track, $(72.5 \pm 1.3)\,\%$
- use of the POCA as *previous intercept*, $(11.6 \pm 1.0)\,\%$
- wrong *first hit*, the rest , $(15.9 \pm 1.1)\,\%$.

With respect to the sample without background the inefficiency due to the missing *first hit* has increased, this is no surprise since it is due to a degradation of the performance of the current tracking algorithm. While it has decreased the failure due to the use of the POCA.

Fig. 4.18 reports the distribution of the estimated vertex's residuals.

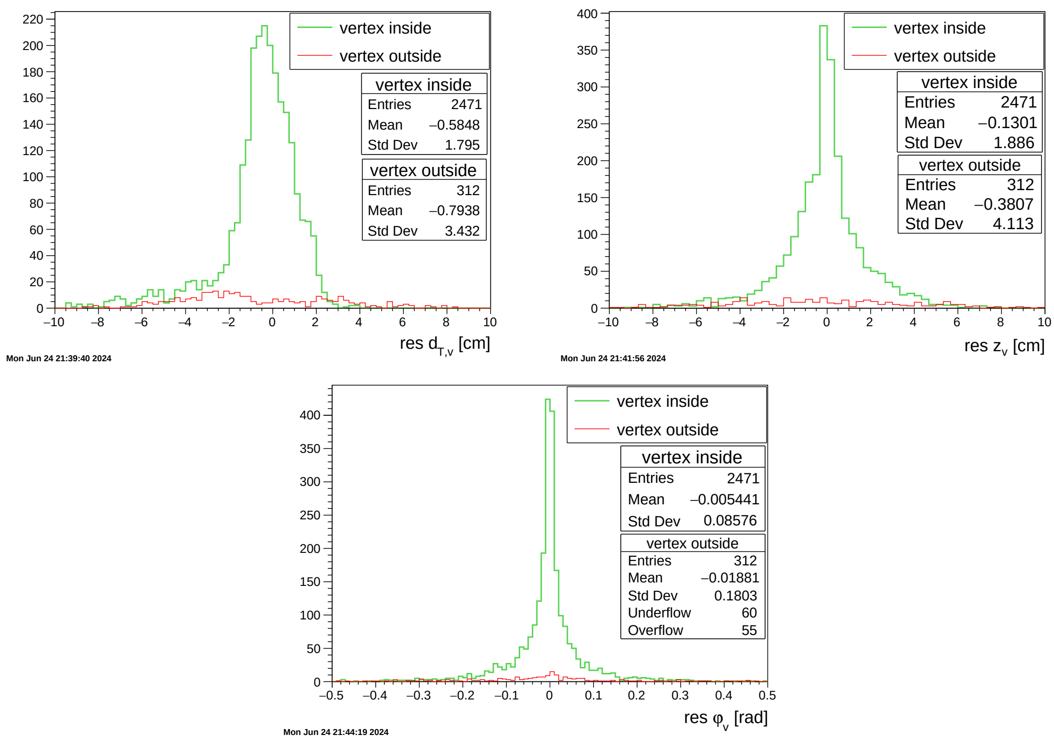

Figure 4.18: Residual of the z, φ and d_T coordinates of the vertex estimated using the hypotheses listed in Eq. 4.10, in the particle gun data sample with background. The red histogram refers to those events whose the true vertex is not inside the selected z range, while the green one refers to those that have the true K_S decay vertex in the range.

Momenta calculation The K_S momentum is then calculated and the same cut on K_S momentum is applied as before. The $(96.8 \pm 0.4)\,\%$ of times at least one solution passes the selection: $(48.8 \pm 0.9)\,\%$ for the first solution and $(90.2 \pm 0.5)\,\%$ for the second one. Fig. 4.19 reports the distribution of the π_{miss} momentum's residuals.

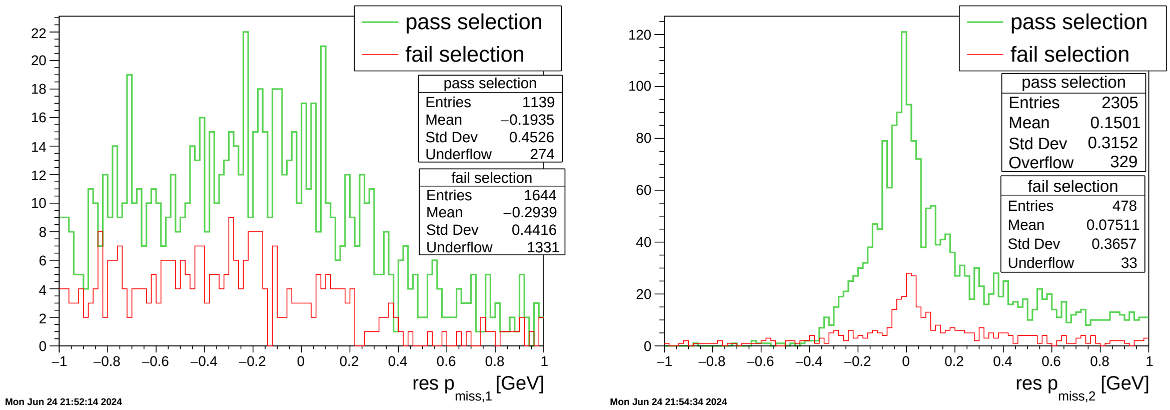

(a) *First solution* (b) *Second solution*

Figure 4.19: The residuals of the π_{miss} 's momentum for the two solutions in the particle gun data sample with background, with in red the events that do fail the selection on the vertex or on the momentum of the K_S .

Adding clusters The probabilities ϵ_{1i}, ϵ_{1h}, ϵ_{2i}, ϵ_{2h} are defined and calculated as before, the results are reported in Tab. 4.3.

Table 4.3: Probabilities to find one or two consecutive intercepts and one or two consecutive clusters related to the π_{miss} MCParticle.

	sol 1	sol 2	at least one sol
ϵ_{1i}	$(25.9 \pm 0.9)\,\%$	$(60.4 \pm 1.0)\,\%$	$(61.9 \pm 1.0)\,\%$
ϵ_{1h}	$(12.6 \pm 1.3)\,\%$	$(10.3 \pm 0.8)\,\%$	$(10.7 \pm 0.8)\,\%$
ϵ_{2i}	$(78 \pm 5)\,\%$	$(74 \pm 4)\,\%$	$(75 \pm 3)\,\%$
ϵ_{2h}	$(30 \pm 6)\,\%$	$(29 \pm 4)\,\%$	$(30 \pm 4)\,\%$

Fig. 4.20 and 4.21 reports the distribution of the intercepts and clusters' residuals for the second solution.

In Tab. 4.4 a summary of the algorithm efficiency is reported for this sample. With respect to the particle gun data sample without background, the efficiency ϵ_{vtx} is lower , this is caused by the degradation of the efficiency of the CKF with background to attach SVD clusters to the CDC track of the π_{reco} . The other relative efficiencies do not have remarkable differences.

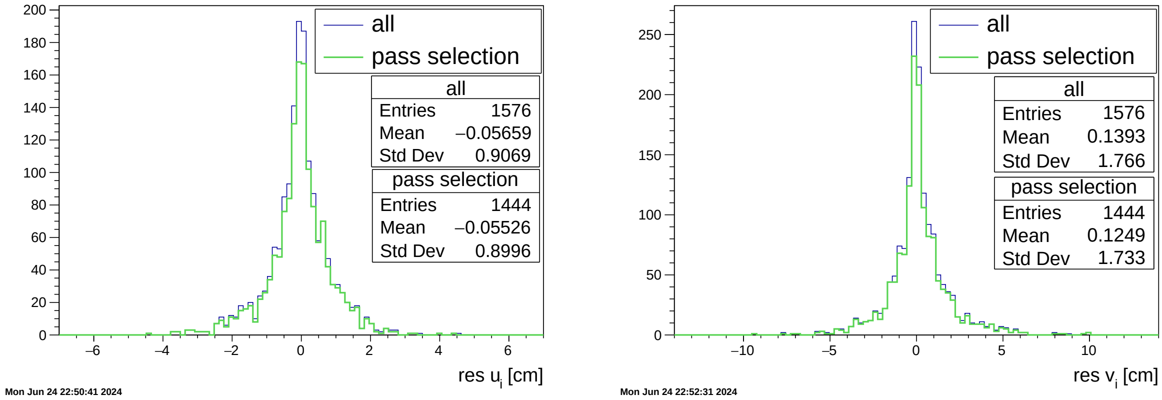

(a) *First intercept*

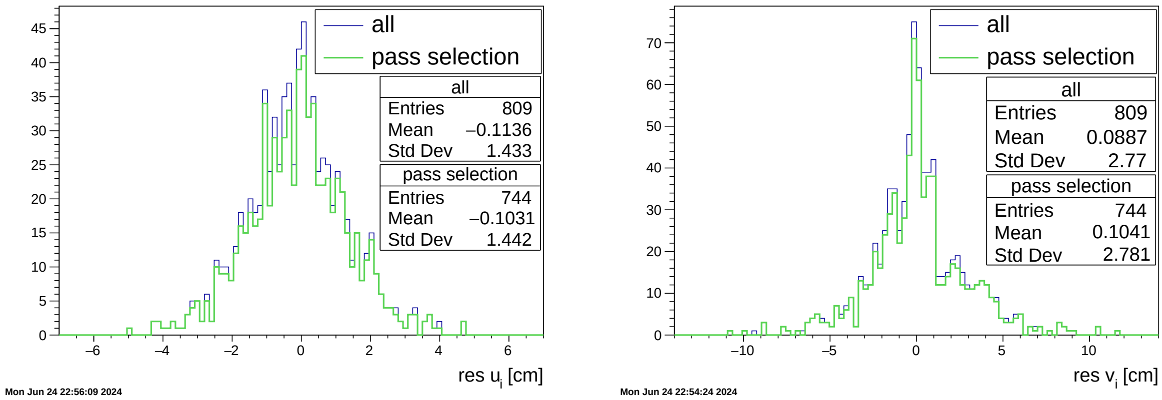

(b) *Second intercept*

Figure 4.20: Residuals of the local u and v coordinates of the first and the second intercepts for the second solution in the particle gun data sample with background. In green the intercepts that pass the selections, in blue all of them (if there is a true SVD cluster on the same sensor)

Table 4.4: Relative efficiencies calculated in the particle gun sample with beam background. The overall efficiency is the product of the efficiencies for at least one solution of that row and the rows above.

	solution 1	solution 2	at least one solution	overall efficiency
ϵ_{vtx}	-	-	$(68.6 \pm 0.8)\,\%$	$(68.6 \pm 0.8)\,\%$
$\epsilon_{p\pi}$	$(48.8 \pm 0.9)\,\%$	$(90.2 \pm 0.5)\,\%$	$(96.8 \pm 0.3)\,\%$	$(66.4 \pm 0.8)\,\%$
ϵ_{1i}	$(25.9 \pm 0.9)\,\%$	$(60.4 \pm 1.0)\,\%$	$(61.9 \pm 1.0)\,\%$	$(41.1 \pm 0.8)\,\%$
ϵ_{1h}	$(12.6 \pm 1.3)\,\%$	$(10.3 \pm 0.8)\,\%$	$(10.7 \pm 0.8)\,\%$	$(4.4 \pm 0.3)\,\%$
ϵ_{2i}	$(78 \pm 5)\,\%$	$(74 \pm 4)\,\%$	$(75 \pm 3)\,\%$	$(3.3 \pm 0.3)\,\%$
ϵ_{2h}	$(29 \pm 6)\,\%$	$(29 \pm 4)\,\%$	$(30 \pm 4)\,\%$	$(1.00 \pm 0.16)\,\%$

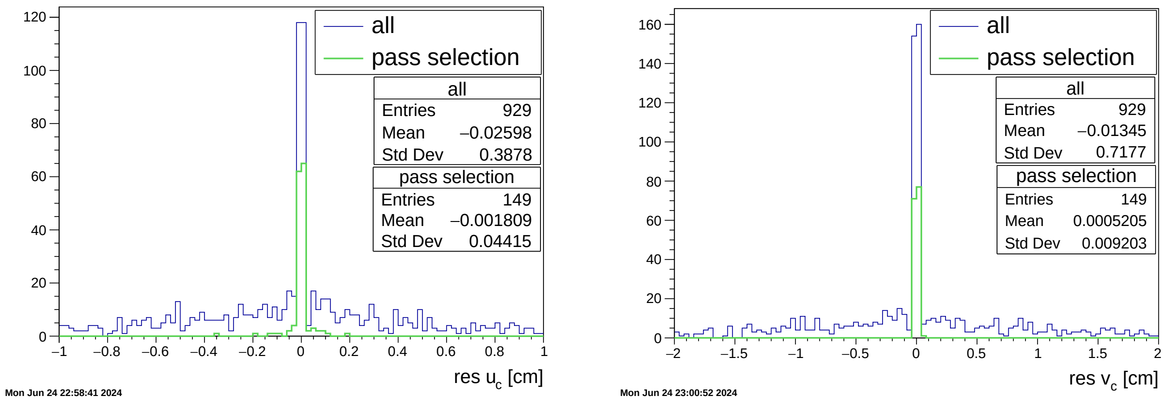

(a) *First cluster*

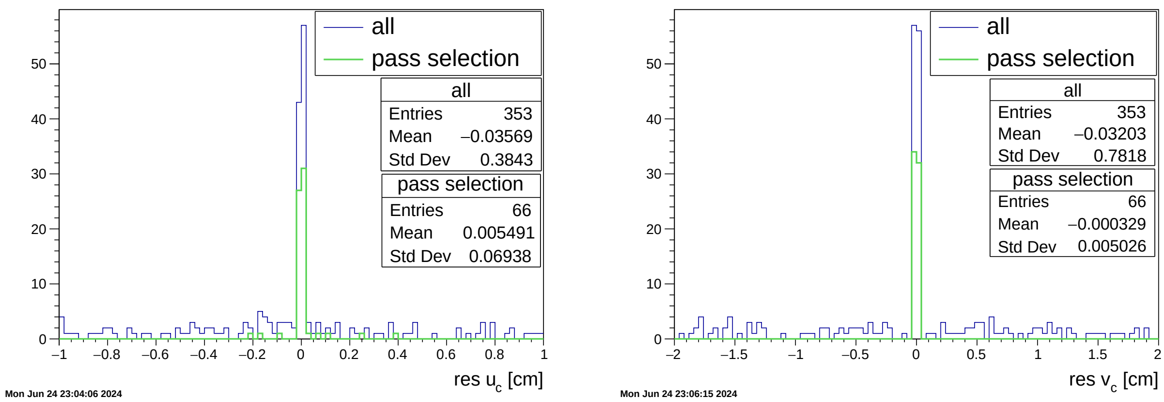

(b) *Second cluster*

Figure 4.21: Residuals of the local u and v coordinates of the closest clusters on the first and the second crossed layers for the second solution in the particle data sample with background. In green the clusters that pass the selections, in blue all of them (if there is a true SVD cluster on the same sensor).

Chapter 5

Physics application and outlook

The algorithm explained in the last chapter (Chapter 4) is applied to a dataset of $B\overline{B}$ events with beam background. The results in the efficiency are presented and compared to those obtain in the particle gun samples in the previous chapter. At the end of the chapter the outlook are discussed: possible improvement of the algorithm are presented, as well as other application of it and the impact of the application of this algorithm on CPV direct measurements.

5.1 Application on $B\overline{B}$ events

To better understand the actual impact on physics measurements, I apply the algorithm to a sample of 10 k $B\overline{B}$ events with the same beam background used in the particle gun sample in section 4.4. This $B\overline{B}$ sample is equivalent to the one used to study the K_S efficiency and inefficiency in the section 3.7.1. In that case I used official simulated samples (provided at analysis level), however, to apply the algorithm, these do not suffice since more information, like material information for the extrapolation, is needed, thus I generated the sample myself.

The main difference of this sample compared to the particle gun ones is the distribution of the K_S decay vertex inside the detector volume, shown in Fig. 5.1, and the distribution and the K_S momentum. This reflects that the K_S has a finite lifetime and a non-uniform momentum and angle distribution.

In this sample the baseline events (K_S decaying inside the fifth SVD layer with only one reconstructed daughter) are the $(10.8 \pm 0.3)\,\%$ of the total generated events, meaning a total of 1075 events.

In Fig. 5.2 the distributions of the true momentum of the two K_S daughters are reported: the maximum momentum is lower compared to the particle gun data sample (Fig. 4.6), for the rest the two distribution have a similar shapes.

Vertex selection The decay vertex is estimated as usual and the selection is applied. The $(82.1 \pm 1.2)\,\%$ of the events have the true vertex inside the range delimited by the *first hit* and the *previous intercept*. This is slightly more than in the particle gun sample with background (PGbkg) as expected: the distribution of the decay vertex is more dense near the IP, therefore the POCA is often taken as the *previous intercept*. Thus the range to delimit the z vertex position is often larger than necessary, since PXD layers are not considered. Its inefficiency is divided into:

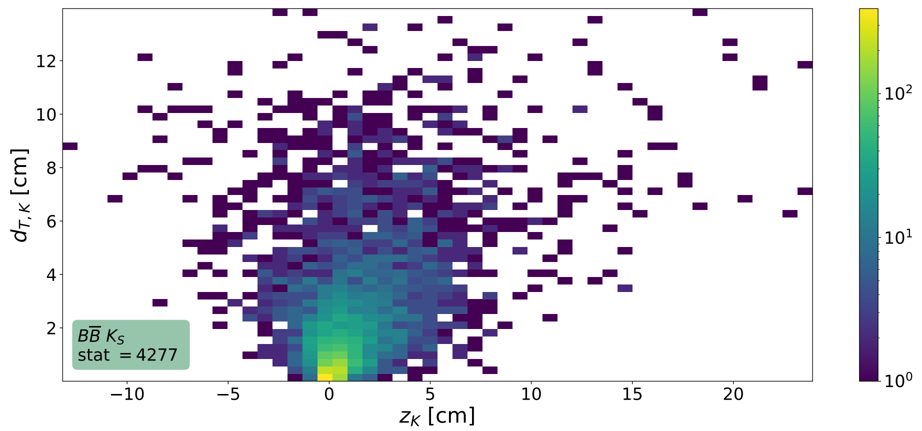

Figure 5.1: Decay vertex distribution of the K_S in $B\overline{B}$ events.

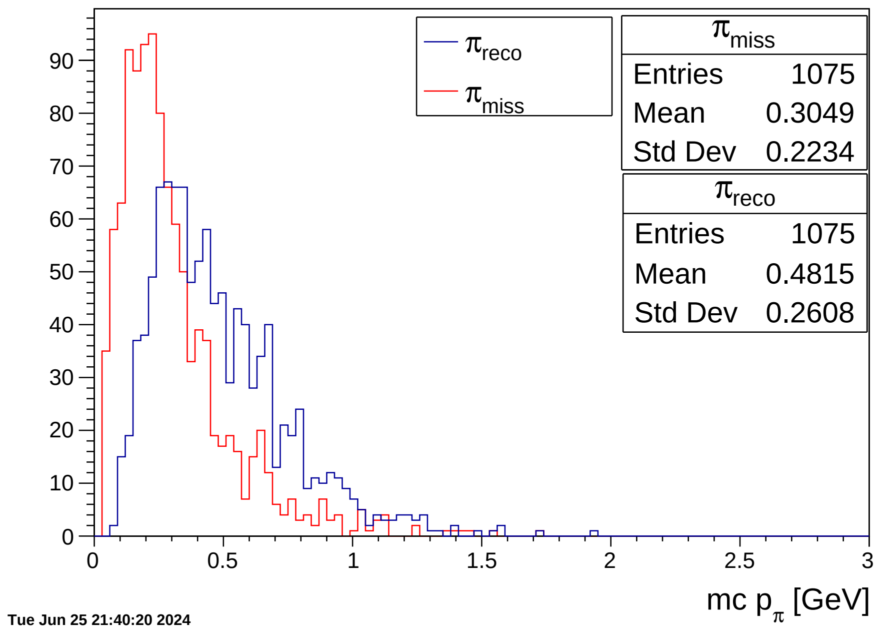

Figure 5.2: The distributions of the true momenta of the π_{miss} (in red) and the π_{reco} (in blue).

- no SVD clusters attached to the π_{reco} track, $(19 \pm 3)\,\%$
- use of the POCA as *previous intercept*, $(33 \pm 3)\,\%$
- wrong *first hit*, $(48 \pm 3)\,\%$.

The residuals for the estimated vertex are reported in Fig. 5.3. Comparing them to those in the PGbkg sample in Fig.4.18, it is observed that the asymmetry on the d_T coordinate is amplified. This is expected given the order in which the hypotheses on the z position of the vertex are made. In physics events it is more probable to have the vertex near the *previous intercept* instead to be equally distributed between the *previous intercept* and the *first hit*. To improve the ϵ_{vtx} per $B\overline{B}$ I could simply change the order which the z vertex position are tested, starting from the one near the IP. The order of the vertex hypotheses, and the intervals between them as well, should be optimized for physics events such as $B\overline{B}$ in future studies.

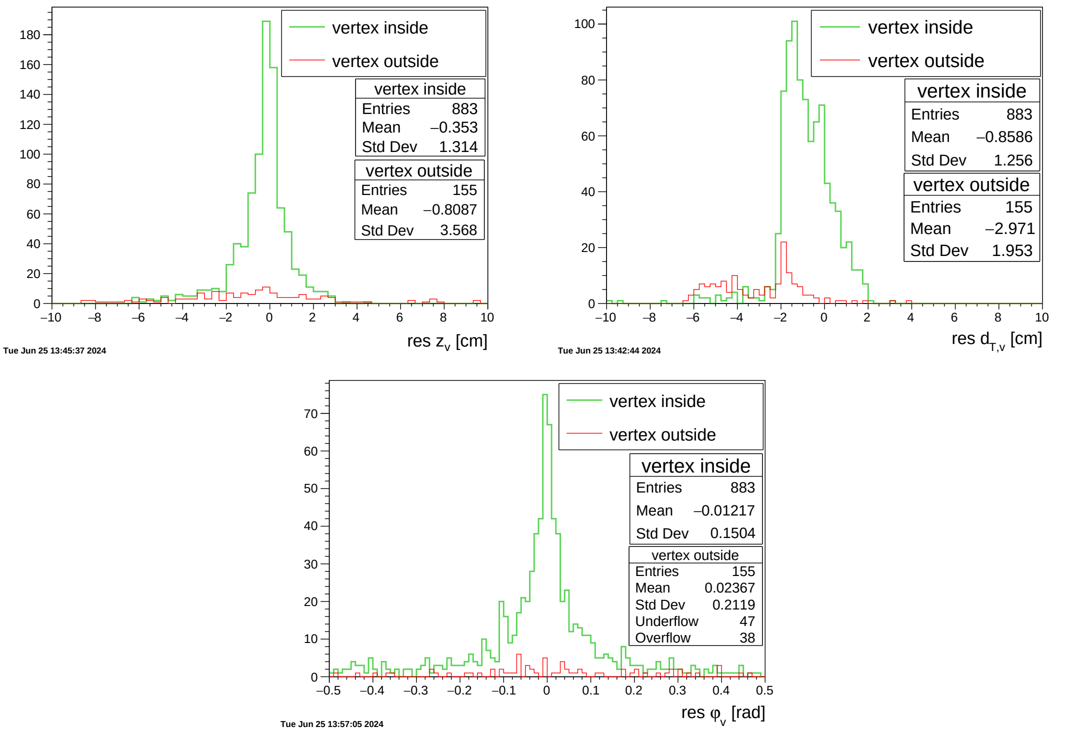

Figure 5.3: The residuals of the estimated vertex coordinates in the $B\overline{B}$ data sample. In red the distribution of the events that do not pass the selection and in green those which pass it.

Momenta calculation In Fig. 5.4 the residuals of the calculated π_{miss} momentum are reported for the two solutions. No main differences are observed with respect to the PG data sample, apart from the wider distribution for the second solution in the PGbkg sample.

Adding Clusters The probabilities ϵ_{1i}, ϵ_{1h}, ϵ_{2i}, ϵ_{2h} are defined and calculated as before, the results are reported in the summary table 5.1. Compared to those calculated in the PG sample only ϵ_{1i} is remarkably different, it is in fact almost the half of the one obtained

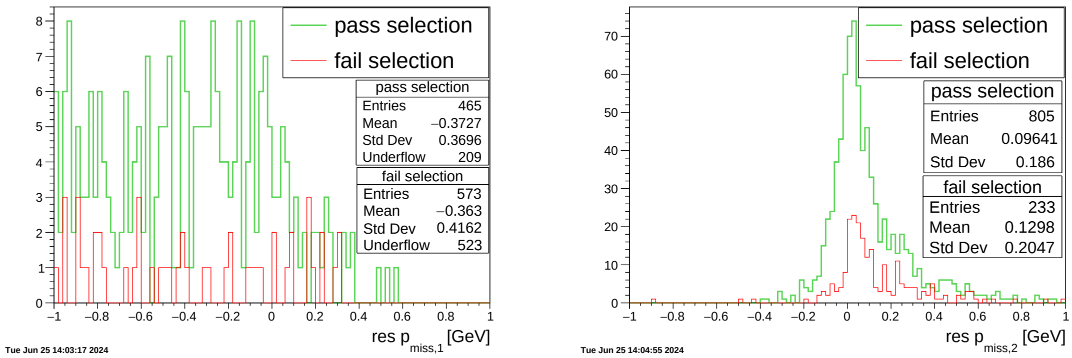

(a) *First solution* (b) *Second solution*

Figure 5.4: The residuals of the π_{miss} momentum for the two solutions. In red the distribution of the events that do not pass the selection and in green those who pass it.

in PG samples before. In particular it is significantly reduce for the second solution, that before it was the most substantial part of the efficiency of the two solutions combined. This is caused by the fact that the second solution works better for higher momenta of the π_{miss} but the momentum range in $B\overline{B}$ events is smaller than in PG events. In Fig. 5.5 and 5.6 the residuals of local coordinates of the first and second inside intercepts and the relative closer clusters are reported.

Table 5.1: Relative efficiencies calculated in the $B\overline{B}$ sample. The overall efficiency is the product of the efficiencies for at least one solution of that row and the rows above.

	solution 1	solution 2	at least one solution	overall efficiency
ϵ_{vtx}	-	-	$(82.1 \pm 1.2)\,\%$	$(82.1 \pm 1.2)\,\%$
$\epsilon_{p\pi}$	$(52.6 \pm 1.7)\,\%$	$(91.2 \pm 1.0)\,\%$	$(98.5 \pm 0.4)\,\%$	$(80.9 \pm 1.2)\,\%$
ϵ_{1i}	$(19.0 \pm 1.3)\,\%$	$(29.2 \pm 1.5)\,\%$	$(30.9 \pm 1.6)\,\%$	$(25.0 \pm 1.3)\,\%$
ϵ_{1h}	$(6.7 \pm 1.9)\,\%$	$(6.3 \pm 1.5)\,\%$	$(7.1 \pm 1.6)\,\%$	$(1.8 \pm 0.4)\,\%$
ϵ_{2i}	$(73 \pm 13)\,\%$	$(75 \pm 10)\,\%$	$(68 \pm 11)\,\%$	$(1.2 \pm 0.3)\,\%$
ϵ_{2h}	$(12 \pm 12)\,\%$	$(8 \pm 8)\,\%$	$(15 \pm 10)\,\%$	$(0.19 \pm 0.13)\,\%$

5.2 Results

All the relative efficiencies from Eq. 4.8 are reported in Tab. 5.2 for the three datasets: the particle gun sample without background (PG), the particle gun sample with background (PG Bkg) and the $B\overline{B}$ sample with background ($B\overline{B}$ Bkg).

The effect of the background can be observed in the differences between the results in the PG samples, with and without background. The efficiency on the selection of the vertex decreases with background because of the degradation of the performance of the current tracking algorithm that reconstructs the track of the pion used to select the vertex.

The differences of the physics sample with respect to the PG one with background are the distributions of the K_S decay vertex in the detector volume and of the K_S momentum. The effects of these differences on the efficiency are an higher efficiency in the selection

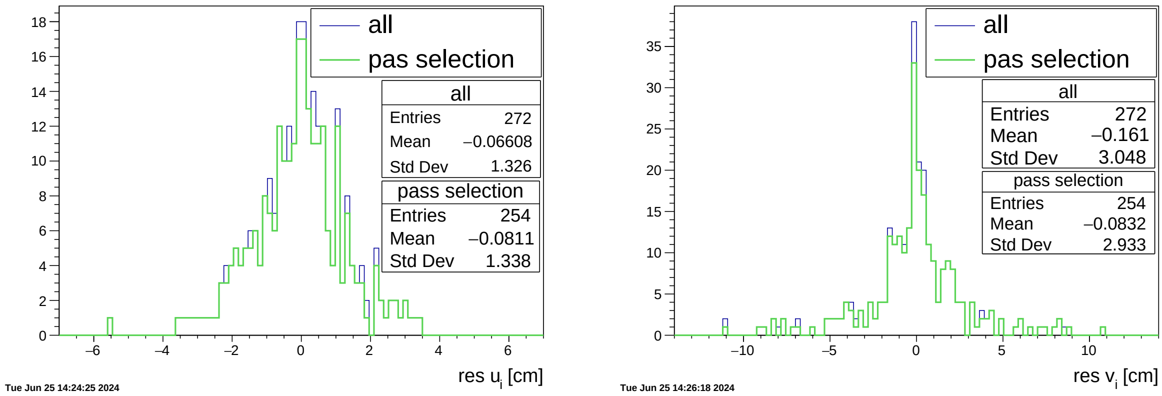

(a) *First intercept*

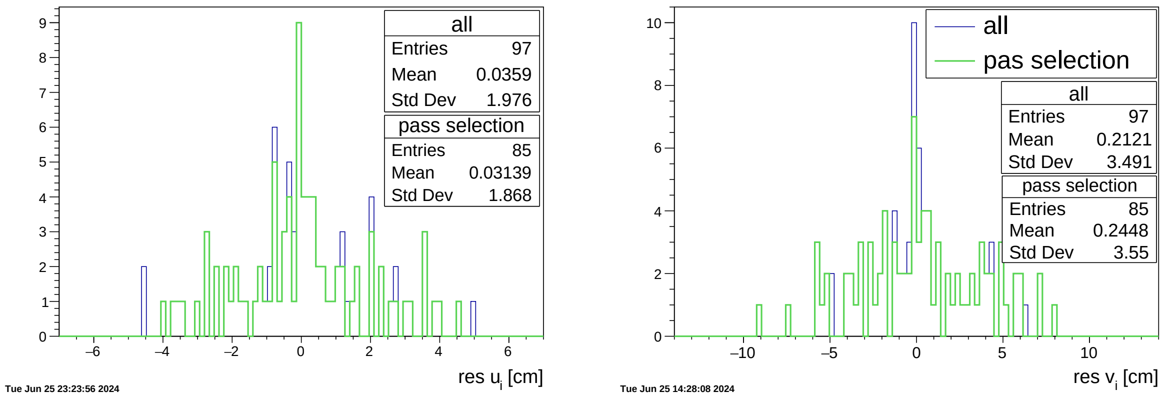

(b) *Second intercept*

Figure 5.5: Residuals of the local u and v coordinates of the first and the second intercepts for the second solution in the particle gun data sample with background. In green the intercepts that pass the selections, in blue all of them.

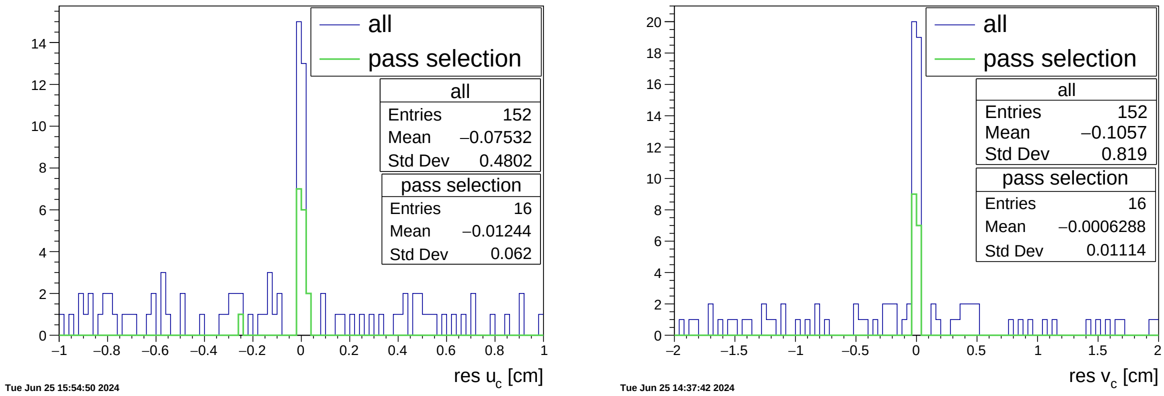

(a) *First cluster*

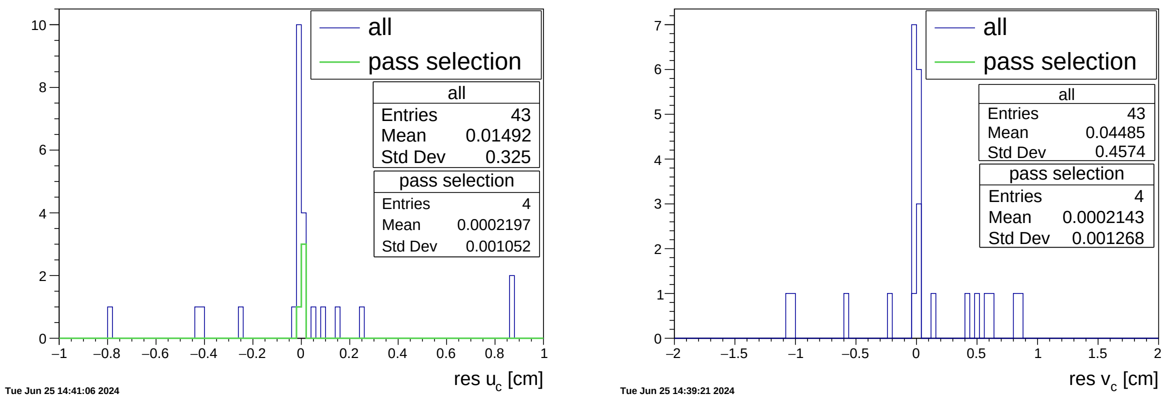

(b) *Second cluster*

Figure 5.6: Residuals of the local u and v coordinates of the first and the second clusters for the second solution in the $B\overline{B}$ data sample with background. In green the clusters that pass the selections, in blue all of them.

of the decay vertex as defined in section 4.3.1 and lower efficiency in finding the first intercept for the π_{miss} , in particular for the second solution.

	PG	PG Bkg	$B\overline{B}$ Bkg
ϵ_{vtx}	$(88.6 \pm 0.6)\,\%$	$(68.6 \pm 0.7)\,\%$	$(82.1 \pm 1.2)\,\%$
$\epsilon_{p\pi}$	$(97.8 \pm 0.3)\,\%$	$(96.8 \pm 0.3)\,\%$	$(98.5 \pm 0.4)\,\%$
ϵ_{1i}	$(58.4 \pm 1.1)\,\%$	$(61.9 \pm 1.0)\,\%$	$(30.9 \pm 1.6)\,\%$
ϵ_{1c}	$(11.6 \pm 0.9)\,\%$	$(10.7 \pm 0.8)\,\%$	$(7.1 \pm 1.6)\,\%$
ϵ_{2i}	$(61 \pm 4)\,\%$	$(75 \pm 3)\,\%$	$(68 \pm 11)\,\%$
ϵ_{2c}	$(26 \pm 5)\,\%$	$(30 \pm 4)\,\%$	$(15 \pm 10)\,\%$
ϵ_{tot}	$(0.91 \pm 0.19)\,\%$	$(1.00 \pm 0.16)\,\%$	$(0.19 \pm 0.13)\,\%$

Table 5.2: Results on particle gun dataset with (PGbkg) and without (PG) beam background, and on the $B\overline{B}$ events.

5.3 Possible future improvement

The overall efficiency, in all the three samples, is too low to insert the algorithm as it is inside the current reconstruction software. However there are many ideas how to improve this algorithm, some of them were anticipated in the previous chapters and are detailed here. They mainly translate in a better prediction of the K_S decay vertex and in a better selection of the hits of the missing track.

The ϵ_{vtx} efficiency could be improved by considering the dead regions of the detector in the search of the *previous intercept*. If no intercept is found on the previous layer with respect to the *first hit*, the POCA is taken instead, as explained in section 4.3.1. However, if there are more inner layers the search can continue on those, until an intercept is found, or there are no more inner layers, only at this point the POCA is taken. This should reduce the z range for these cases and thus improve the estimation on the position of the vertex as well. With the same goal, it should be considered to add the PXD layers in the search of the *previous intercept*, as already mentioned in section 4.2.4. Using the PXD, the prediction on the position of the vertex would improve for all those K_S that decay before the third SVD layer and after the PXD L1, for which the POCA was taken as *previous intercept*. These types of events are more common in physics events such as $B\overline{B}$ (see Fig. 3.13) because of the exponential decay time law that is not present in the particle gun data sample. By adding the information coming from the PXD the estimation on the K_S decay vertex is also improved for those K_S that decay inside the PXD since the *first cluster* can be found on its layer instead to go till the third layer.

In section 4.3.2, the Fig. 4.11 shows that the z range in which the vertex hypotheses are made can be quite large, resulting in a bad estimation of the K_S and π_{miss} momenta. In this work the efficiency of the selection of the vertex is probably overestimated, since I consider also reconstructed vertices far from the true one. A better prediction on the vertex would probably improve all the next steps till the search of the π_{miss} first intercept. In this work, the efficiency of the selection of the vertex is probably overestimated, since I consider also reconstructed vertices far from the true one.

It happens often that only one selected cluster (either u or v) is related to the MCParticle, while the one on the other side is wrong. Recovering all these cases would increase the efficiency by around a factor three. To improve the search of the clusters, a time selection removing off-time background clusters, like the one discussed in section 2.3.1, can be applied. For the extrapolation of the second intercept I could build a new helix at the position of the first hit with the momentum extrapolated at the first intercept, as shown in Fig. 5.7. Indeed the intercept position uncertainty is much larger than the cluster position resolution, starting the extrapolation from the hit should provide a better estimated second intercept and therefore a higher probability to find the second hit.

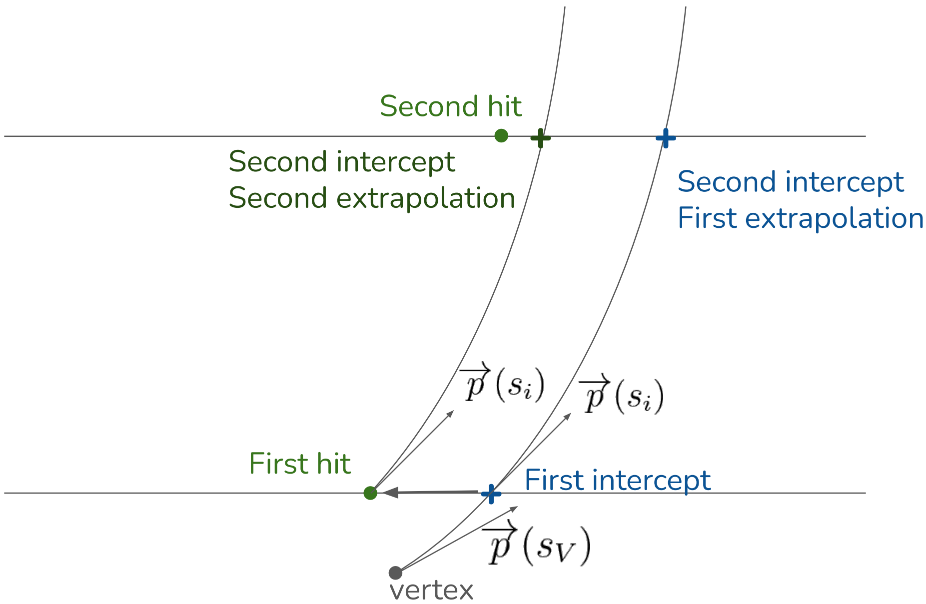

Figure 5.7: Sketch on how to improve the search of the second cluster when the first one is found. The crosses are the intercepts and the green dots are the hits on the SVD layers.

In section 4.2.4 the idea to include the information coming from the CDC was anticipated as well. The multiple hits of the chamber would improve the reconstruction of the missing pion, with a reduction of the possible fake rate generated by the algorithm.

5.4 Impact on CPV measurements in meson decay

I estimate what would be the impact on a CP asymmetry (Eq. 1.22) measurement with a single K_S in the final state when the tracking efficiency of the K_S increases from ϵ_{K_S} to $\epsilon_{K_S} + \Delta\epsilon_{K_S}$. With a simple error propagation of the statistical uncertainty σ_{CP} of CP asymmetry, an improved σ'_{CP} is obtained:

$$\sigma'_{CP} = \frac{\sigma_{CP}}{\sqrt{1 + \Delta\epsilon_{K_S}/\epsilon_{K_S}}}. \tag{5.1}$$

The current gain in efficiency of this algorithm is not enough to have a relevant impact. Estimating the effect of the improvements described before is not straight forward. Let's assume that a total efficiency of $\sim 25\%$ could be achieved. Since the fraction of K_S , with only one reconstructed daughter, decaying inside the fifth layer is $\sim 13\%$, the efficiency gain would be $\Delta\epsilon_{K_S} \sim 3.3\%$, yielding a decrease of the statistical uncertainty by the $\sim 2\%$

(using $\epsilon_{K_S} \sim 81\%$). To change prospective I also estimate the equivalent increase of the luminosity with

$$L' = L(1 + \Delta\epsilon_{K_S}/\epsilon_{K_S}), \tag{5.2}$$

finding that is $\sim 4\%$.

This is especially useful in analyses where the statistical uncertainty is dominant. For example, in the analysis of $D^0 \to K_S K_S$ at Belle (described in section 1.3.3), assuming that the $\Delta\epsilon_K$ estimated for $B\overline{B}$ is the same for $c\overline{c}$ events, the statistical uncertainty of the CP asymmetry would improve from 1.53 to 1.47; indeed, in case of two K_S in the final state Eq. 5.1 and 5.2 become:

$$\sigma'_{CP} = \frac{\sigma_{CP}}{\sqrt{1 + 2\Delta\epsilon_{K_S}/\epsilon_{K_S} + (\Delta\epsilon_{K_S}/\epsilon_{K_S})^2}} \tag{5.3}$$

$$L' = L(1 + \Delta\epsilon_{K_S}/\epsilon_{K_S} + (\Delta\epsilon_{K_S}/\epsilon_{K_S})^2). \tag{5.4}$$

5.5 Other applications

The algorithm was designed to recover K_S with one correctly reconstructed daughter and the other missed by the current tracking algorithm. However it could be applied also to the other $V0$ particles, such as the Λ, simply by changing the mass hypothesis in the quadri-momentum conservation, after checking that a relevant fraction of inefficiency is due to a missing daughter, as it was done for the K_S in section 3.7.1.

It could also be interesting to implement the algorithm to recovered the case E2W1, where both of the daughters of the $V0$ particle are reconstructed but one has been assigned the wrong charge. Ideally the algorithm, applied to the correctly reconstructed daughter track, will find the SVD clusters of the daughter that was reconstructed with the wrong charge. When the algorithm finds that the clusters are already assigned to another track with an incompatible charge, it can try to flip and refit the track to make a V0 particle. If by changing the charge the fit converges and is compatible with a $V0$ daughter, the charge is corrected and the second daughter is correctly found.

Conclusion

The aim of this project was the development of an algorithm to improve the K_S tracking efficiency at the Belle II experiment. The K_S is a particle often present in decay channels of interest for modern particle physics, for instance for CPV measurements in the B and D meson decays. Its displaced vertex is the cause of a lower reconstruction efficiency with respect to other primary particles; in fact the tracking algorithms implemented at Belle II are optimized for charged particles coming from the interaction point.

The main inefficiency, in the reconstruction of the K_S in two charged pions, is caused by the failure of the reconstruction of one of the two charged daughters. The algorithm that I have developed focuses on the recovery of this kind of K_S, exploiting only information coming from the SVD: using the trajectory of the reconstructed daughter, it is possible to search for SVD clusters of the missing one in selected regions of the detector. The information of the reconstructed daughter provides a region where to look for the K_S decay vertex. An estimate of the vertex, together with the assumption of the K_S coming from the interaction point, allows to write a second-degree equation from the quadri-momentum conservation and to compute two estimates for the K_S momentum and the corresponding two of the missing pion momentum. Each estimate is used as seed, together with the estimated vertex position, to built a temporary helix of π_{miss}, used to search for SVD clusters in the vicinity of its intercepts with the SVD layers, in order to fit the track.

The algorithm was applied to three different data samples, two of them generated with a particle gun, with and without beam background, while the last one using a $B\overline{B}$ event generator with beam background; the algorithm efficiencies are computed and compared. The overall efficiency is low, around 1% in the particle gun data sets, this mainly comes from the poor efficiency in the search of the π_{miss} SVD clusters from the found intercept. An optimization of the search of the clusters is suggested for further studies, to improve the efficiency of this step. The efficiency results of the particle gun sample with and without background are quite similar. The main difference is on the estimation of the K_S decay vertex that appears worse with background because of the degradation of the π_{reco} reconstruction by the current tracking algorithm at Belle II. Not many improvements are discussed for this step, however this inefficiency is small with respect to the main one. A similar comparison on $B\overline{B}$ samples (with and without background) should be done to see if there are other background effects more relevant in physics events. In the $B\overline{B}$ dataset the decay vertex and momentum distribution of the K_S are quite different than in the particle gun samples, these differences translate in a decrease of the probability to find the π_{miss} intercepts on the correct sensor. This is probably caused by the lower momentum of the π_{miss} , that is more affected by multiple scattering. Even if the first results obtained are not optimal, there are many ideas how to improve the algorithm.

Bibliography

[1] M. Thomson. *Modern particle physics*. New York: Cambridge University Press, 2013. ISBN: 978-1-107-03426-6. DOI: 10.1017/CBO9781139525367.

[2] D. H. Perkins. *Introduction to high energy physics*. 1982. ISBN: 978-0-521-62196-0.

[3] Serguei Chatrchyan et al. "Observation of a New Boson at a Mass of 125 GeV with the CMS Experiment at the LHC". In: *Phys. Lett. B* 716 (2012), pp. 30–61. DOI: 10.1016/j.physletb.2012.08.021. arXiv: 1207.7235 [hep-ex].

[4] Georges Aad et al. "Observation of a new particle in the search for the Standard Model Higgs boson with the ATLAS detector at the LHC". In: *Phys. Lett. B* 716 (2012), pp. 1–29. DOI: 10.1016/j.physletb.2012.08.020. arXiv: 1207.7214 [hep-ex].

[5] Kou et al. "The Belle II Physics Book". In: *Progress of Theoretical and Experimental Physics* 2019.12 (Dec. 2019). ISSN: 2050-3911. DOI: 10.1093/ptep/ptz106. URL: http://dx.doi.org/10.1093/ptep/ptz106.

[6] Particle Data Group and R L et al. Workman. "Review of Particle Physics". In: *Progress of Theoretical and Experimental Physics* 2022.8 (Aug. 2022), p. 083C01. ISSN: 2050-3911. DOI: 10.1093/ptep/ptac097. eprint: https://academic.oup.com/ptep/article-pdf/2022/8/083C01/49175539/ptac097.pdf. URL: https://doi.org/10.1093/ptep/ptac097.

[7] J. Charles et al. URL: http://ckmfitter.in2p3.fr (visited on 06/20/2024).

[8] J. H. Christenson et al. "Evidence for the 2π Decay of the K_2^0 Meson". In: *Phys. Rev. Lett.* 13 (1964), pp. 138–140. DOI: 10.1103/PhysRevLett.13.138.

[9] M. Sozzi. *Discrete symmetries and CP violation: From experiment to theory*. 2008.

[10] Aaij R. et al. "Measurement of the Time-Integrated CP Asymmetry in $D^0 \to K^-K^+$ Decays". In: *Phys. Rev. Lett.* 131 (9 Aug. 2023), p. 091802. DOI: 10.1103/PhysRevLett.131.091802. URL: https://link.aps.org/doi/10.1103/PhysRevLett.131.091802.

[11] Aaij R. et al. "Observation of CP Violation in Charm Decays". In: *Physical Review Letters* 122.21 (May 2019). ISSN: 1079-7114. DOI: 10.1103/physrevlett.122.211803. URL: http://dx.doi.org/10.1103/PhysRevLett.122.211803.

[12] Marco Gersabeck. "Introduction to Charm Physics". In: *PoS* FWNP (2015), p. 001. DOI: 10.22323/1.220.0001. arXiv: 1503.00032 [hep-ex].

[13] The Heavy Flavor Averaging Group. *HFlav results*. URL: https://hflav.web.cern.ch/results (visited on 06/14/2024).

[14] Giulia Casarosa. “Measurement of Mixing and CP Violation in the Two-Body D0 decays to K+K−, π+ π− and K± π∓ with the BABAR Experiment”. PhD thesis. Pisa U., 2012. DOI: 10.2172/1060207.

[15] Belle II Collaboration and I. Adachi et al. *A new graph-neural-network flavor tagger for Belle II and measurement of* $\sin 2\phi_1$ *in* $B^0 \to J/\psi K^0_S$ *decays*. 2024. arXiv: 2402.17260 [hep-ex].

[16] Adachi I. et al. “Measurement of CP asymmetries in $B^0 \to \phi K^0_s$ decays with Belle II”. In: *Phys. Rev. D* 108 (7 Oct. 2023), p. 072012. DOI: 10.1103/PhysRevD.108.072012. URL: https://link.aps.org/doi/10.1103/PhysRevD.108.072012.

[17] Adachi I. et al. “Measurement of CP Violation in $B^0 \to K^0_S\pi^0$ Decays at Belle II”. In: *Phys. Rev. Lett.* 131 (11 Sept. 2023), p. 111803. DOI: 10.1103/PhysRevLett.131.111803. URL: https://link.aps.org/doi/10.1103/PhysRevLett.131.111803.

[18] Abudinén et al. “Combined analysis of Belle and Belle II data to determine the CKM angle Φ_3 using $B^+ \to D(K^0_S h^+ h^-)h^+ decays$”. In: *Journal of High Energy Physics* (2022). DOI: 10.1007/JHEP02(2022)063. URL: https://doi.org/10.1007/JHEP02(2022)063.

[19] Roel Aaij et al. “Measurement of CP asymmetry in $D^0 \to K^0_S K^0_S$ decays”. In: *Phys. Rev. D* 104.3 (2021), p. L031102. DOI: 10.1103/PhysRevD.104.L031102. arXiv: 2105.01565 [hep-ex].

[20] *SuperKEKB Design Report*. URL: https://www-linac.kek.jp/linac-com/report/skb-tdr/ (visited on 04/30/2024).

[21] Kazunori Akai, Kazuro Furukawa, and Haruyo Koiso. “SuperKEKB Collider”. In: *Nucl. Instrum. Meth. A* 907 (2018), pp. 188–199. DOI: 10.1016/j.nima.2018.08.017. arXiv: 1809.01958 [physics.acc-ph].

[22] *SuperKEKB web page*. URL: https://www-superkekb.kek.jp (visited on 04/27/2024).

[23] Yukiyoshi Ohnishi et al. “Accelerator design at SuperKEKB”. In: *PTEP* 2013 (2013), 03A011. DOI: 10.1093/ptep/pts083.

[24] A. Natochii et al. “Measured and projected beam backgrounds in the Belle II experiment at the SuperKEKB collider”. In: *Nucl. Instrum. Meth. A* 1055 (2023), p. 168550. DOI: 10.1016/j.nima.2023.168550. arXiv: 2302.01566 [hep-ex].

[25] Mika Masuzawa. “SuperKEKB Status”. In: *PoS* EPS-HEP2023 (2024), p. 610. DOI: 10.22323/1.449.0610.

[26] Belle II collaboration. *Belle II Luminosity*. URL: https://www.belle2.org/research/luminosity/ (visited on 05/21/2024).

[27] H. Tanigawa et al. “Beam background study for the Belle II Silicon Vertex Detector”. In: *Nucl. Instrum. Meth. A* 982 (2020), p. 164580. DOI: 10.1016/j.nima.2020.164580.

[28] T. Abe et al. “Belle II Technical Design Report”. In: (Nov. 2010). arXiv: 1011.0352 [physics.ins-det].

[29] Georgios Giakoustidis et al. “Status of the BELLE II Pixel Detector”. In: *PoS* Pixel2022 (2023), p. 005. DOI: 10.22323/1.420.0005.

[30] Hua Ye. “Commissioning of the Belle II Pixel Vertex Detector”. In: *PoS* EPS-HEP2019 (2020), p. 122. DOI: 10.22323/1.364.0122.

[31] K. Adamczyk et al. “The design, construction, operation and performance of the Belle II silicon vertex detector”. In: *Journal of Instrumentation* 17.11 (Nov. 2022), P11042. DOI: 10.1088/1748-0221/17/11/P11042. URL: https://dx.doi.org/10.1088/1748-0221/17/11/P11042.

[32] M. Friedl et al. “The Belle II Silicon Vertex Detector”. In: *Nuclear Instruments and Methods in Physics Research Section A: Accelerators, Spectrometers, Detectors and Associated Equipment* 732 (2013). Vienna Conference on Instrumentation 2013, pp. 83–86. ISSN: 0168-9002. DOI: https://doi.org/10.1016/j.nima.2013.05.171. URL: https://www.sciencedirect.com/science/article/pii/S0168900213007936.

[33] M.J. French et al. “Design and results from the APV25, a deep sub-micron CMOS front-end chip for the CMS tracker”. In: *Nuclear Instruments and Methods in Physics Research Section A: Accelerators, Spectrometers, Detectors and Associated Equipment* 466.2 (2001). 4th Int. Symp. on Development and Application of Semiconductor Tracking Detectors, pp. 359–365. ISSN: 0168-9002. DOI: https://doi.org/10.1016/S0168-9002(01)00589-7. URL: https://www.sciencedirect.com/science/article/pii/S0168900201005897.

[34] C. Irmler et al. “A Low Mass On-Chip Readout Scheme for Double-Sided Silicon Strip Detectors”. In: *Nuclear Instruments and Methods in Physics Research Section A: Accelerators, Spectrometers, Detectors and Associated Equipment* 732 (2013). Vienna Conference on Instrumentation 2013, pp. 109–112. ISSN: 0168-9002. DOI: https://doi.org/10.1016/j.nima.2013.05.169. URL: https://www.sciencedirect.com/science/article/pii/S0168900213007912.

[35] S. Mondal et al. “Silicon vertex detector of the Belle II experiment”. In: *JINST* 19.02 (2024), p. C02038. DOI: 10.1088/1748-0221/19/02/C02038. arXiv: 2312.06501 [hep-ex].

[36] Kazuki Kojima. “The operation and performance of the TOP detector at the Belle II experiment”. In: *PoS* EPS-HEP2021 (2022), p. 803. DOI: 10.22323/1.398.0803.

[37] I. Adachi et al. “Detectors for extreme luminosity: Belle II”. In: *Nucl. Instrum. Meth. A* 907 (2018), pp. 46–59. DOI: 10.1016/j.nima.2018.03.068.

[38] Belle II collaboration. *Belle II analysis software framework documentation.* URL: https://software.belle2.org/development/sphinx/index.html (visited on 06/27/2024).

[39] T. Kuhr et al. “The Belle II Core Software”. In: *Computing and Software for Big Science* 3.1 (2018), p. 1. DOI: 10.1007/s41781-018-0017-9. URL: https://doi.org/10.1007/s41781-018-0017-9.

[40] Valerio Bertacchi et al. “Track finding at Belle II”. In: *Computer Physics Communications* 259 (2021), p. 107610. ISSN: 0010-4655. DOI: https://doi.org/10.1016/j.cpc.2020.107610. URL: https://www.sciencedirect.com/science/article/pii/S0010465520302861.

[41] Tadeas Bilka et al. “Implementation of GENFIT2 as an experiment independent track-fitting framework”. In: (Feb. 2019). arXiv: 1902.04405 [physics.data-an].

[42] Moritz Nadler and Rudolf Frühwirth. “Robust track fitting in the Belle II inner tracking detector”. In: *Journal of Physics: Conference Series* 396.2 (Dec. 2012), p. 022037. DOI: 10.1088/1742-6596/396/2/022037. URL: https://dx.doi.org/10.1088/1742-6596/396/2/022037.

[43] Belle II collaboration. *Belle II Event Display.* URL: https://display.belle2.org (visited on 06/27/2024).

[44] T. Alexopoulos et al. “Implementation of the Legendre Transform for track segment reconstruction in drift tube chambers”. In: *Nuclear Instruments and Methods in Physics Research Section A: Accelerators, Spectrometers, Detectors and Associated Equipment* 592.3 (2008), pp. 456–462. ISSN: 0168-9002. DOI: https://doi.org/10.1016/j.nima.2008.04.038. URL: https://www.sciencedirect.com/science/article/pii/S0168900208005780.

[45] A. Glazov et al. “Filtering tracks in discrete detectors using a cellular automaton”. In: *Nuclear Instruments and Methods in Physics Research Section A: Accelerators, Spectrometers, Detectors and Associated Equipment* 329.1 (1993), pp. 262–268. ISSN: 0168-9002. DOI: https://doi.org/10.1016/0168-9002(93)90945-E. URL: https://www.sciencedirect.com/science/article/pii/016890029390945E.